Development of High Temperature Electrodeposited LIGA MEMS Materials

M. Haj-Taieb, J. Aktaa, K. Bade
Institut für Materialforschung
Institut für Mikrostrukturtechnik

Development of high temperature electrodeposited LIGA MEMS materials

Manel Haj-Taieb*, Jarir Aktaa, Klaus Bade

Institut für Materialforschung

Institut für Mikrostrukturtechnik

Development of high temperature electrodeposited LIGA MEMS materials

Zur Erlangung des akademischen Grads eines

Doktors der Ingenieurwissenschaften

an der Fakultät für Maschinenbau der
Universität Karlsruhe (TH)
eingereichte

Dissertation

von
Dipl.-Ing. Manel Haj-Taieb
aus Sfax, Tunesien

Tag der mündlichen Prüfung: 10.06.2009

Hauptreferent:	Prof. Dr. Oliver Kraft
Korreferent:	Prof. Dr. Volker Saile
Korreferent:	Prof. Dr. Kevin Hemker

Abstract

In the current work, new electrodeposited materials including Ni-W alloys, Ni-Al$_2$O$_3$ nanocomposites and Ni based superalloys were developed for use in high temperature MEMS applications. Ni-W alloys with different compositions (Ni 5 at% W and Ni 15 at% W) were electrodeposited from an alkaline ammonia citrate electrolyte in the form of compact thick (≥ 100 μm) layers and LIGA microspecimens. The mechanical investigations demonstrated in the as-deposited state higher strength and a brittle behaviour compared to pure nickel; while in the annealed state (300 - 700 ^{o}C), the strength remained high and additional plasticity was noticed. Higher W content resulted in higher strength up to a 700 ^{o}C annealing temperature, whereas lower W content led to more softening after annealing. These properties were confirmed by the nanocrystalline microstructure showing grains smaller than 100 nm in the as-deposited state that slightly increased in size after annealing but still remaining in the submicron range. This microstructural stability can be explained by the effect of W atoms impeding the boundaries' movements. In order to incorporate Al$_2$O$_3$ into compact and thick layers and microspecimens, an electrolyte was developed and optimized based on an alkaline ammonia citrate sulfate solution containing hydrophilic nanoparticles electrostatically dispersed. The incorporation of the particles was evidenced by the detected nanosized agglomerates presenting an Al$_2$O$_3$ content of about 3 wt% and 1.3 wt% for the layers and the microspecimens, respectively, and the increase in strength and brittleness in the as-deposited state compared to pure nickel. After annealing, Ni-Al$_2$O$_3$ remained strong, which was in agreement with the slight increase in grain size showing microstructural stability till an annealing temperature of 600 ^{o}C. This may be due to the pinning effect of the particles on the grain boundaries. For use in the formation of superalloys, Ni-Al composites were electrodeposited from a similar solution as Ni-Al$_2$O$_3$ at a neutral pH and containing metallic aluminum particles. It has been shown that the size of the particles affects the structure of the electrodeposited layer that was non-compact when incorporating microparticles, in contrast to nanoparticles resulting in defect free material. Moreover, the electrolyte was unstable even after a short aging time (24h). A first model, based on the determination of the diffusion distance of aluminum in nickel, was presented predicting the annealing parameters necessary for the formation of the high temperature resistant γ' phase.

Kurzfassung

Im Rahmen dieser Arbeit, wurden drei abgeschiedene neue Materialien Ni-W Legierungen, Ni-Al$_2$O$_3$ Nanokomposite und Ni-Basis Superlegierungen für Hochtemperaturanwendungen von MEMS Mikroteilen entwickelt. Zwei Ni-W Legierungen mit den Zusammensetzungen Ni 15 At% W und Ni 5 At% W wurden aus einem Ammonia-Citrat Elektrolyten in Form von kompakten Schichten und Mikroprüfkörper mit einer Dicke ≥ 100 μm elektrochemisch abgeschieden. Die mechanischen Untersuchungen zeigten, im Vergleich zu reinem Nickel, eine höhere Festigkeit und ein sprödes Verhalten im abgeschiedenen Zustand, während das Glühen bei hohen Temperaturen (300 - 700 ^{o}C) ergab ebenfalls hohe Festigkeit aber zusätzliche Plastizität. Hoher W Gehalt ergab hohe Festigkeit bis zu einer Glühtemperatur von 700 ^{o}C, während niedriger W Gehalt fuhr zu mehr Plastizität bei hohen Glühtemperatur. Diese Eigenschaften wurden von der nanokrystallinen Gefügestruktur bestätigt, wo die Körner im abgeschiedenen Zustand eine Gröβe kleiner als 100 nm aufwiesen, während im geglühten Zustand eine Zunahme der Korngröβe, bleibend im submikrometer Bereich, war zu sehen. Diese mikrostrukturelle Stabilität kann auf dem hemmenden Effekt der W Atome auf die Korngrenzenbewegung zurückgeführt werden. Die Abscheidung von kompaktem und dickem Ni-Al$_2$O$_3$ war aus einer optimierten Dispersion gelungen, die aus einer alkalischen Ammonia-Citrat Sulfat Lösung und elektrostatisch stabilisierten hydrophilen Al$_2$O$_3$ Nanopartikeln besteht. Das Einbauen von Nanopartikeln wurde mit einem gemessenen Partikelgehalt von 3 Gew% und 1,3 Gew% Al$_2$O$_3$ in Schichten, beziehungsweise in Mikroprüfkörper und einer Steigerung der Festigkeit und Sprödigkeit im abgeschiedenen Zustand im Vergleich zu rein Nickel, bestätigt. Im geglühten Zustand, Ni-Al$_2$O$_3$ blieb fest, was mit der geringen Steigerung der Korngröβe übereinstimmt. Dies entsprach der mikrostrukturellen Stabilität bis zu einer Glühtemperatur von 600 ^{o}C, verursacht durch das Korngrenzen Pinning Effekt der Partikel. Zwecks der Herstellung von Superlegierungen, wurden Ni-Al Komposite aus einer neutralen Ammonia - Citrat Nickel Sulfat Lösung mit dispergierten metallischen Aluminium Partikel abgeschieden. Es wurde gezeigt dass die Partikelgröβe die Struktur der abgeschiedenen Material beeinflusst, wobei der Einbau von Mikropartikeln, im Gegensatz zu Nanopartikeln, ein nicht kompaktes Material liefert. Das Elektrolyte zeigte sich instabil schon nach kurzem Altern. Basierend auf der Bestimmung der Diffusionslänge von Aluminium in Nickel, wurde ein erstes Modell gedacht um über die Glühparameter, notwendig für die Bildung der Hochtemperatur feste γ' Phase, vorauszusagen.

Danksagung

Contents

Contents

1 Introduction

The field of micro-electro-mechanical systems, known as MEMS, has exploded in the past two decades with prospects for a multi-billion dollar industry. To date, the vast majority of commercial MEMS devices have involved thin films sensors (e.g. polysilicon accelerometers and silicon nitride pressure sensors) that are manufactured using chemical and physical vapour deposition processes. Next generation MEMS applications will not be restricted to two-dimensional sensors, and material with well-developed processing routes, greater dimensional freedom and enhanced physical and mechanical properties are needed to fuel the MEMS explosion. Classes of MEMS devices that are currently being developed include miniature: mechanical and physical sensors, gyroscopes for guidance systems, chemical and biological sensors, RF filters for telecommunication devices, biomedical probes and instruments, fusing/safeing and arming devices, heat exchangers and power generation systems. These applications require a much wider range of material functionality than is offered by traditional thin film materials. Examples of materials that are being considered for use in MEMS devices include but are not limited to: polysilicon, single crystal silicon, silicon carbide, silicon nitride, silicon beryllium, amorphous diamond, LIGA nickel, copper and permalloy, as well as SU8 and other polymeric compounds. Since metals offer high electrical and thermal conductivity, relatively high stiffness and strength and very high fracture toughness, this work is focused on the development of metallic materials realized by LIGA, an acronym derived from the German words for lithography, electroplating, and molding.

Electrodeposited LIGA nickel is one of the most used structural metallic materials for MEMS as it presents a classic material that has been studied for longer time and can be electrodeposited in form of thicker layers. For instance, a variety of micro sensors and actuators and for molding tools for polymeric and ceramic micro parts ([1], [2], [3]) have been developed. Current LIGA processing generally results in electrodeposited nickel structures with high aspect ratios and an attractive balance of room temperature properties. Unfortunately thermal exposure of LIGA nickel has been shown to result in microstructural

1

instabilities and significant property degradation, which limits the use of LIGA structures in elevated temperature MEMS applications such as power generation devices, thermal actuators etc. It is known that by adding alloying elements, particles or new phases it is possible to enhance the thermal stability of these LIGA structures and their mechanical properties at high temperature. The reliability of such new materials is difficult to predict in the same length scale as microparts will be produced and used. This is due to the lack of properties characterizing the mechanical behaviour and the thermal stability at high temperature in the concerned length scale.

In this research work resulting from a collaboration between Forschungzentrum Karlsruhe (FZK) and the Johns Hopkins University (JHU), Ni-W alloy, Ni-Al_2O_3 nanocomposite and Ni-base superalloy are electrodeposited and investigated. For Ni-W, the micropattern fabrication process is studied where relevant features are demonstrated and interpreted. The electrodeposition of Ni-Al_2O_3 is developed in terms of understanding the influence of electrolyte chemistry and electrodeposition parameters on the resulting layers and microspecimens' structure. The mechanical and microstructural properties in the as-deposited and annealed state of both Ni-W and Ni-Al_2O_3 are presented and discussed in comparison to pure nickel. First attempts for Ni-Al composite electrodeposition were carried out in order to prove the concept of forming layers with the intermetallic γ' - phase (Ni_3Al). Some open issues related to the formation of this phase, which is characteristic of the Ni-base superalloy, are discussed in order to predict the necessary annealing parameters.

2 State of the art

2.1 LIGA process for the use in MEMS applications

The leading technology for manufacturing MEMS devices is Si-micromachining. However these technologies are not able to solve the existing problems posed by the great variety of functions, the specificity of the operation surroundings and the optimum cost/performance ratio of the MEMS parts. The invention of the LIGA technique by researchers at the Forschungszentrum Karlsruhe (FZK) in the 1980s opened a door for MEMS devices with new materials [4]. This processing technique is expected to reduce the costs of the microparts by choosing low-cost materials to ensure greater dimensional freedom of the fabricated parts and enhanced physical and mechanical properties of the materials chosen for the MEMS devices.

The LIGA-process represents a sequence of microfabrication steps combining a step of deep X-ray lithography and subsequent additive processing of plating-through mask and molding. Thus, a wide variety of products with diverse functionalities can be achieved depending on the fabrication route chosen among the fabrication possibilities offered by LIGA.

The LIGA technology provides unique advantages over other manufacturing methods, some of them are listed below:

- Very large structural heights varying from hundreds to thousands of micrometers and the smallest lateral dimensions of a few micrometers with structural details in the sub-micrometer realized in one single step (Figure 2.1).

- The access to a large variety of materials including electrodeposited metals and alloys, molded polymers [5], ceramics, composites, multilayered material. The intention of the development of these materials is the commercial production of microcomponents by the replication techniques offered by LIGA (electroplating, molding).
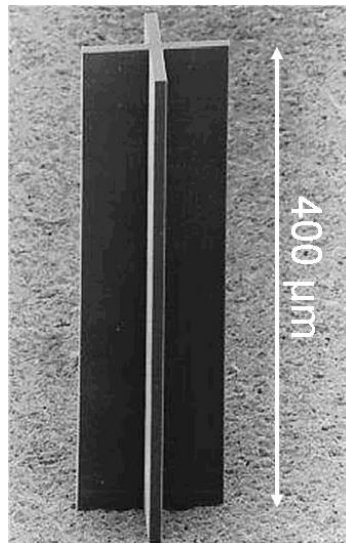
Figure 2.1: SEM-figure showing a LIGA micro resist column with 400 μm height and relatively small lateral dimensions of few μm .

- The structural accuracy of the features shown by the LIGA components:
  - Precise shape definition: straightness and planarity of sidewalls, well-defined lateral dimensions of a few micrometers
  - Low surface roughness of the side-walls (rms (root mean square) roughness of 20 nm or better), sufficient for micro optical components [6]
  - Extreme parallelism/verticality of sidewalls with slopes of the order of 1 mrad [7]

- Combination with other microfabrication techniques are possible, such as: sacrificial layers used to manufacture movable microsystems (e.g. LIGA gears in Figure 2.2), spark plasma sintering used to produce microparts made of ceramics or alloy [3]

- Collective manufacturing by parallel processing of microcomponents (batch fabrication) to reduce the cost of fabrication

The features mentioned above are a requirement for various important applications fields:

- Micromechanical devices including precision actuators and mechanisms, such as:
  - Moving elements showing high accuracy and tight tolerance when produced by LIGA, for example miniaturized gear systems [8], bearings [9]

Figure 2.2: LIGA Gears made of various metallic materials (nickel alloys, cobalt alloys, gold alloys).

- Mechanical sturdy devices, e.g. micro-motors, -rotors and -drivers with appreciable torques [10], microturbines generating power for a variety of applications, micromechanical actuators for electrical switches and relays

- Nozzles for the use in spinnerets for textile fiber [11], ink-jet printing type applications, etc.

- Mold inserts for a number of replication techniques [12], [13], [14]

- Micro optical components and systems [6] made of polymers produced in a large number (replication process) reducing the manufacturing costs, for example, optically based sensors (e.g. microspectrometers for different wavelength ranges)

- Microfluidics and bio-MEMS including devices for medical/biological applications and chemical and biotech systems, e.g. reaction chambers, integrated heat exchangers [15], micropumps, etc.

Despite the various strengths offered by LIGA, the development of this fabrication process is still mostly limited to labs scales. However, the mass production of polymer parts by molding becomes more recognized by industries, which push the fabrication of molding inserts forward. More work still has to be invested till the LIGA technique becomes well commercialized.

2.2 Electrodeposited metals

As mentioned in 2.1, the end product manufactured by LIGA varies depending on the needed material and number of parts. One possible product is a metallic micropart obtained after the electrodeposition step. These metallic structures have proven to be more fracture resistant than silicon-based devices that are the most commercialized products in the field of MEMS applications. The balance of properties that electrodeposited metals offer (high electrical and thermal conductivity, relatively high stiffness and strength and very high fracture toughness) makes them extremely attractive for a number of MEMS applications. Examples of electrodeposited materials available for MEMS applications include, arranged from the most developed material to the less developed one: Ni, Co, Au alloys, Ni alloys, Co alloys and nanocomposites.

Previous work has demonstrated that the properties of the material mentioned above, such as crystallographic texture, internal stresses, ductility, etc., are sensitive to processing conditions (e.g. plating current density, bath temperature, chemistry) [16]. That means that the fabrication process has to be optimized according to the requirements of the material functionality.

Among others, electrodeposited nickel (ED Ni) represents one of the most used electroplated metals for MEMS applications especially as structural material for mold inserts (e.g. mold insert for a MEMS microspectrometer, see Figure 2.3). Ni electroplating, first
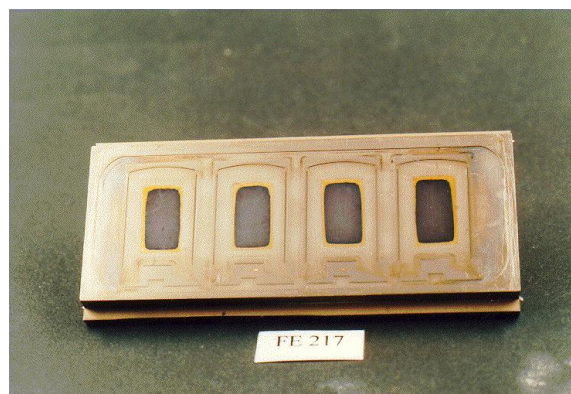
Figure 2.3: LIGA mold insert (Ni) for the fabrication of a commercially available microspectrometer (Boehringer Ingelheim - MicroParts, Germany). A batch of four microspectrometers can be fabricated during a single hot embossing step.

introduced in the 19th century, is studied in earlier works in terms of process parameters

and mechanical characterization of coatings and microparts. The electroplating community has shown that ED Ni is generally deposited with columnar or refined fibrous grain morphology and an out-of-plane crystallographic texture that depends on the plating parameters (bath composition, current density, pH, temperature and agitation) [17], [18], [19]. More recent studies in [20] and [21] have shown that ED Ni can be deposited in nanocrystalline form. These observations can be used to explain the wide variation in mechanical properties that was uncovered in a recent study of a LIGA Ni MEMS fusing/safing and arming device that was conducted at Johns Hopkins University (JHU) and reported in [22] and [23]. More details about the mechanical behaviour of ED Ni will be discussed in paragraph 2.4.

In order to extend the applicability of the material in general and particularly of ED Ni, some alloying elements are electrodeposited into the nickel matrix or a new phase in the form of small sized particles is co-deposited. Both methods used to enhance the capability of the material are illustrated in the next paragraphs (2.2.1 and 2.2.2).

2.2.1 Electrodeposited Nickel alloys

In the last decade, alloy plating has aroused more and more interest as the (electroplating) technology development associated with applications in the field of electronics and automotive industries, such as electronic contacts, printed circuits, bearings and corrosion protection of steel plates, increases.

A wide variety of binary and ternary alloys has been developed with regard to the functional property to be influenced, the most important being zinc alloys, tin alloys, nickel alloys, and noble metal alloys. Ni alloys specifically are illustrated in the following paragraphs, in terms of functionality added by the alloying element.

Ni-Fe has been used in diverse industrial applications for over 100 years ([24], [25]) thanks to its physical and mechanical properties. In fact, the low thermal expansion coefficient and the relatively high strength make nanocrystalline Ni-Fe alloys attractive especially for integrated circuit packaging and shadow masks for cathode ray tubes. Both of the latter properties also permit the use of Ni-Fe alloys in micro-electro-mechanical systems since this material improves the performance of the component in terms of specific strength, elastic energy storage and thermal shock resistance [26]. In addition, Ni-Fe alloys show good soft magnetic properties, which are suitable to several applications such as electromagnetic shielding, read-write heads, magnetic motors and actuators. One more

property advancement resulting from alloying is increasing the oxidation resistance by adding Cr and Mo to Ni-Fe alloys as mentioned in [27].

Ni-Mn also presents a promising nickel alloy that improves the performance of MEMS devices in terms of electrical and mechanical properties. [28] and [29] illustrate the influence of the addition of a small amount of Mn ($\leq$ 1 at%) to electrodeposited nickel, consisting in the negligible change of the electrical resistivity and the strength when exposed to high temperature (up to 600 ^{o}C). Alloying with P plays a relevant role in the field of surface engineering since it enhances the performance of coatings from point of view of wear and corrosion ([30], [31]).

In addition to the common alloying elements mentioned above, W can be co electrodeposited with nickel in order to improve the strength and the elastic behaviour of ED Ni [32], see for instance HF-contact elements for testing and multi chip module applications made of Ni 2.31 wt% W [33]. The abrasion and wear resistance is also enhanced by the alloying element W as demonstrated in [34] and [35]. A literature search [36] indicates that Ni-W alloy can be made by electroplating and may provide significant thermal stability. Ni-W was initially targeted for improved wear and high temperature resistance, but the low diffusivity of W in Ni also results in increased microstructural stability as shown in Figure 2.4, which presents field ion images of as-deposited state and specimens annealed at temperatures between 400 and 800 ^{o}C for 10 h. The randomly arranged image spots seen in the first three images in Figure 2.4 a-c correspond to the nanocrystalline structure of the disordered fcc Ni-rich phase surrounded by W rich regions (grain boundaries). Due to the low diffusivity of W, the grain growth of the disordered Ni rich fcc phase is inhibited and the nanocrystalline structure is preserved even at 700 ^{o}C, as shown in Figures 2.4 a-c. Only after heat treatment at 800 ^{o}C does the ring pattern (Figure 2.4 d) of the size of 10 to 20 nm corresponding to the intermetallic Ni_4W phase develop. The latter effect confirms the diffusion of tungsten to the regions where the new phase is formed. As a result, the growth of the grains, shown to be stable till 700 ^{o}C, is enhanced.

As mentioned in the examples above, a wide variety of nickel alloys is available for diverse applications. Nevertheless, development of nickel alloys in regards to high temperature MEMS applications needs to be examined further in order to investigate the microstructural and mechanical properties of the electrodeposited alloys with respect to the length scale of MEMS microparts.
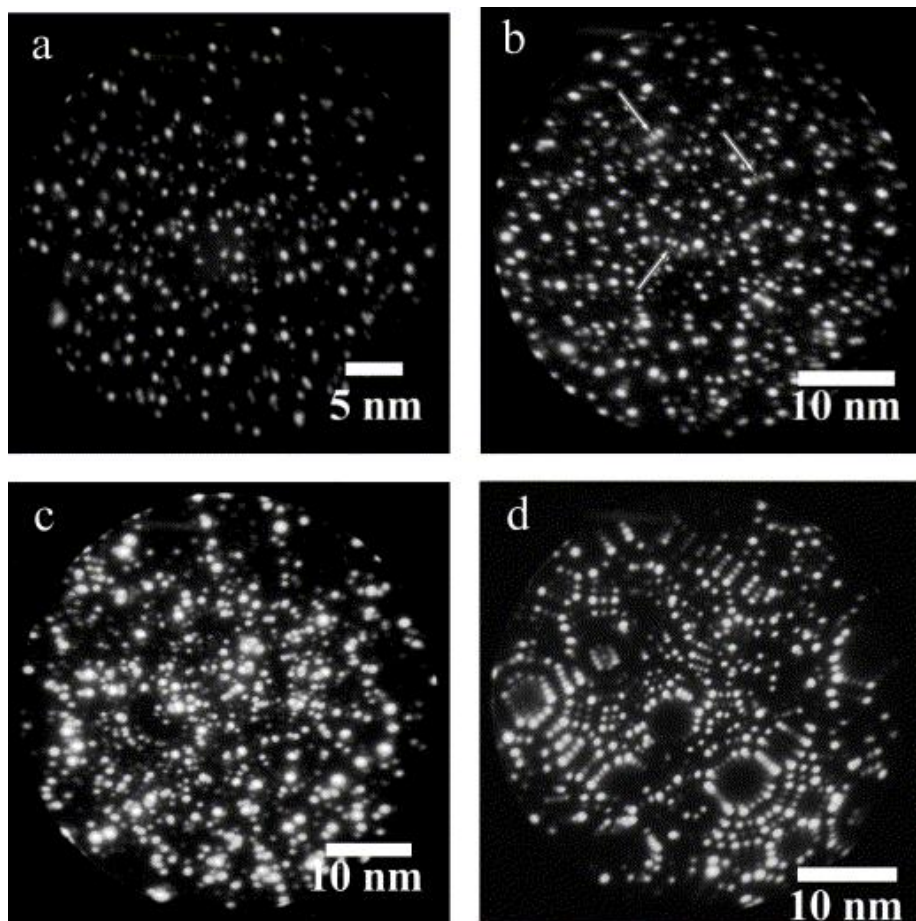
Figure 2.4: Field ion images (5×10^{-5} mbar Ne at 20 K) of electrodeposited Ni 18 at% W: (a) as-plated; (b) 400 ^{o}C, 10 h; (c) 700 ^{o}C, 10 h; (d) 800 ^{o}C, 10 h [36].

2.2.2 Electrodeposited composites

Electrodeposited composites consist of a metallic matrix containing a dispersion of small particles ranging in size from sub μm to 100 μm in diameter. The embedded particles can be made of pure metals, ceramics or organic materials. The available metal matrices, in which the particles are incorporated, are electroplated Cu, Ni, Co, Cr and various alloys. The composites are electrodeposited in the form of coatings used essentially for protection against oxidation and hot corrosion and as wear and abrasion resistant surfaces ([37], [38], [39], [40], [41].

The mechanism governing the electrocodeposition was studied in several previous works and different hypothesis were proposed. Martin and Williams [42] suggested that electrocodeposition was due to the mechanical entrapment of the particles by the electrodeposited metal. Snaith and Groves [43] supported this proposition based on their observation that the incorporated particles fell out when mechanically polished and etched. This effect proved that there was no bond between the particles and the surrounding metal matrix. Guglielmi [44] developed also a model describing the electrocodeposition of particles into a metallic matrix. This model is based on two consecutive adsorption steps, termed the loose and strong adsorption, in which the combined effect of adsorption of particles and electrochemical reduction of particle-bound ions is held responsible for the encapsulation of particulate matter in a growing electrodeposit.

As mentioned above the electrolytic codeposition of particles with metals is far from being fully understood, so that the influence of electrolysis parameters on the codeposition cannot yet be predicted. Notwithstanding this, from the available information on composite plating practice some rules can be derived about the influence of some important plating parameters on the incorporation of the particles into the metal matrix. Several of these parameters include:

- Hydrodynamics: the agitation of the electrolyte is relevant to maintain the particles in suspension; for instance, rotating the electrode cells as mentioned in [45].

- Current density: the effect of the current density varies in dependence of the deposition system. For example, for Ni-TiO$_2$, the increase of the current density results in an increase of the amount of incorporated particles [46]; which is not the case for the co-deposition of alumina in nickel showing an unchanged composition of the layer when varying the particles concentration [47].

- Bath chemistry: pH, bath components and temperature show different influences on the composition of the composites.

- Particle characteristics: this includes composition, crystallographic phase, size, density and shape. The amount of co-deposited alumina in nickel for example, decreases with a decreasing particle size [48], in contrast to alumina in the silver matrix [49].

In this work, we concentrate on co-deposition of nanoparticles (nominal diameter of the particle in the range of several 100 nm or $\leq$ 100 nm). The nanoparticles are co-deposited in the layer, not in the form of isolated particles but in form of agglomerates, as demonstrated in [50] because of its high surface energy. The phenomenon of agglomeration influences the amount of the particles embedded and the distribution of the agglomerates in the electrodeposited layer and microparts. Wang et.al [51], for example, demonstrated the non-uniform distribution of the ceramic Al_2O_3 particles in high aspect ratio structures 2.5. This may prove that the particles are particularly difficult to incorporate in very small high aspect ratio structures.
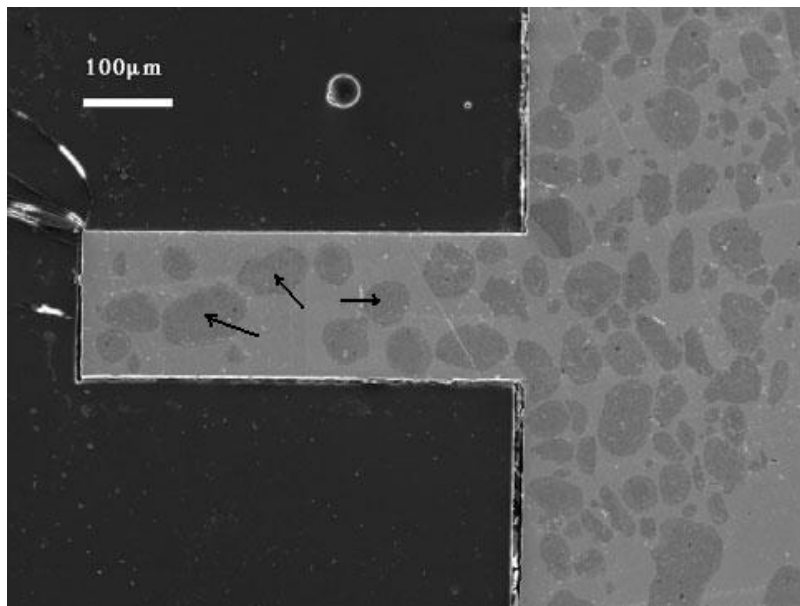
Figure 2.5: SEM cross sectional micrograph of a Ni-Al_2O_3 post grown from a bath containing 25 g l^{-1} Al_2O_3 particles: particles agglomerates in both post and overplated layer [51]. Several Ni-Al_2O_3 agglomerates are indicated by arrows.

Many previous works tried to study the agglomeration effect to find a solution how to control it. The agglomeration tendencies depend especially on the bath chemistry. In fact,

according to the studies completed by [52], the nickel ions concentration and the pH of the solution affect the agglomeration of the particles controlled by the adsorption of the nickel ions on the particle surface.

Electrolytic codeposition offers, in addition to changing the composition of the pure metal or alloy matrix, the possibility to to form alloys that are difficult to obtain by straight electrolysis such as stainless steel resulting by diffusion of chromium from chromium particles codeposited with an iron-nickel matrix [16] and Ni-Al alloy as a result of the diffusion of aluminum from aluminum particles in the nickel matrix. Ni-Al alloy in general, resulting from the method described above, and Ni-based superalloy, in particular, presents an issue of this work. Macro Ni-based superalloys are employed in load-bearing structures at the highest homologous temperature (0.9 T_m, T_m: melting temperature) of any common alloy system and are used extensively at the hot sections of turbine engines. Their high temperature strength is related to the formation of a coherent γ - γ' microstructure. The continuous matrix phase (γ) is fcc-Ni while the primary strengthening phase (γ') is an Ll2 intermetallic, Ni_3Al. From the presence and distribution of the γ' - phase, the high temperature strength and microstructural stability of the Ni-base superalloys is derived, as mentioned in section 2.4 concerning the deformable particles. Thus improving the high temperature performance of electrodeposited Ni by formation of γ'- Ni_3Al precipitates, as is done in Ni superalloys, will require the addition of Al. Aluminum is an extremely active metal and cannot be electrolytically reduced from a water solution because water separates into hydrogen and oxygen first. Organic solvents can be used to deposit Al [53], but there are serious limitations to the use of co-electrodeposition of Ni and Al and we propose to incorporate Al particles into standard LIGA Ni deposits to develop LIGA Ni-Al alloys. The entrainment of Al particles in ED Ni has been accomplished by several investigators. Zhou et al. ([54], [55]) developed a Ni 28 wt% Al nanocomposite coating for oxidation resistance by electrodeposition of Ni with 75 nm Al nanoparticles. These nanoparticles were dispersed in a nanocrystalline Ni matrix. A superior high temperature oxidation resistance was noted, but no attempt was made to optimize the γ - γ' microstructure or to characterize the mechanical performance of the films. Meng et al. [56] have magnetron sputtered γ - γ' multilayer films with good mechanical properties and Li at al. [57] fabricated similar γ - γ' microlaminates with EB-PVD, but neither of these techniques produces thick or robust enough films to be used as LIGA structures. These experiments point at the possibility of making ED Ni with entrained Al particles. Nevertheless, literature does not provide a

consistent description of the codeposition process and the resulting Ni-Al composite either in form of layer or microparts.

In conclusion, more efforts in the field of co-deposition of particles, especially the nano-sized ones used in MEMS microfabrication, have to be invested. The diameter of the nanoparticles agglomerates shown to be inevitable should be kept as small as possible (in the range of a few hundred nm) in order to ensure the incorporation of the agglomerates in the electrodeposited microparts and result in a relatively homogeneous distribution.

2.3 Micro electroplating

Micro electroplating represents an important process step within the LIGA technique. It consists on the electroplating of metals and alloys into photo-resist patterned polymer layers, which are fabricated by LIGA. The LIGA process is described in Figure 2.6. In the
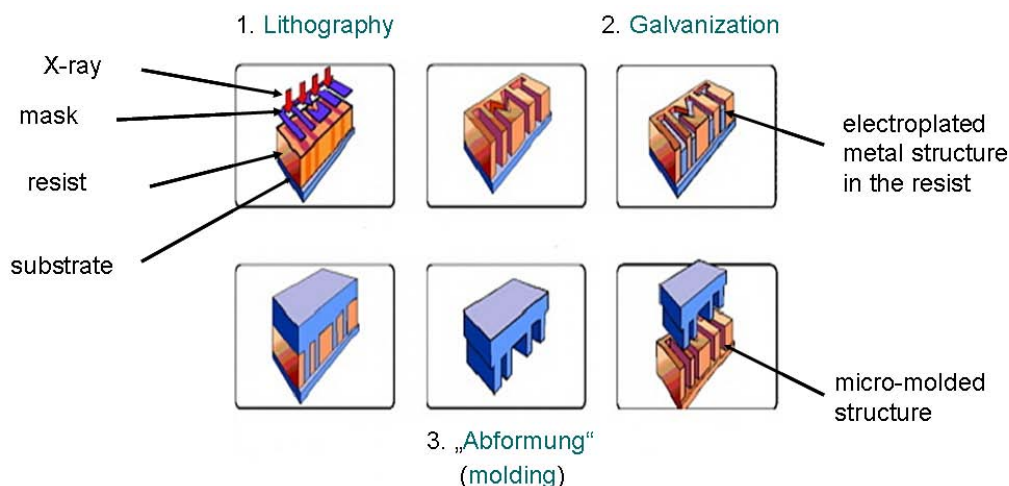
Figure 2.6: LIGA process

first step of micropattern fabrication, an X-ray sensitive resist layer is glued on a conductive substrate. The substrate covered by a mask is irradiated with X-rays transferring the pattern from the mask to the substrate. The irradiated pattern is then removed. Thereafter, depending on the material and the number of parts selected for the final product, different fabrication ways can be chosen:

- the polymeric structure as a final product if released from the substrate

- production of metallic microparts using the polymeric structure as electroplating template

- fabrication of molded parts made of diverse materials using an electrodeposited metallic mold

This work deals with the production of metallic microparts resulting from electroplating. In general, electroplating is the process of producing a coating, usually metallic, on a surface by means of electric current. This electrochemical technology entered the electronics industry some 50 years ago as a manufacturing process for low-end printed circuits boards. Nowadays, it is employed widely for the processing of advanced microelectronic components, including Cu chips, high -end packages and interconnects and micro-electromechanical systems MEMS (e.g. sensors and actuators). The electroplating process is summarized in the schema presented in Figure 2.7. This process is realized in
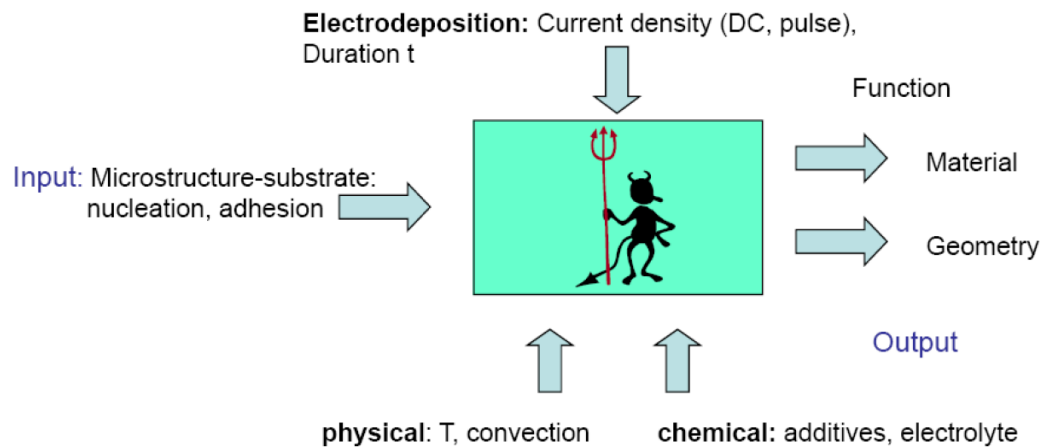
Figure 2.7: Schematic representation of the electrodeposition process and its parameters

an electrolytic cell shown in the Figure 2.8. The electrodes and the metallic connector enable the conduction of electrons when an electrical potential is applied. In the electrolyte, which represents mostly an aqueous solution, the electricity is conducted ionically. Positive ions A^+ (cations) move toward the cathode and produce a layer of A (electrodeposit) with respect to the reduction reaction $A^+ + e^- \rightarrow A$. On the anode an oxidation reaction such as $B^- \rightarrow B + e^-$ takes place.
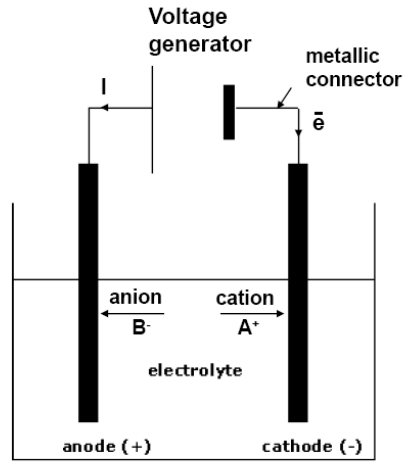
Figure 2.8: Electrolytic cell

The relationship between the charge and the deposited mass is given by the Faraday's law summarized in the following equation:

$$d = \eta \cdot \frac{M}{z \cdot F \cdot \rho} i \cdot t \tag{2.1}$$

where d is the electrodeposit thickness, η is the current efficiency, M is the molar mass of the reduced element, z is the number of exchanged electrons, F is the Faraday constant, ρ is the material density, i is the current density and t is the electrodeposition duration. The current density i depends on diverse parameters including the chemical composition of the electrolyte, the operating temperature and Reynolds' number.

Electrochemical fabrication offers some unique advantages over competing technologies such as vapor phase technologies, making it more attractive for the electronics and microsystems industry. Indeed the achievable precision is shown to be high and from an environmental point of view the produced waste is minimized since the material deposition is highly selective.

The electrochemical principles governing the micro electroplating have been studied in several previous works ([58], [59], [60], [61], [62]). The basic principles consist of current density distribution and mass transport.

The current density distribution can be influenced by the inhomogeneous coverage of the active areas as demonstrated in the literature ([63], [64]). This effect can be avoided through introduction of additional areas on the substrate that have to be electrodeposited.

One more aspect affecting the current density distribution is the resist thickness. When increasing the resist thickness, the shielding effect shown by the resist increases which homogenizes the current distribution [65]. Hence, as a rule for electroplating, thicker resist layers and lower filling ratios are recommended. Mass transport during micro electroplating involves the ion transfer from the bulk electrolyte to the cathode surface by convection, diffusion and migration. A homogeneous composition distribution of the electrodeposited alloy and a compact deposit require lower current densities as reported in [66]. The current density is in dependence on the diffusion zone, where the electrodeposition is controlled by diffusion. In fact, the reduction of the metal ions concentration near to the cathode results in a depletion zone, called diffusion zone, in which the concentration gradient is adjusted by diffusion.

The aspects mentioned above present a correlated phenomena and their optimization to obtain a successful micro electroplating is a complex task especially when additional parameters play a role in the homogenization of electrodeposited microstructure. Unlike the case of macroscopic substrates, the homogenization of electrodeposits is relevant for further use of the microparts since the small defects destroy their function.

2.4 Microstructural stability and mechanical behaviour

An accurate knowledge of mechanical properties is required for the design of a large number of LIGA MEMS applications. The well-known fine grain structure of electrodeposits, representing the type of material to be studied in this thesis, yields mechanical properties that are unique to electrodeposition and different from those of bulk material showing the same chemical composition. Furthermore, mechanical properties of electrodeposits are a function of the electrodeposition technique that involves bath chemistry, agitation and current density. Another influencing factor is the size of the microparts. At the microscale, certain mechanical properties differ from those of conventional, macroscale components and devices. For example, strength has been reported to be significantly increased for

MEMS [67], [68]. Among the reasons for this different behaviour of the mechanical properties of MEMS are the change in microstructural parameters like grain size, and the increase of surface to volume ratio, which increases the influence of surface effects on the mechanical behaviour of microparts. It is therefore clear that the mechanical behaviour of MEMS materials has to be characterized at the same length scale as they will be produced and used.

The mechanical test methods of microscale materials may be, in general, distinguished between on-chip testing devices (i.e. [69] and [70]) and ex-situ testing devices where specifically microfabricated specimens are tested on separate micro testing systems that are used to apply external loads and measure both force and strain. Good overviews of the various ex-situ tensile testing methods are given by Allameh [68], Sharpe [71] and Ilzhöfer [67]. These testing systems are similar to standard macro test machines. The non-contact strain measurements methods used here, however, are different. The strain measurement method used by Allameh is based on image correlation techniques, while Sharpe uses the interferometric strain displacement gage (ISDG) and Ilzhöfer the shadow-optical principles using an infrared collimator. Most of these tensile testing machines operate at room temperature except the machine developed by Sharpe, which was recently modified by [72] for elevated temperature use.

Several studies have been reported on determining the mechanical properties of the electrodeposited material. The microstructure of the electrodeposits has been shown to be nanocrystalline with an average grain size and range of grain sizes smaller than 100 nm depending on the electrodeposition parameters. This grain refinement leads to the strengthening of the material rationalized on the basis of the Hall-Petch effect ([73], [74], and [75]). One possible cause for this refinement is the effect of a dislocations pile up at grain boundaries. With further grain refinement (smaller than 10 nm) weakening of the material can happen (Figure 2.9). Electrodeposited Nickel was investigated in many works that illustrated the effects mentioned above. The results conducted by Cho [77] showed the influence of the current density on the microstructure of the obtained material and therefore, with respect to the Hall-Petch relation, the effect on the tensile strength at room temperature (see Figure 2.10). It is worth noting that the high temperature exposure of some metals results in loss of mechanical properties related to microstructural instabilities impeding the use of these materials for several MEMS applications. ED Nickel is a good example explaining this phenomenon. Samples stress-strain curves conducted at high temperature from previous studies at JHU (see Figure 2.11) show the significant loss
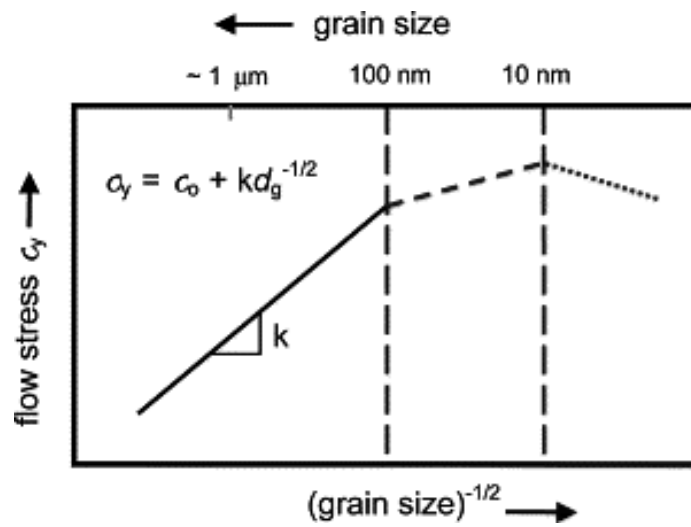
Figure 2.9: Schematic representation of the variation of yield stress as a function of grain size in microcrystalline, ultrafine crystalline and nanocrystalline metals and alloys [76].
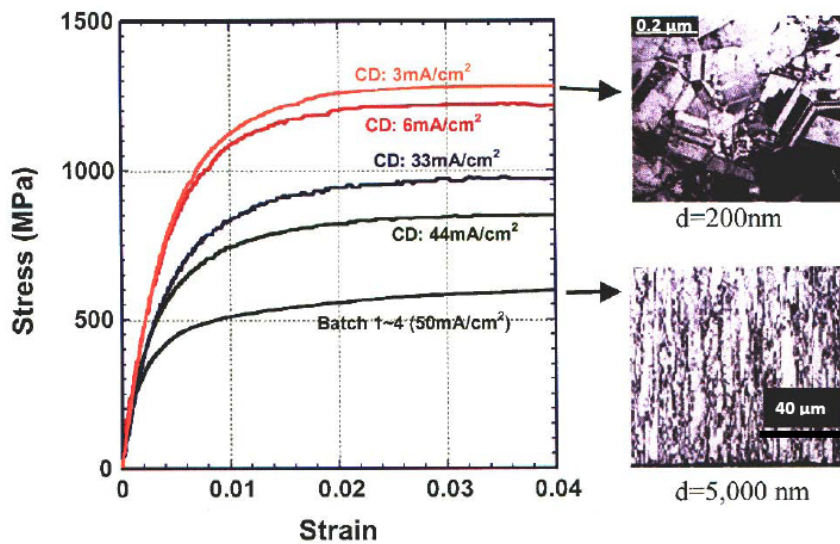
Figure 2.10: The effect of electroplating current density on the grain size and overall mechanical response of LIGA Ni structures [77].

of strength at temperatures as low as 200 ^{o}C. This decrease in strength has been related to coarsening of the as-deposited microstructure, which deposited far from its equilibrium state [77], becomes unstable at temperatures as low as 70 ^{o}C [78].
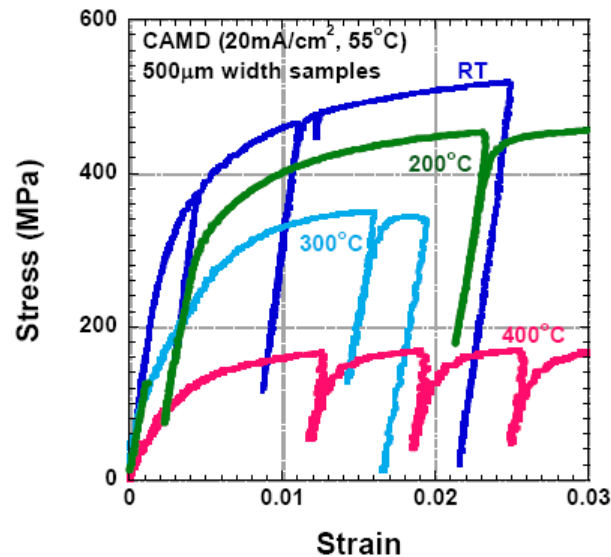
Figure 2.11: Stress-strain curves of pure nickel at various temperatures [77]

In order to enhance the thermal stability of the electrodeposited material, some solutions have been proposed in the literature including strengthening ensured by solid solution, second phase particles or forming nanocomposites.

In the case of solid solutions, the alloying element segregates in the grain boundaries. This segregation inhibits the grain growth during heating and maintains the microstructure stability even at high temperature as shown in [79], where Ni-P alloy stays stable at temperatures up to 400 ^{o}C.

A second phase, in form of dispersed particles contained in metal matrix composites, may also maintain the microstructure at high temperature by exerting a significant pinning effect on both low and high angle grain boundaries. The second phase particles could be in the form of high temperature stable particles such as ceramic particles (e.g. Al_2O_3, SiC, SiO_2), or coherent particles resulting after precipitation such as γ' - phase in Ni superalloys.

The annealing behaviour of these materials depends strongly on the particle parameters consisting in volume fraction, size, shape and spacing of the second-phase particles.

The effect of these parameters on the grain growth and recrystallization of the material was studied in previous works. In Figure 2.12, it has been shown that with a sufficiently small spacing of ceramic particles as a result of high volume fraction of the incorporated particles, it is possible to preserve the microstrucure up to the melting point.
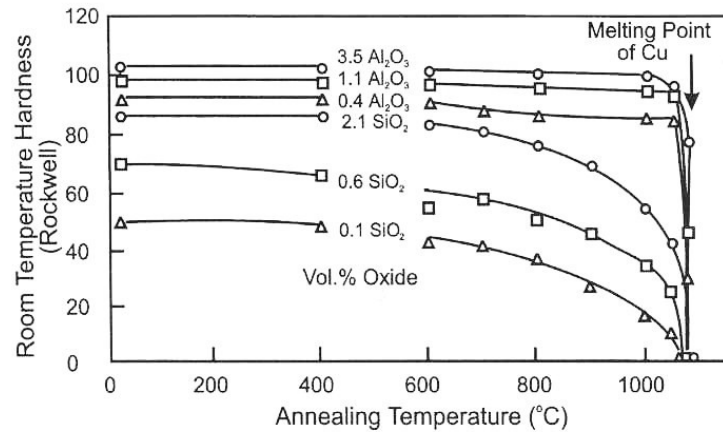
Figure 2.12: The room temperature hardness of extruded and annealed dispersion-strengthened copper alloys [80]

The variations of the particle size and interparticle spacing were also examined in [81] and [82]. The bigger particles incorporated in the matrix (diameter larger that 1 μm) and the larger interparticles spacing is, the faster occurs the recrystallization, see Figure 2.13 and Figure 2.14.

The effect of the particles on preserving the microstructure can be explained by the interaction of the particles with the grain boundaries. In fact, a dispersion of particles exerts a retarding force or pressure on a low angle or high angle grain boundary and this may have a profound effect on the process of grain growth. This effect is known as Zener pinning pressure P_Z, which is given by [83]:

$$P_Z = \frac{3 F_v \gamma}{2 r} \tag{2.2}$$

where F_v is the volume fraction, γ is the specific energy of the boundary and r is the radius of the spherical particle. The magnitude of the Zener pressure is dependent on the interface and the particles parameters (shape, size, spacing, volume fraction).

The thermal stability of the microstructure, due to the particles' incorporation, is in most cases accompanied by improving mechanical properties (strength and creep resistance)
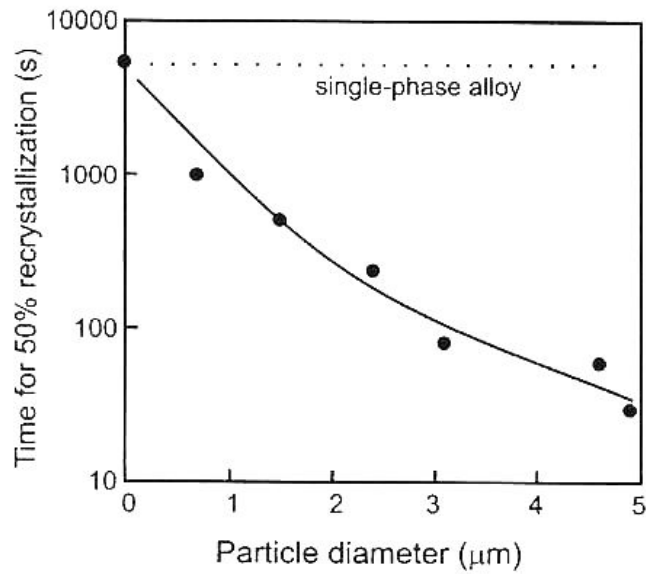
Figure 2.13: The effect of particle size on recrystallization in Al-Si alloys reduced 50 % by cold rolling and annealed at 300 ^{o}C: the time for 50 % recrystallization [81].
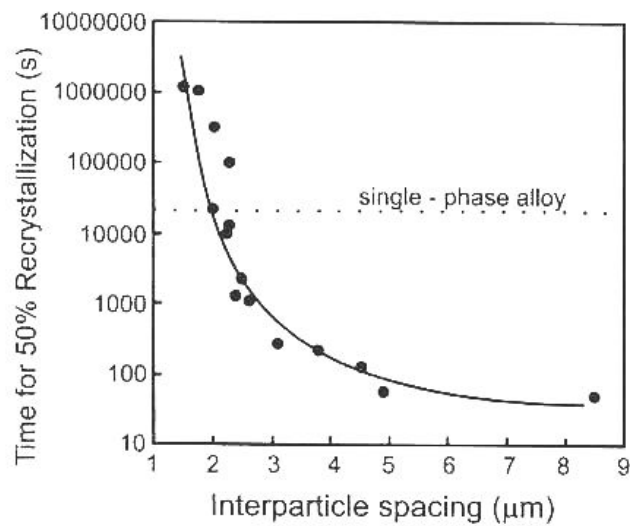
Figure 2.14: The effect of interparticle spacing on the recrystallization of Al-Cu single crystals reduced 60 % by rolling and annealed at 305 ^{o}C: the time for 50 % recrystalization [82].

21

at high temperatures. According to Orowan's report, particles' strengthening caused by non-deformable incoherent particles, was also mentioned in [84], [51] and [85]. In fact,
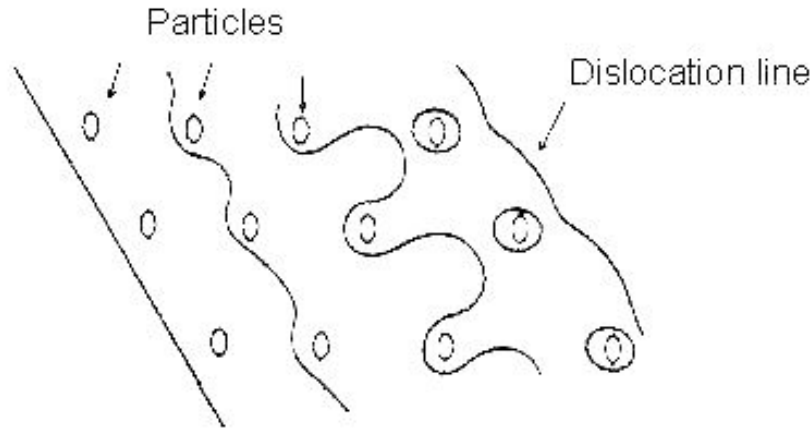
Figure 2.15: Schematic image of the Orowan mechanism

according to the Orowan dislocation bowing model as demonstrated in Figure 2.15, the shear yield stress (τ_y) associated with dislocation bowing around the particles is expressed as following:

$$\tau_y = \frac{G b}{\lambda} \tag{2.3}$$

where G is the shear modulus of nickel matrix, b is the magnitude of the Burger's vector, λ is the average particle center to center distance. τ_y increases when decreasing the distance between the dispersed particles in the electrodeposits. The decrease in the distance is ensured only if the particles incorporated are nanosized and hence well-dispersed [51].

In the case of nanocomposites containing a coherent second phase, the Orowan type of particle strengthening is not expected. This deformable second phase is supposed to be sheared by the dislocation (Figure 2.16). The diameter of the particle is thus reduced which leads to the formation of dislocations slips. This is of particular concern in the design of high strength precipitation hardened alloys such as Ni base superalloys.

As seen in this paragraph improving the microstructural stability at high temperature is feasible with respect to one of the mentioned strategies. Accordingly, the electrodeposition process has to be optimized in order to result in the desired material composition and structure (alloying element content, particles parameters).
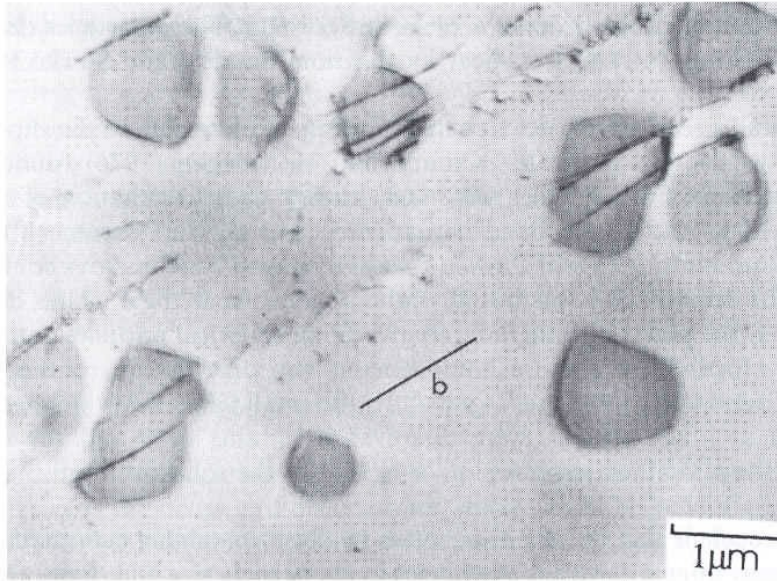
Figure 2.16: Deformed Ni$_3$Si particles in Ni 6 % Si single crystal [86]

2.5 Aims of this work

The principle purpose of this work is to enhance the high temperature capability (microstructural stability and better mechanical properties) of electrodeposited nickel for the use in the fabrication of LIGA microparts. This can be ensured either by alloying or by adding a second phase (coherent or incoherent). Alloying with W has been demonstrated to be feasible by electroplating and also presented a stable microstructure at high temperature (see Section 2.2.1). Ni-W alloy consequently is planned to be electroplated in the form of layers and micro specimens. Compositional optimizations are guided by the microstructural stability of the material at high temperature (up to 700 ^{o}C) and its mechanical performance at room and high temperature.

Ni-Al$_2$O$_3$ presents the electrodeposited nanocomposite, containing an incoherent second phase, of interest within this thesis. The proposed route to better the stabilization of the electrolyte and the homogeneity of the particles distribution in the deposits is to add chemicals shifting the isoelectric point far from the working pH-range. By means of this strategy, 100 μm thick layers and microspecimens showing homogeneous distributed particles are expected to be electrodeposited. On this material, microstructural observations and mechanical characterization will be used to evaluate the followed electrodeposition strategy and the capability of microstructural stability at high temperatures (up to 600 ^{o}C).

Last not least Ni superalloys, that are known with their attractive properties at high temperature, will be developed by electrodepositing Ni-Al nanocomposites. The challenges to overcome in the development of LIGA Ni-base superalloys involve incorporation of Al powders into thick Ni electrodeposits (thickness $\geq 50\ \mu$m) to be used in microtechnology applications, and identification of an appropriate heat treatment that will allow for diffusion of Ni and Al in order to form γ' precipitates with proper morphologies. Microstructural investigations are used to identify optimum processing parameters.

3 Experiments and Characterization

In this chapter, the experimental steps to determine the mechanical properties of the suggested materials are explained. Specifically, the production of the needed material in the form of layer- and microspecimens, the microstructure investigations using adequate microscopy methods and the mechanical characterization concentrating on the exposure at high temperatures, will be clarified.

3.1 Microspecimens fabrication

3.1.1 Electroplating

The electroplating of the layers and the microspecimens investigated in the current work is realized by an electrolytical cell as explained in Figure 2.8 in Section 2.3. The cell consists of a cylindrical glass vessel covered with a plastic foil in the case of layer electrodepositing in small electrolyte volumes (500 ml)and with a PMMA-cover in the case of microspecimens' electrodeposition in an electrolyte with a volume of 2 - 3 L, in order to limit the loss of ammonia as well as water vapour during deposition.

Soluble nickel pellets or platinized titanium are used as soluble or inert anode, respectively, for the electrodeposition. The reactions occurring at the anode consist of the oxidation of nickel in the case of the soluble anode presented in the following chemical equation:

$$Ni \rightarrow Ni^{2+} + 2e^- \tag{3.1}$$

and the formation of O_2 gas in the case of the inert anode according to the equation:

$$2\,OH^- \rightarrow 1/2\,O_2 + H_2O + 2e^- \tag{3.2}$$

The layer deposition is done either on polycrystalline copper substrates of 20 mm diameter and 1 mm thickness or on a brass sheet, on which a window with a several cm^2 area is defined for the electrodeposition. The microsamples used for the mechanical characterization are electrodeposited into a micropatterned window on a Si-wafer shown in Figure 3.1 and presenting an area of 770.8 mm^2. This wafer will be described in details in Section 3.1.2.
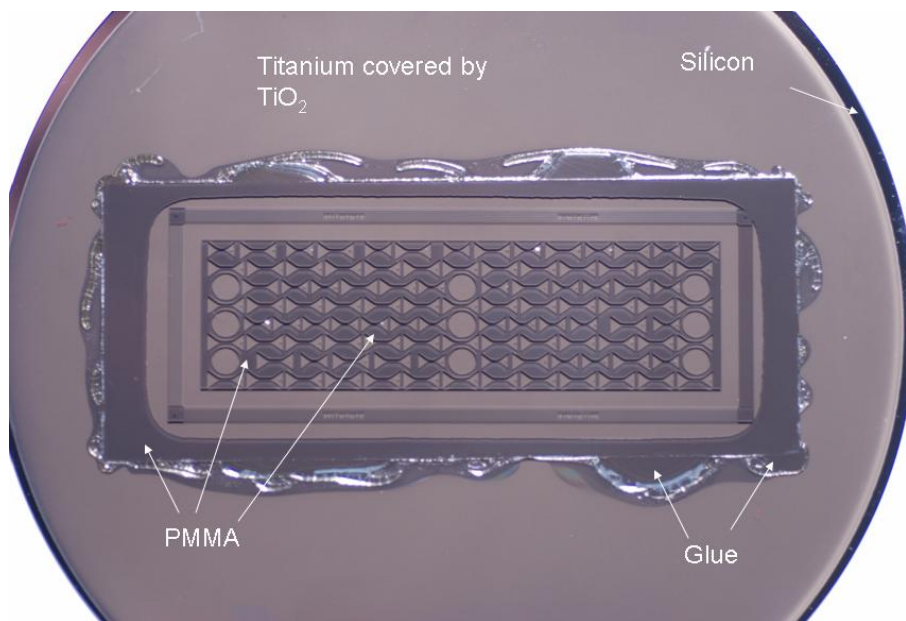
Figure 3.1: Photograph of the electrodeposition window (A = 770.8 mm^2) on a silicon wafer before electrodeposition. The wafer is metalized on the top surface with a 2.5 μm Ti film covered by an nanoporous oxide layer. A micropatterned PMMA - resist is glued on the Si - Ti - TiO_2 substrate.

When preparing the electrolyte containing the particles (dispersion), the particles are mixed into the electrolyte by a high speed stirrer shown in Figure 3.2.

During the electrodeposition, agitation of the bath and well defined current density are required. In the experiment described above, the current and the stirring velocity are provided by a current source and a magnetic stirrer fabricated by FUG and Heidolph, respectively.
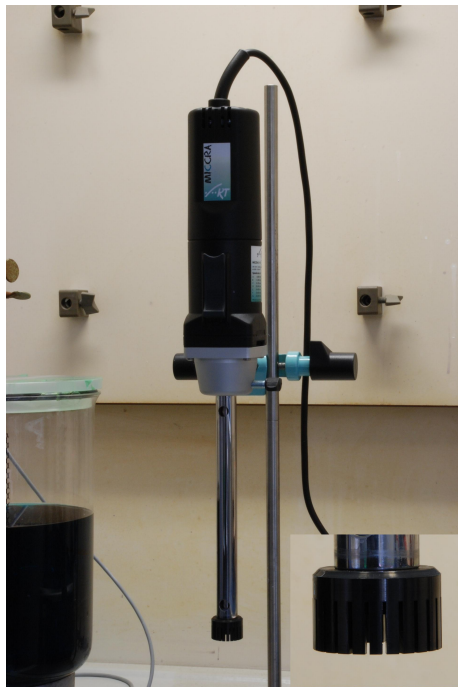
Figure 3.2: Dispersing high speed stirrer (MICCRA)

3.1.2 Micropattern fabrication by LIGA

The studies in this work concentrate on the production of LIGA metallic microparts by electrodepositon (see Figure 3.3). The microparts resulting from the wafer available within this thesis (Figure 3.1) comprise micro tensile specimens, micro fatigue specimens and TEM discs as indicated in Figure 3.4.

The microspecimens are fabricated on a 100 mm Si wafer metalized on the top surface with a 2.5 μm Ti film by sputtering (HL-Planartechnik, Germany). The top surface of Ti is oxidized in NaOH/H_2O_2 at 60 ^{o}C to form a nanoporous oxide layer for better adhesion.

A 300 μm thick resist layer made of polymethylmethacrylate (PMMA) which is a positive single component photoresist is glued on the wafer. An X-ray working mask is placed on the photoresist coated surface at a proximity gap of 10 μm. After exposure to X-ray radiation, PMMA becomes soluble through chain scission caused by the deep X-ray illumination. A GG-developer is used to dissolve the irradiated resist parts.

A sacrificial copper layer with 10 μm thickness is electroplated on the wafer from a conventional copper electrolyte including $CuSO_4$, H_2SO_4, HCl and some additives. The latter, consisting in PRIMUS CD system produced by Hesse and Cie, Germany, are used
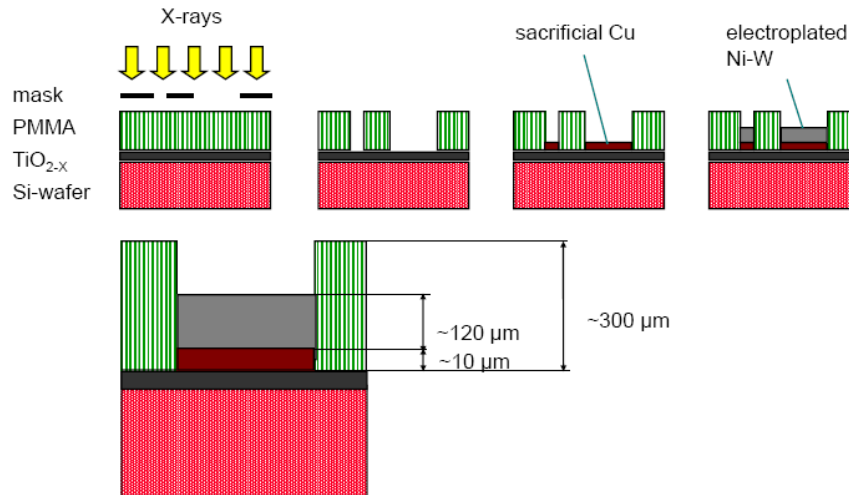
Figure 3.3: LIGA process for the purpose to fabricate metallic electrodeposited microparts
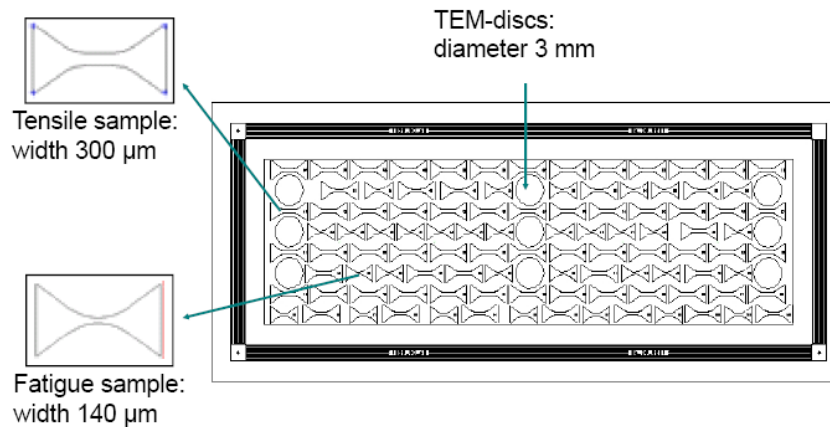
Figure 3.4: Wafer layout showing the different samples resulting from the electrodeposition illustrated in Figure 3.3.

to enhance the surface characteristics (shiny, smooth) of the electrodeposit. After electrodepositing the required microspecimens, the latter have to be released. In a first step the remaining resist is removed by a flood exposure and development. The result is demonstrated for example in the SEM micrograph in Figure 4.3. In a second step, the sacrificial layer is etched using the ammoniacal etching solution and nitric acid in the case of Ni 5 at% W microspecimens as well as Ni-Al$_2$O$_3$ ones and Ni 15 at% W microspecimens, respectively.

3.2 Microstructure investigations

3.2.1 Optical microscope

Two optical microscopes Leica Ergolux 200 and Leica DMLM were available for this work. They are supported by software for image processing. Among others, some important tasks in relation to this work include:

- imaging defects (e.g. pits, cracks) in the range of tens of microns at the surface of the electrodeposited samples

- controlling the surface quality of the ground and polished cross sections

- measuring heights of structure, for instance difference between the electroplated material and the substrate, in order to determine the thickness distribution on the wafer

The accuracy of the optical microscope is estimated to be around 0.5 μm.

However, the use of the optical microscope for these studies is limited and cannot achieve any deeper microstructural investigations. This is due to the low magnification reached by the optical microscope and the small size (in the nm-range) of the grains in the electrodeposited material expected to show nanocrystalline structure.

3.2.2 Scanning Electron Microscope and Energy-Dispersive X-ray spectroscopy

Scanning Electron Microscope (SEM)

The Scanning Electron Microscope (SEM) allows for the observation and characterization of different materials from the micrometer down to the nanometer scale resulting in three-dimensional-like images of the surfaces. This property makes SEM method attractive for characterizing the electrodeposited samples. Two SEMs were used:

- an ESEM 30 XL microscope fabricated by Philips. The resolution reached by this device is about 3 nm depending on the material to be investigated and the scanning parameters (energy, beam size).

- a JSM-6600 microscope fabricated by Jeol. Its resolution reaches approximately 10 nm.

The use of an SEM enables the investigations of the sample surfaces, realized within this study, in order to identify features with the size of several micrometers or even smaller (some hundreds of nanometers) such as pores and co-deposited phases (Al_2O_3 -, Al-particles). The Jeol SEM shows one more facility: introducing the whole wafer into the SEM, which permits the characterization of the whole pattern and not only single specimen.

Despite the relatively higher magnification, the microscope technique mentioned above cannot lead to a successful characterization of the microstructure since the investigated materials are expected to show a grain size in the nm range, presenting the capability limits of this apparatus, and in some cases interacts with the electron beam (e.g surface charging caused by the ceramic particles) hindering consequently the use of SEM at its limits. Within this work, this technique is used to characterize some features that cannot be detected by the optical microscope.

Energy Dispersive X-ray spectroscopy (EDX)

Generally the modern SEMs permit the possibility of Energy-Dispersive X-ray spectroscopy analysis (EDX), which is used to determine the chemical composition of a material. This method is based on measuring and analyzing the energy and intensity distribution of the X-rays emitted by the material hit with the electron beam. These X-rays are characteristic

of an element's atomic structure. The error in the measurements is estimated to the values in Table 3.1 depending on the content of the element detected by EDX [87]. This error can

Table 3.1: the relative error in EDX measurements

Element content in the sample [%]	Relative error [%]
10 - 100	1 - 5
1 - 10	3 -20
0.1 - 1	> 10

be due to different causes. Some of them are given in the following:

- Sample features: the surface smoothness resulted after polishing, non-conductive particles comprised in the investigated material which enhance the electric charging of the surface

- Measurements parameters: counting time and rate, electrons accelerating voltage, angle tilt of the sample, etc. Those parameters have to be optimized in order to obtain valid analysis

The chemical composition of the material deposited within this study is determined using a liquid nitrogen cooled detector mounted in the ESEM 30 XL microscope mentioned in the paragraph above. The voltage applied to accelerate the electrons in the column beam for the use of EDX measurements is 25 kV. Two types of measurements (see Figure 3.5) are realized:

- Area measurements: the scanned area is about 100 μm^2. Three to five areas dispersed along the flat-polished cross sections are scanned and the obtained compositions are averaged to deliver information about the deposited material.

- Point measurements: the scanning occurs on a selected point as indicated in Figure 3.5. The goal of these measurements is to give an overview about the composition distribution along the thickness of the specimen.

By means of EDX, only the percentage of single element in weight-% (wt%) or atom-% (at%) can be given. In order to get the content in a defined phase, further calculations are needed. In the case of Ni-Al$_2$O$_3$, the oxide weight percentage $\chi(Al_2O_3)$ is determined
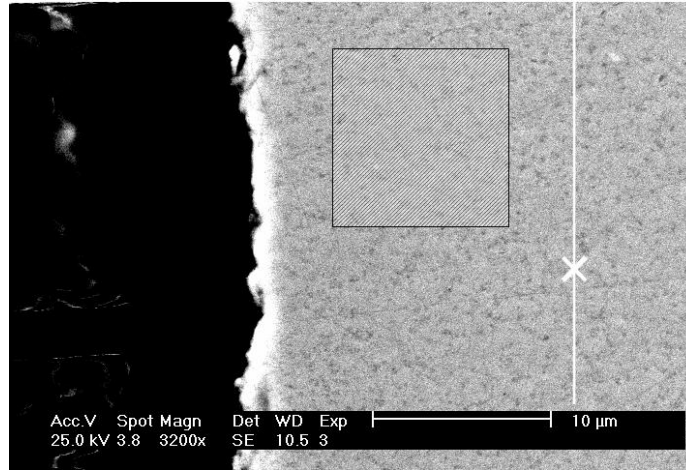
Figure 3.5: SEM picture showing an area of 100 μm^2 and a selected point where the material composition has to be determined using EDX

in Equation 3.3, knowing that $\chi(Al_2O_3) = \chi(Al) + \chi(O)$. $\chi(Al)$, standing for the weight percentage of aluminum, is obtained from the spectrum analysis delivered by the equipment software after the measurement, while $\chi(O)$, the weight percentage of oxygen, is determined using the stoichiometry of the anion-cation ratio of the oxide $\frac{\chi(O)}{\chi(Al)} = \frac{3}{2} \cdot \frac{M(O)}{M(Al)}$. $M(O)$ and $M(Al)$ represent the molar mass of oxygen and aluminum, respectively.

$$\chi(Al_2O_3) = \chi(Al) + \frac{3}{2} \cdot \frac{M(O)}{M(Al)} \cdot \chi(Al) \tag{3.3}$$

The volumetric content of the oxide is also relevant for the study of the Ni-Al$_2$O$_3$ nanocomposites and is given based on the data of the EDX by the following equation:

$$\chi_v(Al_2O_3) = \frac{1}{1 + \frac{\chi(Ni)}{\chi(Al_2O_3)} \cdot \frac{\rho(Al_2O_3)}{\rho(Ni)}} \cdot 100 \tag{3.4}$$

Determining the chemical composition by EDX represents an easy way to obtain relevant information about the deposited material serving as a relevant criterion for optimizing the electrodeposition parameters.

3.2.3 Transmission Electron Microscope (TEM)

Transmission Electron Microscopy (TEM) is one of today's premier tools for microstructural characterization of materials due to its diverse investigation techniques and its high resolution that allows the imaging of objects of a few Angstrom (10^{-10} m). This microscopy technique is based on transmitting electrons with a high energy (> 100 keV) through a thin sample (d < 0.1 μm). The electrons crossing the layer interact with the investigated material. The image is obtained from the transmitted electrons magnified and focused by an objective lens and is displayed on a monitor or detected by a sensor of a CCD Camera.

The TEM investigations in this thesis are performed by Dr. S.J. Suresha (Johns Hopkins University) using Philips 420 TEM operating at 120 keV and Philips CM 300 field-emission gun operating at 300 keV both equipped with X-ray detectors. The investigated samples are disk shaped showing a diameter of 3 mm. The electrodeposited TEM-disks are 150 μm thick depending on the electrodeposition parameters, which is not electron transparent to be used for TEM - investigations. Specimens for TEM observation were prepared using a two-step process. First, twin-jet electropolishing was performed at a potential of 20 V in a 2:1 (v:v) solution of methanol and nitric acid at -40 ^{o}C to perforate the specimens. Final thinning was then conducted by ion milling at 4 kV and 5 mA, at a milling angle of 12 ^{o}.

The TEM-investigations enable the quantification of the material microstructure expected to be nanocrystalline. Mean grain sizes were calculated using equivalent circle diameters from the direct grain area measurements. This was accomplished in a multi-step process since direct image processing of TEM images of nanocrystalline material, that include many overlapping grains with poorly defined grain boundary contrast, was not possible. First, bright and dark field images were taken of the microstructure. Subsequently, traces of single grains, that are either in an orientation that gives rise to strong Bragg diffraction or that show well-defined boundary contrast, were made. Keeping careful track of the scales, these images were digitally processed using Image-Pro Plus software (MediaCybernetics) to segment the area within the traces that resulted in complete geometrical description of the grain shape in 2D (e.g. area, aspect ratio, major axis length, minor axis length, etc.).

In addition, new phases (Al_2O_3-, Al-particles) and lattice defects (distortions through dislocations, twins) are detected and localized. The local chemical composition on precise

areas of the electrodeposited material is determined by the EDX equipment of TEM as well, in order to know about composition distribution within the grains.

3.2.4 X-Ray Diffraction (XRD)

X-Rays are diffracted by crystalline matter. The intensity distribution over the range of diffraction directions is been plotted in a graph called a diffractogram. It usually shows several intensity maxima called "peaks" or "reflections" that come with a Gaussian like shape. Analysis of the position, width and relative intensities of one or an ensemble of XRD peaks yields information on several of the materials' structural features. Speaking in terms of a "reflection", it is due to the explanation model by Bragg demonstrating how XRD diffraction would be maintained within a material. The effect of diffraction is actually the superposition of scattering and interference, thus the effect of vanishing or amplified scattered intensities in respective directions can be explained in terms of optical path differences. This effect is governed by Bragg's Equation [88]:

$$n\lambda = 2d\sin\Theta \tag{3.5}$$

where n is the order of reflection, λ is the wavelength, d is the distance between reflecting lattice planes, Θ is the angle between the incident ray and the reflecting planes.

In this work a Philips X'pert scanning diffractometer, with Ni-filtered Cu-Kα radiation at a wavelength of 1.54187 A^o, has been used in backreflection geometry and $\Theta - \Theta$ scanning Mode. The machine is equipped with a silicon solid detector (X' Celerator detector). For the current measurements, the diffraction angle (=2 Θ) ranges from $38^o \leq 2\Theta \leq 160^o$ and scanning is at angular speed of 0.017 ^{o}/sec. The estimation of the grain size of the electrodeposited materials is one issue; another is phase identification for nanocomposite material. The latter task is accomplished due to the fact that each phase shows a characteristic XRD-diffractogram. The ICDD PDF2/PDF4 databases provide collected diffractograms of diverse materials. An unknown phase with measured diffractogram can be identified if a match of the diffractogram is found in the database.

Estimation of the grain size using XRD

Smaller sizes of diffracting crystallites yield broader diffraction peaks [89]. Thus, the size of crystalline particles can be calculated from the width of XRD peaks if other sources

of broadening can be separated. The sources of the additional broadening include instrumental broadening such as non-ideal optics or wavelength dispersion and microstrain broadening caused, for example, by plastic deformation or point defects. Among the used methods of analysis, Simplified Integral Breadth Methods and advanced Fourier methods usually called Warren-Averbach Methods are to be mentioned.

In the current work, the grain size has been evaluated by means of Williamson-Hall
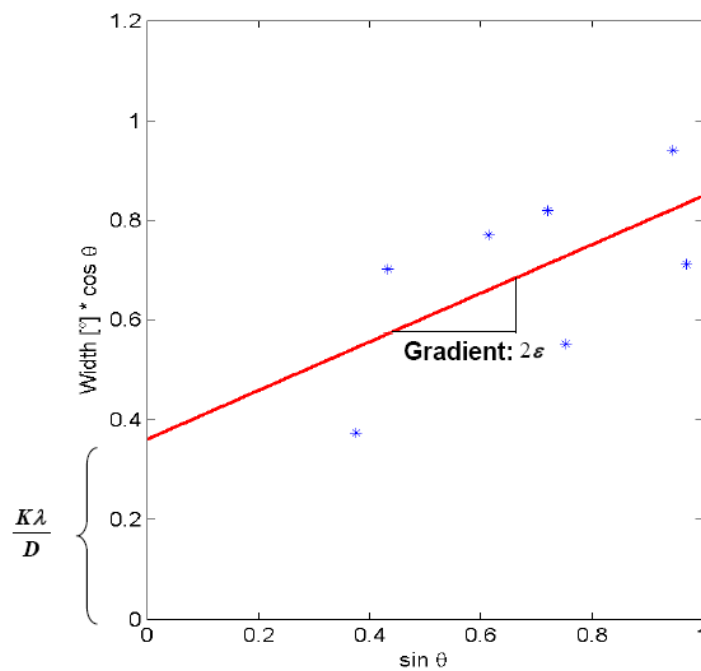
Figure 3.6: Williamson-Hall plot of a Ni 5 at% W sample annealed at 400 ^{o}C for 1h. The individual points represent the experimental peak broadening exluding the instrumental broadening. The line is the linear regression of the experimental data points.

plots [90], which represents an integral breadth method. Assuming that the crystallite size broadening and the strain broadening are additive, which means:

$$\beta = \beta_D + \beta_\varepsilon \qquad (3.6)$$

where:

- the crystallite size broadening $\beta_D = K \frac{\lambda}{D \cos \Theta}$, where K is the Scherrer constant varying between 0.87 and 1, λ is the wavelength of the radiation, D is the crystallite size and Θ is the angle associated to the peak broadening

- the strain broadening $\beta_\varepsilon = 2 \varepsilon \tan(\Theta)$ where ε is the average strain

the crystallite size is given by the following formula:

$$\beta \cos \Theta = \frac{K\lambda}{D} + 2 \varepsilon \sin \Theta \qquad (3.7)$$

The equation 3.7 is equivalent to a linear function $\beta \cos \Theta = A + B \sin \theta$ that can be plotted from the experimental data (peak broadening excluding the instrumental broadening), see Figure 3.6. The crystallite size is consequently determined from the intersection of the plot at $\Theta = 0$ y-coordinate t of the plot, as demonstrated in the WH-plot in Figure 3.6.

The determination of the mean grain size, expected to be above approximately 150 nm by means of this method, becomes inaccurate since the peak broadening is very small for larger grains and thus results in higher standard deviations from the average broadening and consequently for the average grain size. One additional feature that has to be considered while using this method is that the determined crystallite size corresponds to a measure of the size of coherently diffracting area which is not generally the same as particle size due to the presence of polycrystalline aggregates.

3.2.5 Focused Ion Beam (FIB)

The basics of the Focused Ion Beam (FIB) microscope are similar to the SEM, except the FIB uses an ion beam instead of an electron beam. Secondary electrons are emitted after the interaction of the ions with the sample surface to produce high spatial-resolution images. Ga-ions are most commonly used in the commercially available systems.

This instrument shows many functions depending on the resulting effect after the interaction of the ion beam with the sample surface. Among others, the sputtering action of the ions can be mentioned. The FIB can be used to remove or mill away material. For example, TEM-samples can be prepared thanks to several milling steps realized by the ion beam. The imaging of surfaces is also enabled by the FIB. In fact, the ion-induced scanning imaging delivers stronger channeling contrast than the secondary electrons obtained

using a SEM. One other relevant functionality is ion-beam activated deposition accomplished by introducing organic precursors with metal atoms close to the sample surface where they collide with the Ga-ions and, thus, are deposited onto the sample surface.

Nevertheless, the focused ion beam scanning causes damage at the sample surface. Depending on the material and the temperature, the damage can have the form of grain modification, point defects formation, new phase formation, destruction of surface features, etc.

In this study, a dual beam workstation with FIB (focused ion beam) and SEM fabricated by FEI stands at disposal. Cross sections are realized by performing cuts using the Ga-ions beam that is accelerated by a voltage of 30 kV and at a beam current varying between 0.3 nA and 0.5 nA. In order to characterize the microstructure of the deposited material, the imaging of the sample surface is accomplished either using the ion beam at lower ion current (10 pA ... 50 pA) or by means of the electron beam accelerated with a voltage of 10 kV. This electron beam offers the possibility of high resolution imaging through reducing the beam size down to less than 1 nm and thus can be called HR-SEM standing for High Resolution Scanning Electron Microscope.

The use of this device for the characterization of the alloys and nanocomposites developed in this project is limited since formation of Ga containing phases (black islands) [91], [92] as well as ion-beam induced grain growth occur after interaction of the Ga-ions with the nickel atoms (see Figure 3.7).

3.3 Mechanical testing

3.3.1 Microhardness

The resistance of a material with respect to permanent deformation is characterized by its hardness. It relates to the strength of the material [93]. The microhardness can be measured by the use of different scales (Brinell, Vickers, Rockwell). In this work, Vickers microhardness has been measured. The Vickers test uses a square-based diamond pyramid indenter resulting in Vickers hardness values (HV) that are determined from the following equation [93]:

$$HV = 2P\frac{\sin(\Theta/2)}{L^2} = 1.854\frac{P}{L^2} \tag{3.8}$$
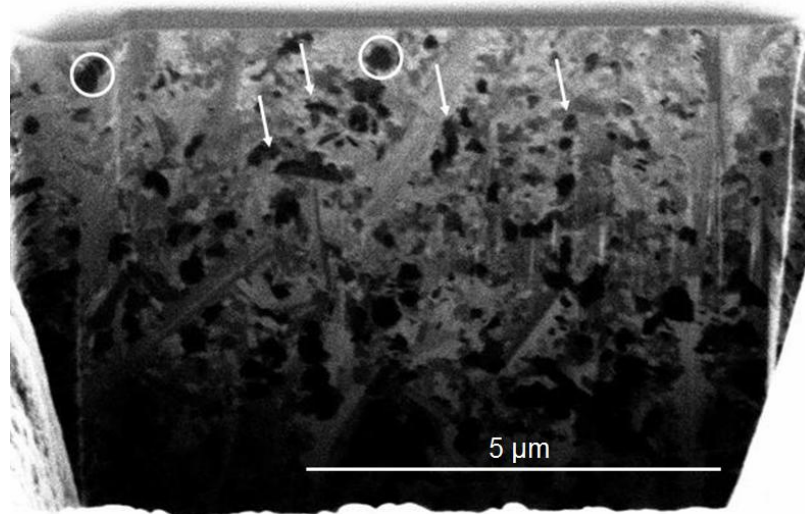
Figure 3.7: FIB-image of Ni-W cut (during imaging ion beam by a voltage of 30 kV and a tilt angle 0°) showing numerous Ga containing phases (black islands) caused by the ion beam. These features are indicated by arrows and circles.

where P presents the applied load given in kg, L is the average length of the diagonals given in mm, measured microscopically on the impression of the indenter (see Figure 3.8) and Θ is the angle between opposite faces of diamond $= 136\,^o$.

The microhardness measurements in these studies are carried out with a Leitz miniload 2 machine. A load of 50 g was applied for 30 s on the surface of the material to be investigated. The preparation of the cross-sections consists of embedding the sample in an embedding medium, which is a mixture of aluminum oxide powder, epoxy resin (Araldit) and hardener, and grinding and polishing its surface to get a scratch-free, smooth surface. On each sample, five to seven indentations are realized, depending on the distribution of the microhardness values.

Since the measurements are realized through human observations of the indentation diagonals, it is important to mention the possible error resulting for the HV values. Based on the equation 3.8, the relative error is calculated as follows:

$$\frac{\Delta(HV)}{HV} = \frac{\partial(HV)}{\partial L}\frac{\Delta L}{L} = -2\frac{\Delta L}{L} \tag{3.9}$$

In this work, the error given with the diagonal length determined by human eye is estimated to be $\pm$ 0.5 μm. This leads to a HV error of $\leq$ 8 % knowing that the smallest diagonal length measured in this study is 12 μm.
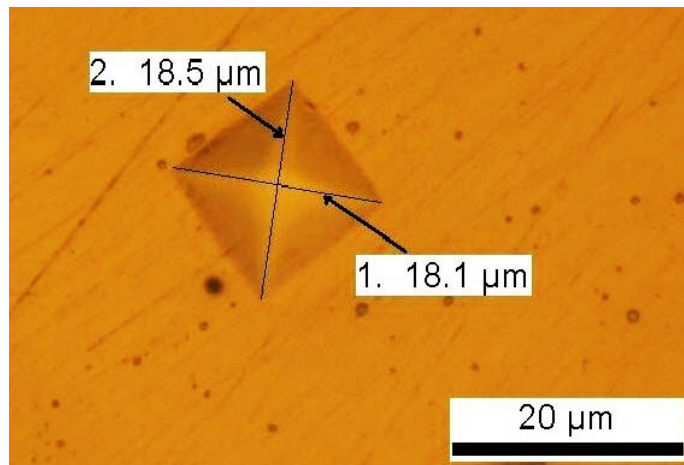
Figure 3.8: Microhardness indentation on the cross section of a Ni-W sample

3.3.2 Microtensile testing

The tensile test is used to provide basic information about the strength of materials. In this type of test, a continually increasing uniaxial tensile load is exerted on a specimen while elongations are simultaneously observed. As a result, a stress-strain curve is obtained that yields relevant mechanical properties. In this curve, engineering stress, obtained from dividing the tensile internal force of a deformed specimen by its original cross-sectional area, is plotted in dependence on the engineering strain which represents the relative displacement between tow particles in the tested material (see Figure 3.9). The tensile strength and yield strength represent strength parameters. Elongation to fracture and elongation area indicate the ductility of the material tested. The stress-strain relation depends especially on the composition and the fabrication process and the heat treatment of the material, the strain rate and the temperature during the test.

In this work, tensile tests are conducted by Dr. S.J. Suresha (Johns Hopkins University) at room temperature for samples in the as-deposited and annealed state. The set-up and the strain measurement method used in these experiments are illustrated in the following paragraphs.

Set-up

The tensile testing set-up, first introduced by Zupan ([94], [72]), is shown in Figure 3.10. Tensile loading, which varies between 0 N and 113.4 N, is accomplished through the
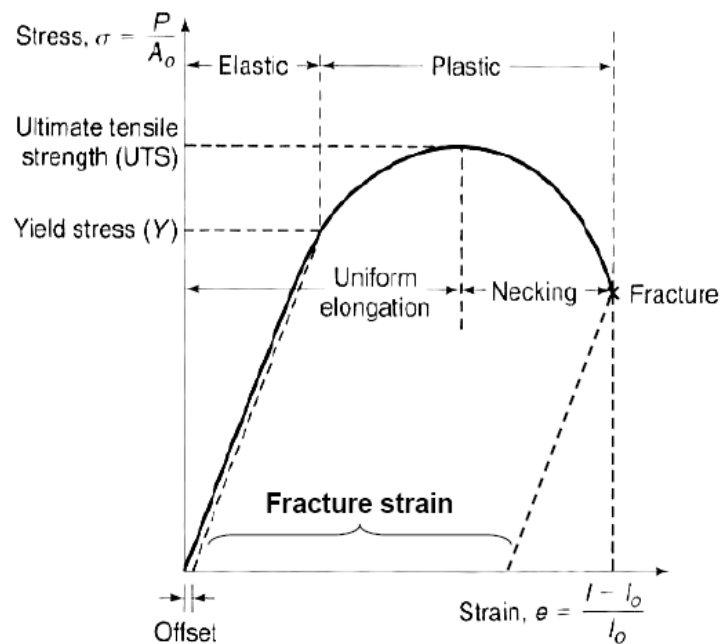
Figure 3.9: Basics of a tensile test

use of a piezo-electric actuator. The tensile test is conducted at a nominal strain rate of $2 \cdot 10^{-4}$ s^{-1} given by the displacement of the actuator.

Sample geometry

The microsamples electrodeposited by the microfabrication process explained in Section 3.1 are dog-bone shaped (see Figure 3.11). They have a thickness in the range of 120 to 200 μm depending on the electrodeposition parameters and the position of the sample on the wafer. This thickness must be machined down to a lower value so that it stays in the range of the measurable stress given by the load cell and the actuator. The tensile specimens show also a curvature between the ear and the gage section given by the function presented in Figure 3.12. For further details see [95].

In contrast to radius or straight angle, the curvature minimizes the stress concentration at this location, and as a result the sample fails especially within the gauge length or at the ear.
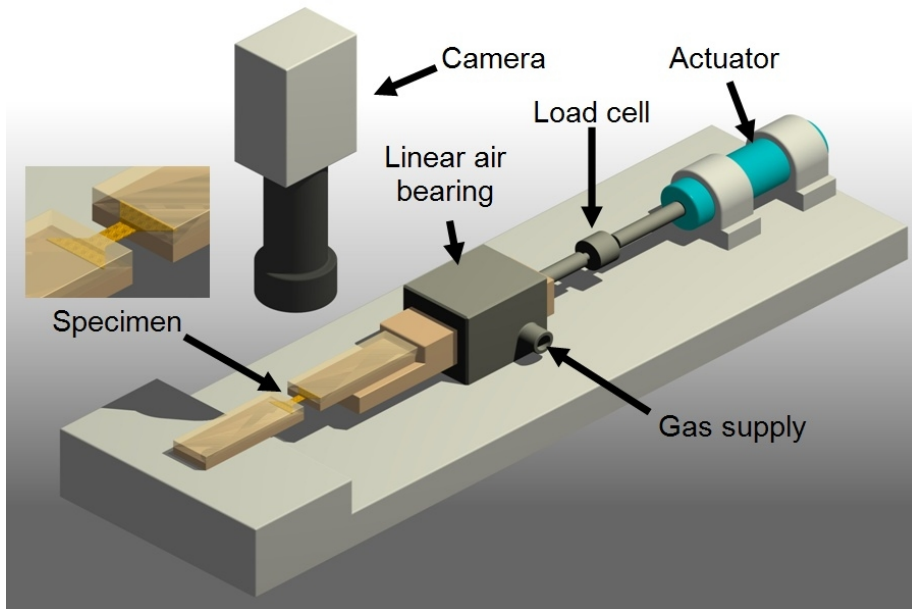
Figure 3.10: Microtensile set-up developed in JHU [94]
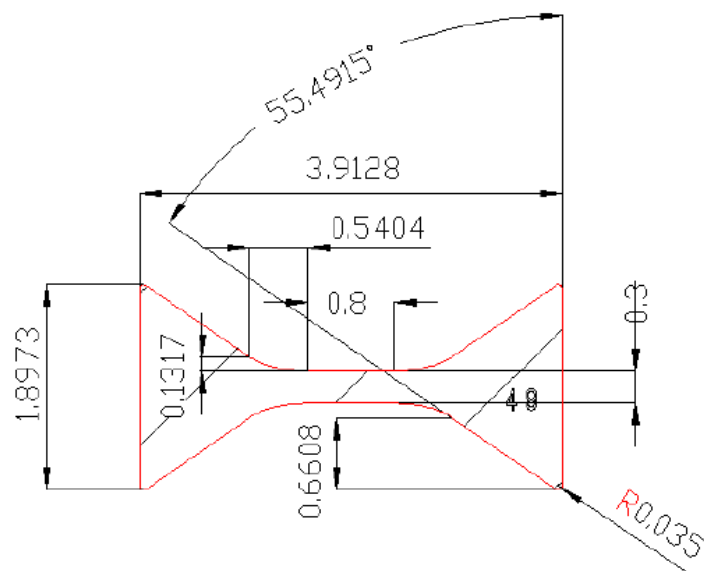
Figure 3.11: Tensile specimen geometry

$$\alpha_{i+1} = 2 \arcsin\left(\frac{D_{i+1} \cos\left(\sum_{k=0}^{i-1} \alpha_k\right)\left(1 + 2\sin\left(\frac{1}{2}\alpha_i\right)\right)}{D_i} - \frac{1}{2} \right)$$

$$D_{i+1} = D_i + 2\,S \sin\left(\sum_{k=0}^{i} \alpha_k\right)$$
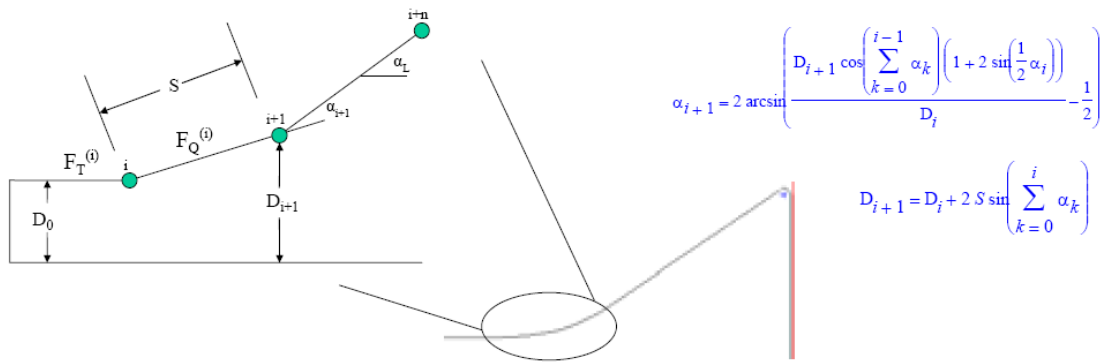
Figure 3.12: The function describing the curvature at the transition from the gage section to the ear of the tensile specimen shown in Figure 3.11.

Strain measurement

In order to measure the strain at micrometer sized samples, a non contact method based on Digital Image Correlation is used in this study. The pictures needed for this method are taken by means of a digital camera (Pixelink, PL-782A) and an objective (Edmund Optics, magnification 2:1). The strain values are then calculated, based on the made pictures, by a software suite using the mathematical package MATLAB [96].

This optical method employing tracking and image registration techniques is based on the maximization of a correlation coefficient that is determined by examining pixel intensity array subsets on two or more corresponding images and extracting the deformation mapping function that relates the images, see Figure 3.13.
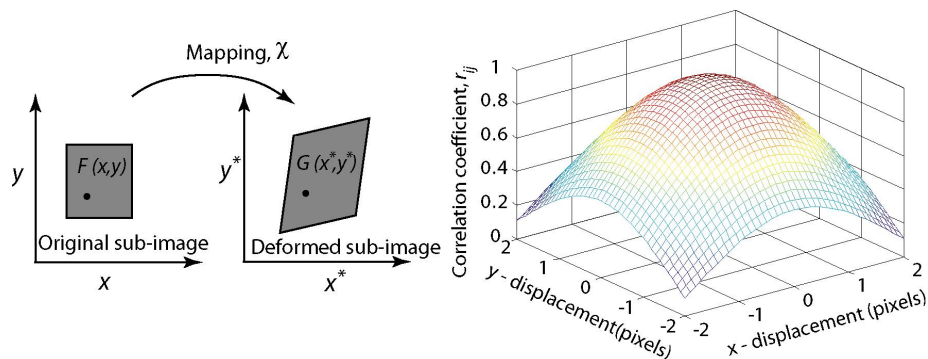
Figure 3.13: Basics of Digital Image Correlation [96]

The needed contrast to correlate images well is provided either by specular markers (powder, paint) or the surface finishes from machining and polishing.

4 Results

4.1 Ni-W alloy

4.1.1 Optimization of the electrodeposition process

Reliable statements about mechanical behaviour of a material, for the use in a determined application, requires the electrodeposition of microspecimens with dimensions comparable to those of the real microparts and showing less defects. For this purpose, the electrodeposition process was optimized within this work and the observed features are presented in the following paragraphs.

Electrolyte chemistry

An ammonia-citrate electrolyte was used in order to electrodeposit Ni-W as mentioned in previous works ([97], [98], [99]). The chemical composition of the electrolyte and the parameters of the electrodeposition are taken from studies summarized in [97], who investigated this electrolyte for the use of electrodepositing Ni-W with different compositions. Two electrolyte compositions for low (5 at%) W and high (15 at%) W are given in Table 4.1. Nickel sulfate and sodium tungstate serve as the origin of the relevant species in the solution responsible for electrodepositing Ni-W. Citric anions and ammonium ions serve as ligands; whereas, sodium bromide is used in order to increase the conductivity of the solution. The tetraethylammonium perfluoro octanesulfonate based commercial surfactant (FT 248) is added since this reduces the formation of pits. The tungsten content in the electrodeposited alloy is controlled by the concentration of nickel sulfate and sodium tungstate. In fact, the electrolyte showing the highest nickel sulfate concentration results in 5 at% W, whereas the one containing lower nickel concentration leads to the electrodeposition of Ni-W with 15 at% W. The pH value, governing the species formed in the electrolyte and their concentration, is determined by means of calculations using Chess software [100]. The

Table 4.1: Chemical composition of the electrolyte used for the electrodeposition of Ni-W alloy with low W content and the one with high W content.

Component	c/W high [g/l]	c/W low [g/l]
Nickel sulfate · 6 H_2O	15.77	61.79
Sodium citrate · 2 H_2O	147.05	147.05
Sodium tungstate · 2 H_2O	46.18	20.57
Ammonium chloride	26.75	26.75
Sodium bromide	15.44	15.44
FT 248	0.2	0.2

results of these calculations, established for the electrolyte showing the chemical composition of Ni-W with high W content, see Table 4.1, are presented in Figure 4.1. For these calculations only two major $[Ni(NH_3)_x]$-species are considered, $x = 2$, $x = 6$.
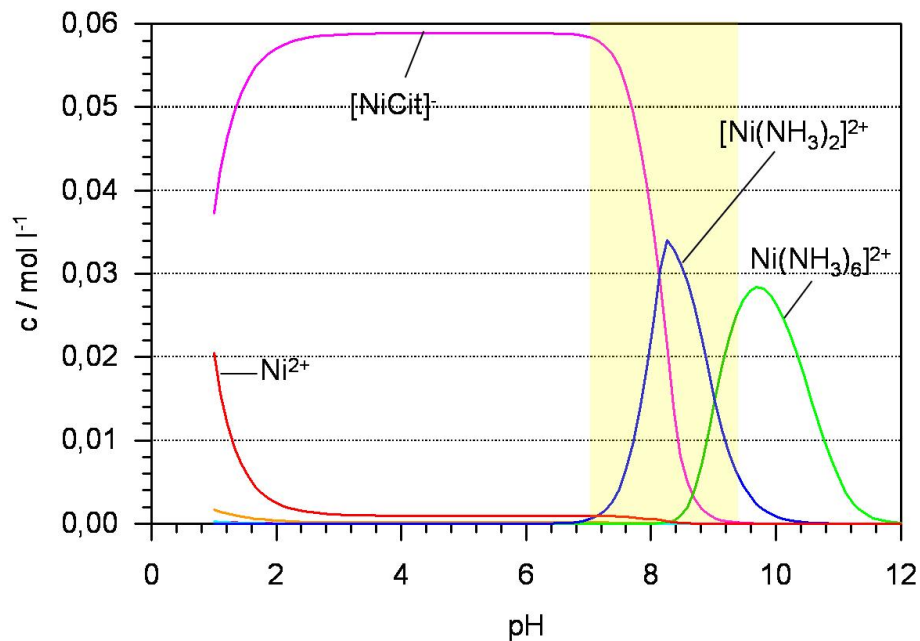
Figure 4.1: Simplified species distribution plot of a Ni-W electrolyte where the initial concentration of nickel is $c^0(Ni^{2+}) = 15.77$ g/L [101].

Each curve corresponds to a species in the electrolyte in thermodynamic equilibrium. The concentration of Ni^{2+} ions starts to decrease at a low pH value (≤ 2) whereas the citrate complex ($[NiCit]^-$) concentration increases to reach a plateau at a pH higher than 2

where the nickel ions are almost completely converted to complexes. When the pH is 7, the concentration of $[NiCit]^-$ decreases till this species disappears at a pH value of circa 9.2, while the formation of nickel ammine complexes $[Ni(NH_3)_2]^{2+}$ and $[Ni(NH_3)_6]^{2+}$ begins. The changes noticed for the species' concentration in the electrolyte are explained by the concentrations' balance stating that the sum of the complexes' concentrations is equal to the initial concentration of nickel ions.

The pH range of 7 to 9 presents the range where the ammine complex $[Ni(NH_3)_2]^{2+}$ reaches its highest concentration range whereas citrate complexes show low concentration. As the electrodeposition of Ni-W is favoured when metallic nickel results from reducing the ammine complexes rather than the citrate ones, the pH controlling the electrodeposition is fixed to 8.5. It is found that in order to reach a layer thickness of about 120 μm, the electrodeposition of the samples with 15 at% W takes 45.5 hours, whereas for the microspecimens with 5 at% W, the electrodeposition needed only 24 hours. The temperature of the solution, which is slowly stirred during the electrodeposition, is adjusted to $75 \pm 5\ ^0$C and the current density to 10 mA / cm^2.

Remarkable features observed within the electrodeposited samples

The samples, fabricated using the electrodeposition process described above, will be examined in this section where some features at the surface and within the cross section of these specimens will be presented. Figure 4.2 displays the W distribution measured for a sample with an average W content of circa 8 at%.

The chemical composition of the material resulting from the electrolyte given in Table 4.1 was determined by EDX measurements at the surface and on the cross section of the samples. It has been shown that Ni-W with an average W content of 5 at% and 15 at% was obtained from the electrolyte c/W low and c/W high in Table 4.1, respectively. The composition distribution along the growth direction is also studied for several electrodeposited samples. The W content is plotted in dependence on the position of the analyzed points. The points selected for the composition measurements are located on the cross section of a Ni-W layer with a thickness of circa 200 μm and aligned showing spacing of 10 μm each. It is important to note that the average of the W content along the cross section of the layer is estimated to be around 8 at%. The deviation range of the measurements is shown to be 1.5 at% W which represents at several points the deviation range of the values measured
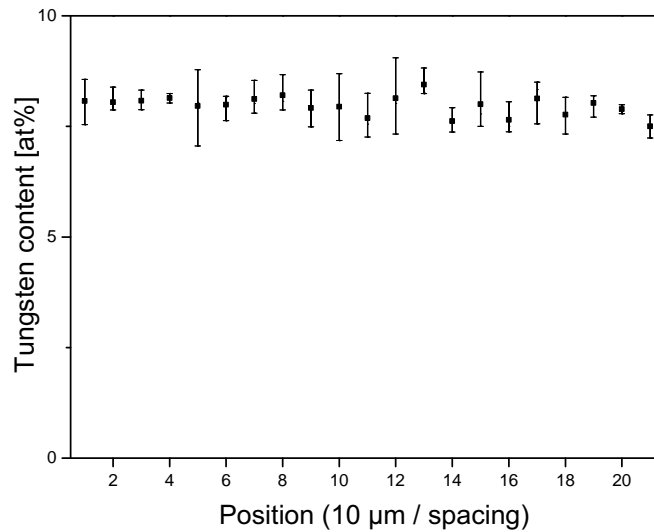
Figure 4.2: Chemical composition distribution along the cross section of a Ni-W layer containing an average W content of 8 at%. The first measurement corresponds to the closest point to the substrate.

at one position. A comparable trend with that in Figure 4.2 was also observed while measuring the composition distribution along the cross section of samples containing 5 and 15 at% W.

The micrographs in Figure 4.3 and 4.4 show two tensile microspecimens with different compositions.

The microspecimen with low W content presents a rough surface with dispersed cusps. This effect is partly due to the higher thickness of the microsample in 4.4 compared to the specimen containing 15 at% W, which shows a smoother surface. On the latter specimen, isolated pits are still visible despite the addition of the surfactant FT 248. After analyzing selected specimens, getting an overview on all the specimens on the wafer is also relevant, since LIGA is thought to be a microfabrication process delivering higher numbers of microparts.

The thickness of the electrodeposited material is plotted against the specimen number which gives information about the position on the wafer, for Ni 15 at% W and Ni 5 at% W in Figure 4.5 and 4.6, respectively. The plotted values correspond to the entire thickness of the electrodeposited microspecimens before releasing them from the wafer. This includes
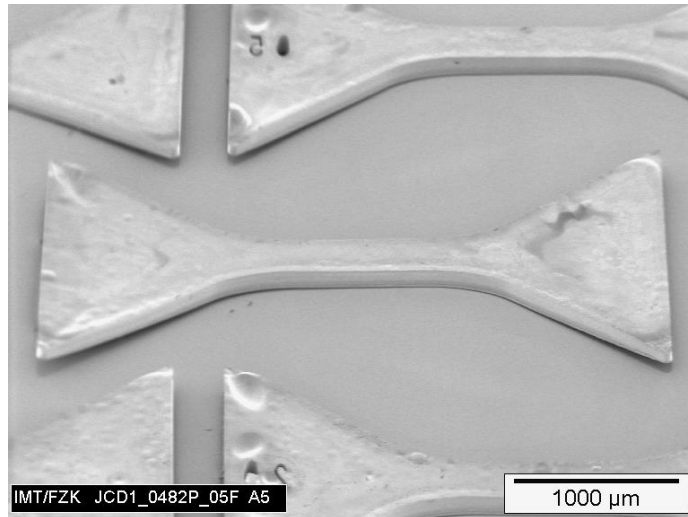
Figure 4.3: Ni 15 at% W tensile microspecimen after stripping
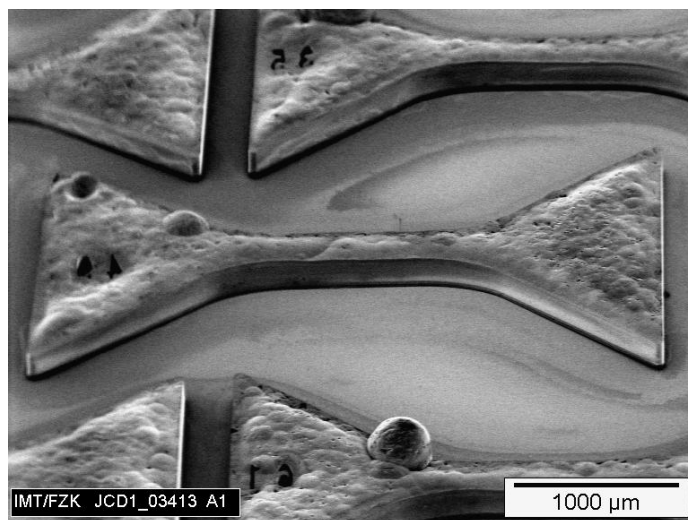
Figure 4.4: Ni 5 at% W tensile microspecimen after stripping

the electrodeposited Ni-W and the sacrificial copper layer showing a thickness of 10 μm.
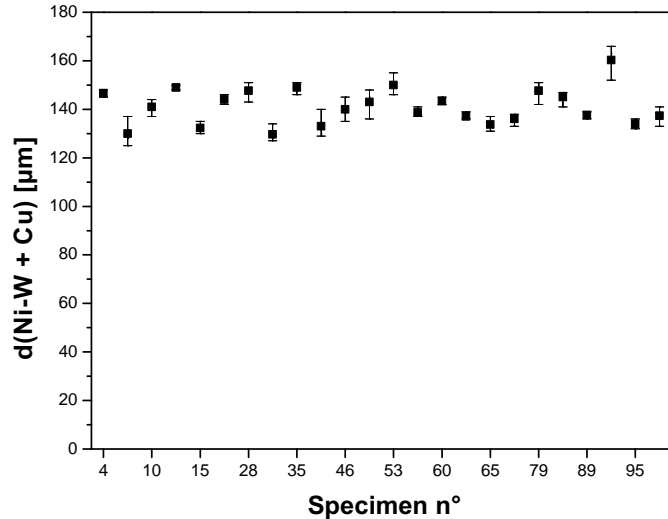
Figure 4.5: Thickness distribution of the electrodeposited material on the wafer surface. The thickness is the sum of Ni 15 at% W and 10 μm thick sacrificial copper layer.

It is worth noting that the thickness of the Ni 15 at% W alloy presented in Figure 4.5 varies around a mean value of 130 μm in a range of circa 30 μm, whereas the thickness of the samples with 5 at% (Figure 4.6) is shown to scatter around an average of 200 μm in a larger range of about 70 μm. The wider dispersion observed for Ni-W with low W content is due to the relatively high obtained thickness.

One more feature observed on the cross section is illustrated in the micrograph 4.7 which presents the lower part of a microspecimen edge. The sample consists of Ti-oxide, sacrificial copper and Ni-W as indicated in Figure 4.7.

A step between Ni-W and copper is identified through the difference in sharpness marked in Figure 4.7. This demonstrates that the dimensions of the specimen vary slightly from those of the copper layer.

The micrograph 4.8 shows an electrodeposited TEM disk. The TEM disk is partly released from the wafer and consequently bent, while the tensile specimens, see Figure 4.3, are more attached to the wafer and show less bending effects since they are released at smaller areas. The release of both samples occurs in the titanium oxide layer. This effect is observed mainly on the TEM disk in Figure 4.8 that shows the larger released area. It
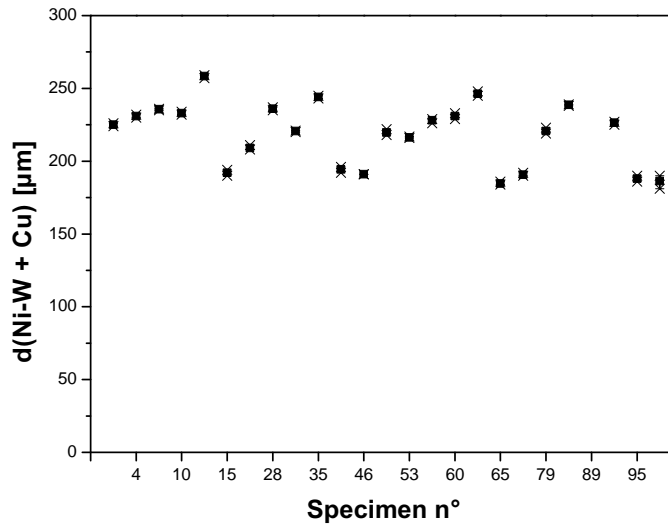
Figure 4.6: Thickness distribution of the electrodeposited material on the wafer surface. The thickness is the sum of Ni 5 at% W and 10 μm thick sacrificial copper layer.
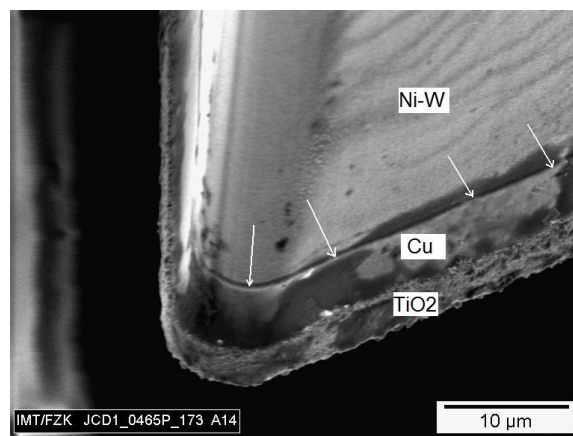
Figure 4.7: Lower part of a microspecimen profile including Ni-W, sacrificial Cu and TiO$_2$. A step between Cu and Ni-W is indicated by arrows.
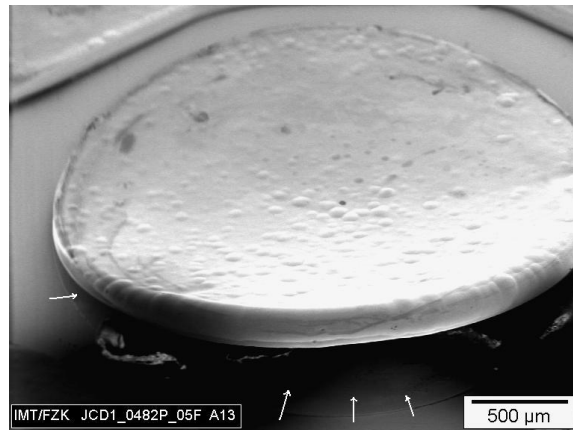
Figure 4.8: Ni 15 at% W TEM disk after stripping. The arrows show the release of the TEM sample in the titinium oxide layer.

is identified through the color difference remarked on the substrate as indicated in Figure 4.8.

The microstrcuture and mechanical properties of several samples studied in this section will be described in the following paragraphs. Those samples are summarized in Table 4.2 with their W content and the experiments they are used in.

4.1.2 Microhardness measurements and microstructure investigations in the as-deposited state and after annealing

Some layers, prepared according to the electrodeposition process described in the last paragraph 4.1.1 and indicated in Table 4.2, are used to determine the microhardness of the material and the respective microstructure in the as-deposited state and after annealing.

In Figure 4.9, the microhardness values of Ni-W layers versus the annealing temperature are shown for different compositions. The behaviour of these alloys is compared to pure nickel electrodeposited from a commercial sulfamate electrolyte, similar to that investigated in [102]. The microhardness values of pure nickel drop strongly after annealing and reach at temperatures $\geq 400\ ^oC$ a domain where the microhardness decreases only weakly. After annealing at higher temperatures ($\geq 500\ ^oC$), the hardness represents only 33% of the initial value (before annealing) as shown in [103]. In contrast, the Ni-W layers show much higher microhardness values in the as-deposited state compared to pure nickel. After annealing, the microhardness values increase slightly at intermediate temperatures

Table 4.2: Electrodeposited samples for the use in microstructural and mechanical characterization

Sample form	W content [at%]	Characterization type
Layer	0	Microhardness (Figure 4.9) and FIB (Figure 4.10)
Layer	13.6	Microhardness (Figure 4.9)
Layer	14	Microhardness (Figure 4.9)
Layer	15	Microhardness (Figure 4.9) and FIB (Figure 4.10)
Dummy areas from a microspecimens batch	15 and 5	Microhardness (Figure 4.11) and grain size by XRD (Figures 4.12 and 4.13)
TEM disks from a microspecimens batch	15 and 5	TEM (Figures 4.14 and 4.15)
Tensile microspecimens	15 and 5	Tensile test (Figures 4.16 and 4.19)
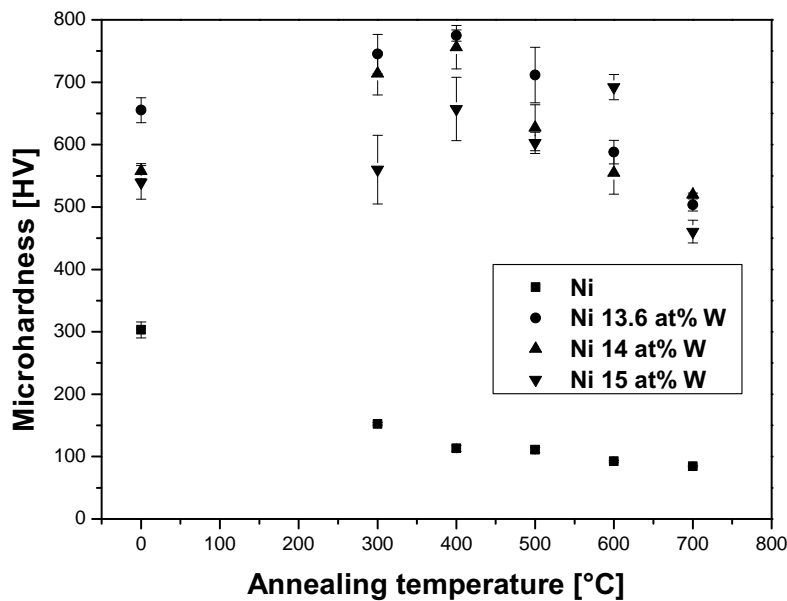
Figure 4.9: Microhardness of LIGA Ni and different LIGA Ni-W alloys and its dependence on the annealing temperature (2h duration).

(300 - 500 ^{o}C) reaching a maximum at 400 ^{o}C and decrease a little at higher annealing temperatures. We notice that the microhardness values of Ni-W layers after annealing are higher than the values of pure nickel even in the as-deposited state.
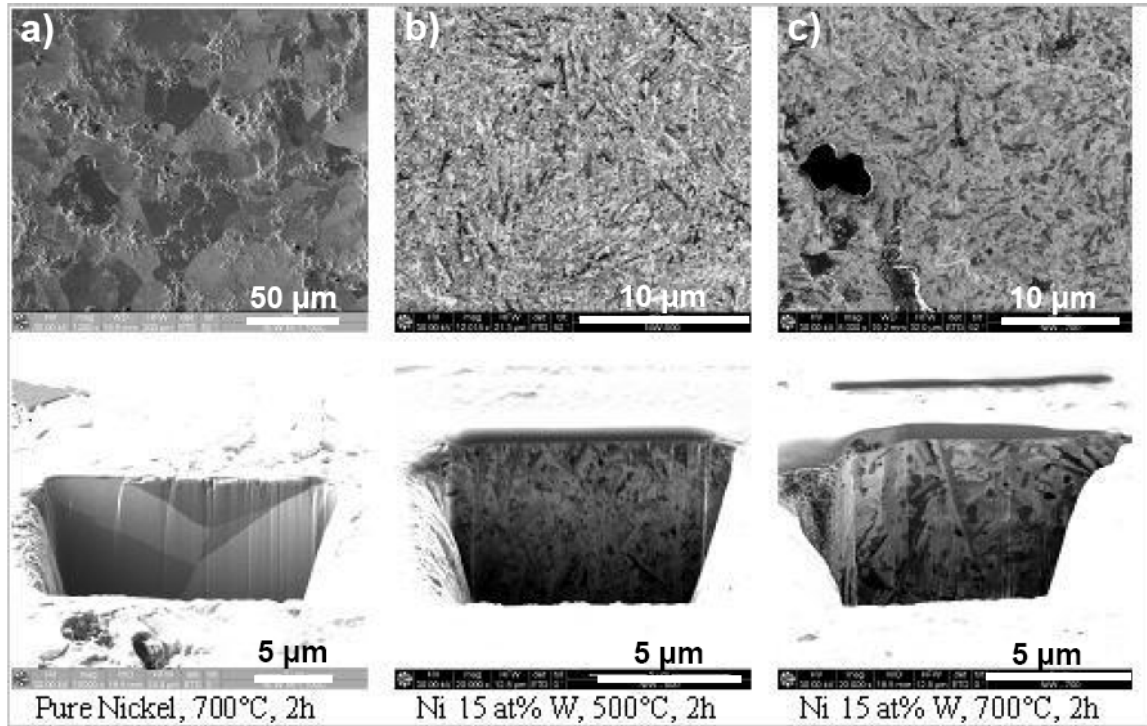
Figure 4.10: Focused ion beam (FIB) microscopy images showing the microstructures of annealed LIGA Ni and LIGA Ni-W after annealing in plan (above) and cross views (below).

The FIB images presented in Figure 4.10 show overviews and cross-views of pure nickel annealed at 700 ^{o}C and Ni 15 at% W annealed at 500 ^{o}C and 700 ^{o}C. In Figure 4.10 a, the remarkable grain growth of the annealed electrodeposited pure nickel compared to the initial grain size at the as-deposited state is seen [104]. However, the Ni-W samples annealed at different temperatures show small grain size in the nm-range even at high annealing temperatures up to 700 ^{o}C (Figure 4.10 b and c). The influence of the W content and the annealing parameters on the microhardness measurements was also studied and is presented in Figure 4.11. The microhardness values of the Ni 15 at% W samples at each annealing temperature show a negligible decrease even with long annealing durations. The Ni 5 at% W samples annealed at 400 ^{o}C feature a quite constant behaviour of the microhardness independent of the annealing duration. At 700 ^{o}C, the microhardness decreases even at shorter annealing times and reaches a plateau at about 50% of the microhardness
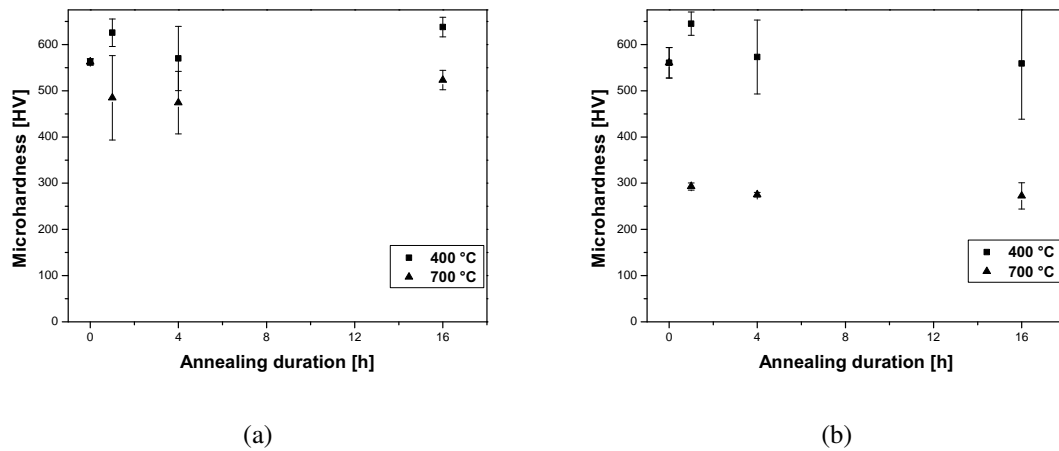
Figure 4.11: Dependence of the microhardness of LIGA Ni-W alloys on the annealing duration, annealed at different temperatures 400 ^{o}C and 700 ^{o}C: a- Ni 15 at% W, b- Ni 5 at% W.

value of the as-deposited samples. However, the microhardness value reached after longer annealing time is still higher than pure nickel in the as-deposited state (see Figure 4.9).

The grain size of the annealed samples from Figure 4.11 is determined by the WH-plot method described in Section 3.2.4 and is plotted in dependence on the annealing duration in Figures 4.12 a and b. At intermediate annealing temperature (400 ^{o}C), the grain size of Ni 15 at% W and Ni 5 at% W remain almost unchanged in comparison to the as-deposited state even at higher annealing duration. However, at higher annealing temperature, the developing of the Ni 15 at% W grain size values demonstrates a small increase in contrast to that of Ni 5 at% W which exceeds the limit of the grain size measurable by XRD. The standard deviations of the samples with lower W content are clearly higher than those of higher W content samples reaching half of the determined grain size after 1 hour annealing.

The grain size obtained by XRD for both alloys is also displayed as a function of the annealing temperature in Figures 4.13 a and b. The effect of the annealing duration on the grain size becomes more considerable at high annealing temperature (700 ^{o}C) especially for the alloy with low W content. Until an annealing temperature of 400 ^{o}C is reached, the grain size remains almost unchanged. At annealing temperatures > 400 ^{o}C, it is worth noting that the grain size increases rapidly. This effect is shown to be in high gear for the alloy with low W content than that with high W content.

(a)   (b)
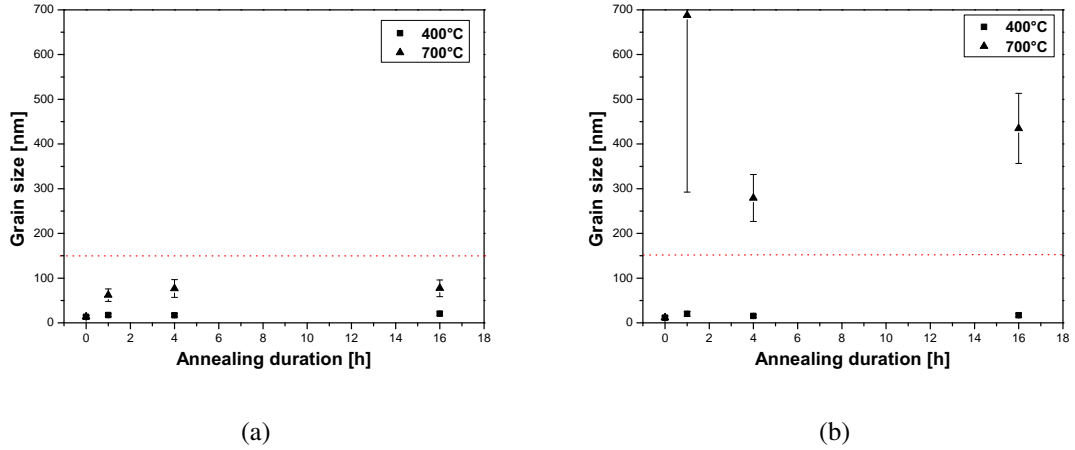
Figure 4.12: Grain size determined by WH method in dependence on the annealing duration at two different annealing temperatures 400 ^oC and 700 ^oC: a- for Ni 15 at% W, b- for Ni 5 at% W. The dashed lines correspond to the upper grain size limit of the size measurable by XRD.

(a)   (b)
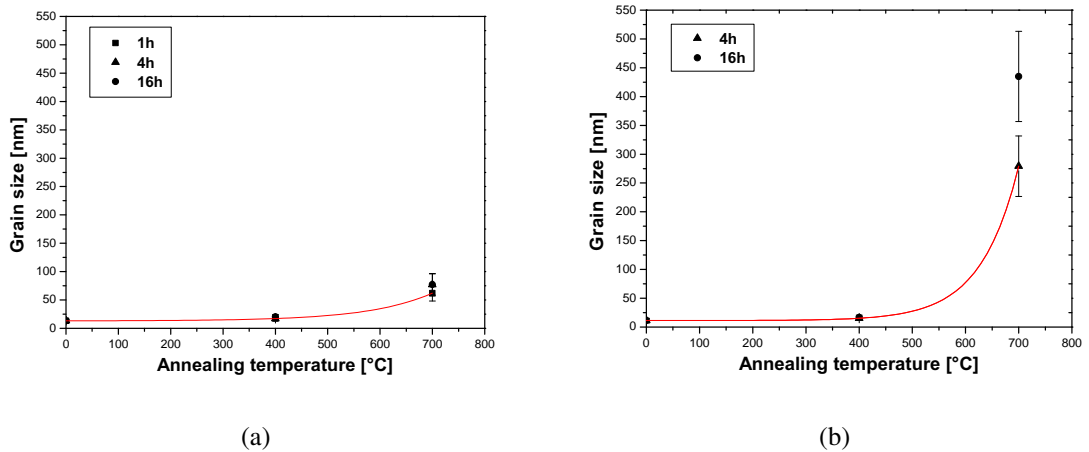
Figure 4.13: Dependence of the grain size determined by XRD on the annealing temperature: a- for Ni 15 at% W annealed at different durations (1h, 4h, 16h), b- for Ni 5 at% W annealed at different durations (4h, 16h).

The microstructure of several samples studied above is also investigated by means of TEM (see Figures 4.14 and 4.15).   The corresponding grain size is determined using
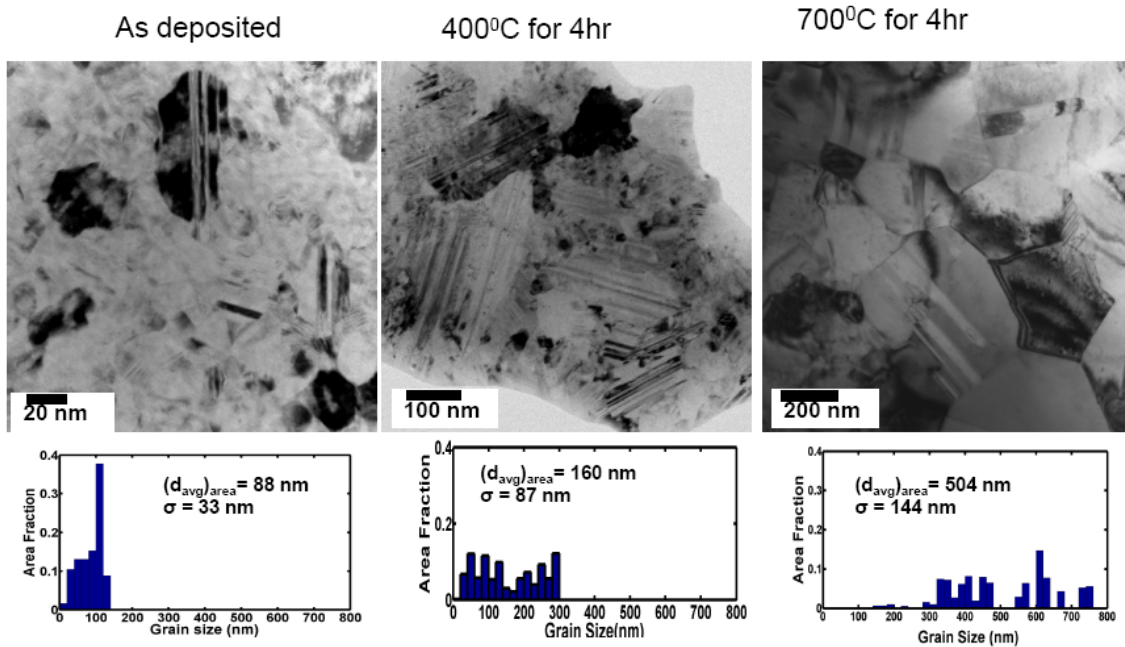
Figure 4.14: TEM micrographs of as-deposited and annealed Ni 15 at% W samples and the corresponding grain size distributions [105].

the strategy mentioned in Section 3.2.3. The observed grains for both alloy compositions show fuzzy boundaries that become clearer at high temperature (700 ^{o}C). Within the grains many defects are detected, for instance twins and dark areas conventionally standing for accumulation of dislocations. The alloy with higher W content in the as-deposited state demonstrates, according to the TEM image and the respective grain size distribution, 40 % of the grains with about 100 nm size and the rest with homogenous distributed sizes ranging between 0 and 100 nm. After annealing, the grain size becomes more uniformly distributed. The grains grow slower at 400 ^{o}C than at 700 ^{o}C where they show two size groups including smaller ones ranging around 400 nm and larger ones with an average grain size of about 600 nm.

The samples with lower W content contain, in the as-deposited state, grains whose sizes vary between 0 and 100 nm. At an annealing temperature of 400 ^{o}C and an annealing duration of one hour, which is lower than the annealing duration set for Ni 15 at% W, the grains show grains in the range between 50 and 350 nm. At higher annealing temperature
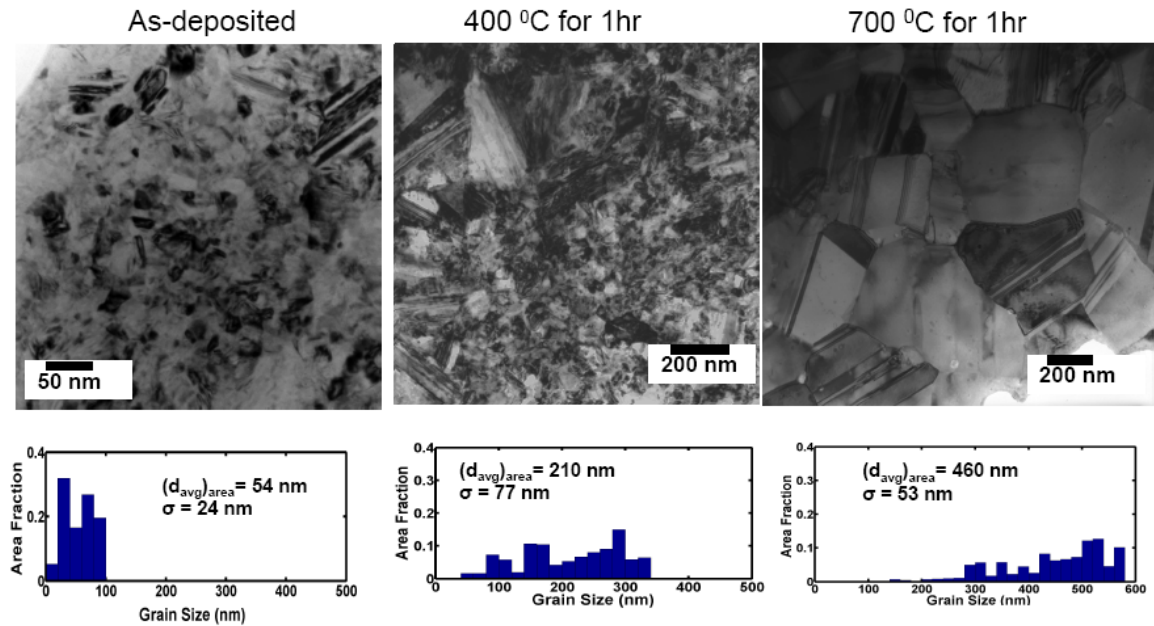
Figure 4.15: TEM micrographs of as-deposited and annealed Ni 5 at% W samples and the corresponding grain size distributions [105].

and the same annealing duration as before, larger grains, whose majority show a size above 400 nm are observed.

4.1.3 Room temperature tensile tests in the as-deposited and annealed state

As-deposited state

Microtensile tests were carried out for selected microspecimens with different compositions in order to better characterize the mechanical behaviour of the electrodeposited material in the as-deposited and annealed state as well. For each composition, several samples coming from the same batch were tested in order to obtain statistical information about mechanical properties of the electrodeposited material.

The room temperature stress-strain curves of Ni 15 at% W and Ni 5 at% W samples are plotted in Figure 4.16a and b, respectively. The mechanical properties determined from these plots are summarized in Table 4.3 which also includes data about electrodeposited pure nickel mentioned in [22]. Young's modulus was determined to 175 ± 12 GPa and
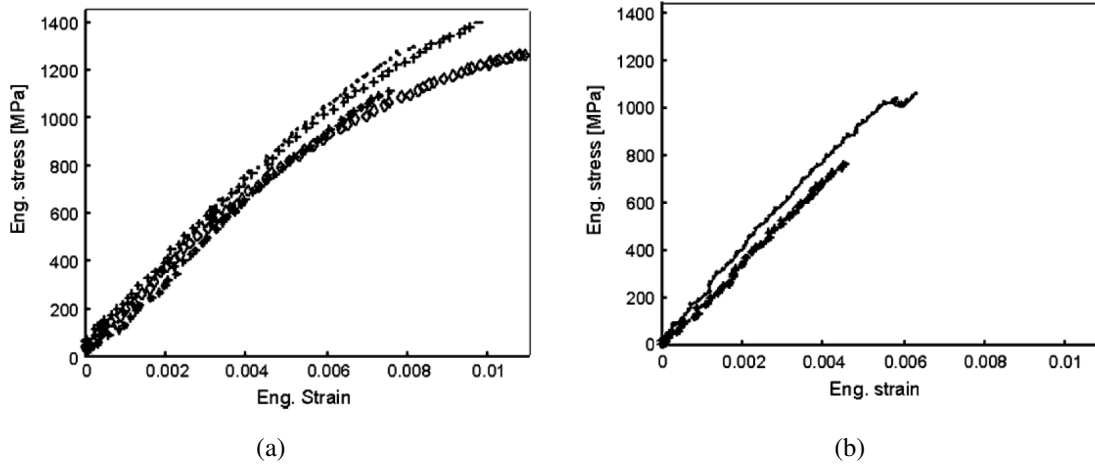
Figure 4.16: Room temperature stress-strain curves obtained by the microsample tensile testing, strain-rate: $2 \cdot 10^{-4} s^{-1}$, a- four samples with Ni 15 at% W composition, b- two samples with Ni 5 at% W composition.

Table 4.3: Mechanical properties of LIGA Ni and LIGA Ni-W at room temperature

	Fracture stress [MPa]	Modulus of elasticity [GPa]	Fracture strain [%]
Ni 15 at% W	1264 ± 119	175 ± 12	0.17 ± 0.12
Ni 5 at% W	912 ± 211	176 ± 2	0.04 ± 0.06
pure nickel [22]	520 (UTS)	163 ± 14	3.35

176 ± 2 GPa for Ni 15 at% W and Ni 5 at% W, respectively, by linear regression of the initial straight part of the curve. For each composition the curves show similar linear elastic behaviour. The average of the fracture stress of each composition is higher than the ultimate tensile strength (UTS) of pure nickel, see Table 4.3. The Young's modulus of the Ni-W samples given in Table 4.3 is almost the same for both compositions and is located in the range of one of the pure nickel as shown in [22]. The tested materials exhibit very low ductility compared to electrodeposited pure nickel, as shown in Table 4.3. The Ni 15 at% W samples show a very low plasticity. They broke after much less than 1% engineering strain. The Ni 5 at% W samples exhibit almost no plasticity. Moreover, they show lower strength than the Ni 15 at% W samples. The roughness of the fracture surfaces of two tested tensile samples with different compositions (Figures 4.17 and 4.18) prove the brittleness of electrodeposited Ni-W alloys. If we compare the fracture surfaces ob-
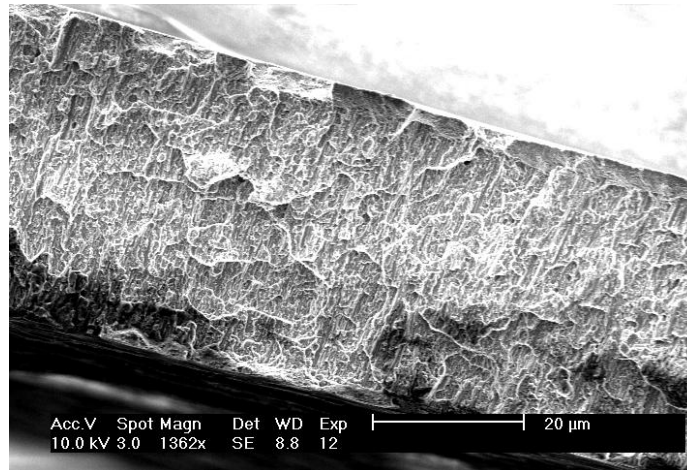
Figure 4.17: SEM-image showing the fracture surface of a LIGA Ni 15 at% W tensile specimen in as-deposited condition.

tained for both samples, we can first conclude that the fracture of the Ni 15 at% W sample looks intergranular where the cracks propagate along grain boundaries (Figure 4.17). The fracture of the Ni 5 at% W sample looks transgranular in which the cracks grows at high speed into the grains and move from a plane level to another when they hit an obstacle (see circular lines in Figure 4.18). As it is well known that electrodeposited Ni-W shows a nanocrystalline microstructure, it is possible also to say that the fracture of the samples with the higher W content is transgranular if the crack growth into the grains occurs in smaller scale than the one demonstrated in the case of Ni-W with low W content.
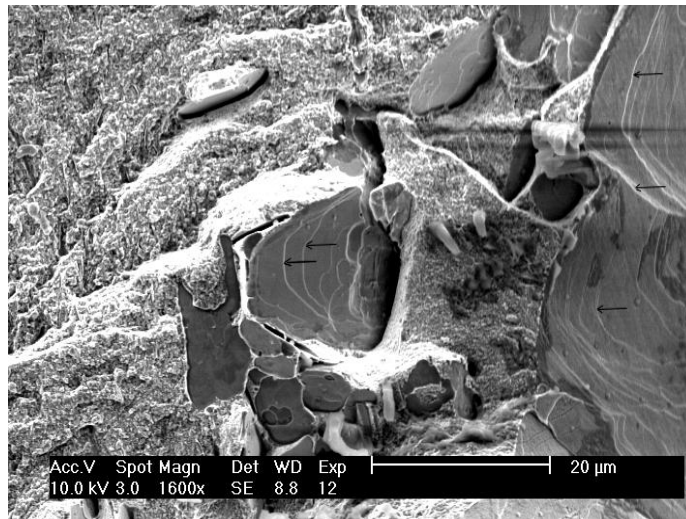
Figure 4.18: SEM-image showing the fracture surface of a LIGA Ni 5 at% W tensile specimen in as-deposited condition. Arrows indicate circular lines caused by the fracture.

Annealed state

The behaviour of several microspecimens from both available compositions and annealed at the same parameters as in Section 4.1.2 are compared to that of the as-deposited samples in 4.19. Some tensile properties, determined from Figure 4.19, are given in Table 4.4. At 400 ^oC annealing temperature and one hour annealing duration, the microspecimen

Table 4.4: Tensile properties of several Ni 15 at% W and Ni 5 at% W samples in the annealed state [105]. The corresponding stress-strain curves are plotted in Figure 4.19.

Annealing temperature [^oC]	Annealing duration [h]	UTS of Ni 15 at% W [MPa]	UTS of Ni 5 at% W [MPa]
400	1	2135 ± 30	1080 ± 14
400	4	2030 ± 20	955 ± 20
700	1	1459 ± 22	746 ± 10
700	4	1515 ± 14	782 ± 21

with low W content shows similar tensile behaviour as in the as-deposited state, while the material with higher W content reaches higher ultimate tensile strength presenting about 2 times the fracture stress of the as-deposited material (1049 ± 40 [MPa]) and an additional low plasticity is to see. The higher annealing temperature 700 ^oC highlights a remarkable
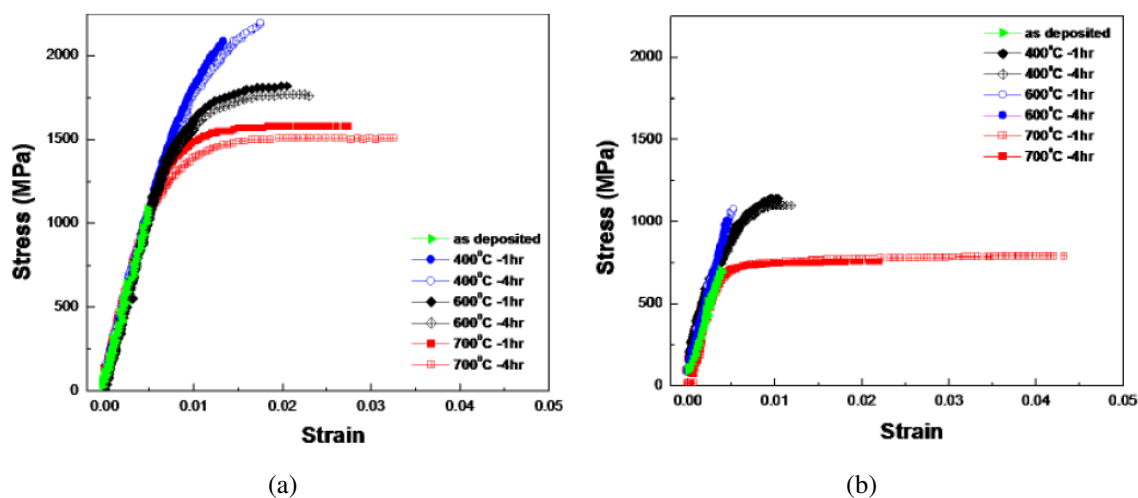
Figure 4.19: Room temperature stress-strain curves of annealed samples in comparison to as-deposited ones [105], a- Ni 15 at% W, b- Ni 5 at% W.

increase in plasticity for all the samples. The UTS of the Ni 15 at% W sample annealed during one hour decreases if compared to the 400 ^{o}C value, remaining higher than the fracture stress (704 $\pm$ 27 [MPa]) und UTS resulting for the samples containing 5 at% W in the as-deposited and annealed state, respectively. The UTS of the latter material demonstrates no change compared to lower annealing temperatures, whereas the plasticity area increases clearly, especially at higher annealing duration. Both alloys, tested above, result in higher strength even at higher annealing temperature and duration compared to pure Nickel in the as-deposited state (see Table 4.3).

4.2 Ni-Al$_2$O$_3$ nanocomposite

4.2.1 Optimization of the electrodeposition process

The co-deposition of alumina nanoparticles with nickel should yield finely dispersed particles in the nickel matrix. Therefore, well dispersed particles are needed in the electrolyte. For this purpose, two dispersions are studied and presented in the following.

Nickel sulfamate electrolyte with hydrophobic particles

The used electrolyte shown in Table 4.5 is a nickel sulfamate electrolyte at a pH of 3.4, which represents the usual electrolyte for the electrodeposition of nickel [102]. Spherical

Table 4.5: Composition of the sulfamate electrolyte containing hydrophobic Al_2O_3 particles

Component	Concentration [g/L]
$Ni(SO_3NH_2)_2$(as nickel sulfamate solution)	76
Boric acid H_3BO_3	40
SDS	12.65
hydrophobic Al_2O_3	30

hydrophobic particles fabricated by Evonik with average nominal diameter of 13 nm were added to the solution. Hydrophobic refers to the tendency of a substance to repel water or to be incapable of mixing with water. The hydrophobic particles carry no charge at their surface. The surfactant sodium lauryl sulfate (SDS) was added progressively till the particles dissolve in the electrolyte and are not anymore to see as separate phase above the solution. The prepared dispersion was treated by ultrasonic for 30 minutes before starting the electrodeposition. During the experiment, the temperature is kept to $50 \pm 5\ ^oC$ and the stirring velocity to 200 rpm. Two current densities, 2 A / dm^2 and 5 A / dm^2, were selected for the electrodeposition. The chemical composition of the electrodeposited layers were determined by local measurements using EDX and global ones using chemical analysis. These methods for determining the chemical composition demonstrated almost no trace of alumina in the electrodeposits. The measured microhardness for both samples showed values varying between 200 and 300 HV which is of the order of pure nickel (see Figure 4.9).

Nickel sulfate electrolyte with hydrophilic particles

Table 4.6 gives the composition of another dispersion studied. Ammonia and citrate were used as ligands in the Ni-W electrolyte discussed above. Sodium citrate is also known to be a dispersing agent assuring the electrostatic stabilization of the ceramic particles in the electrolyte. The latter dispersion strategy is based on the repulsive interaction between the particles after modifying their electrostatic state. The effect of citrate will be studied

Table 4.6: Composition of the sulfate electrolyte containing hydrophilic Al_2O_3 particles

Component	Concentration [mol/L]
Sodium citrate	0.1...0.9
Nickel sulfate	0.06...1.06
Ammonium chloride	0.5...2
Sodium bromide	0.15
FT 248	$2.1 \cdot 10^{-4}$
hydrophilic Al_2O_3	0.294

more closely later. Sodium bromide and the surfactant play the same role here as in the electrolyte used to electroplate Ni-W.

The alumina particles aeroxide ALU 65 delivered by Evonik show a nominal diameter of 17 nm. They are hydrophilic and consequently charged or have polar groups at their surface that attracts water.

The pH of the solution is adjusted to around 8.5 for the purpose of obtaining similar species distribution as demonstrated in Figure 4.1. The temperature during the electrodeposition was kept at 50 ± 5 ^{o}C, which represents the temperature during pure nickel electroplating [102]. During the electrodeposition, the electrolyte was stirred with a stirring velocity of 500 rpm in order to avoid the sedimentation of Al_2O_3 and to homogenize the temperature in the solution.

In the following, several explicit studies related to the hydrophilic particles dispersion are presented. These studies deal with the behaviour of the electrolyte and the electrodeposited material when varying one of the parameters described above.

Effect of sodium citrate on the dispersion characteristics

The citrate concentration varied in the range between 0.1 and 0.9 mol/L, remaining below the solubility limit of sodium citrate in water (425 g/L corresponding to 1.445 mol/L). The effect of this variation is illustrated in Figure 4.20. The plots show the dependence of the measured change in height (ΔH) of the dispersion phase (see cylinder on the left of Figure 4.20) on the age of the electrolyte. Each plot corresponds to a different citrate concentration. Such plots provide the information about the sinking velocity of the particles floating in the solution. We can notice the decrease of the dispersion heights when increasing the age of the solution for all citrate concentrations. In the case of the highest concentration,
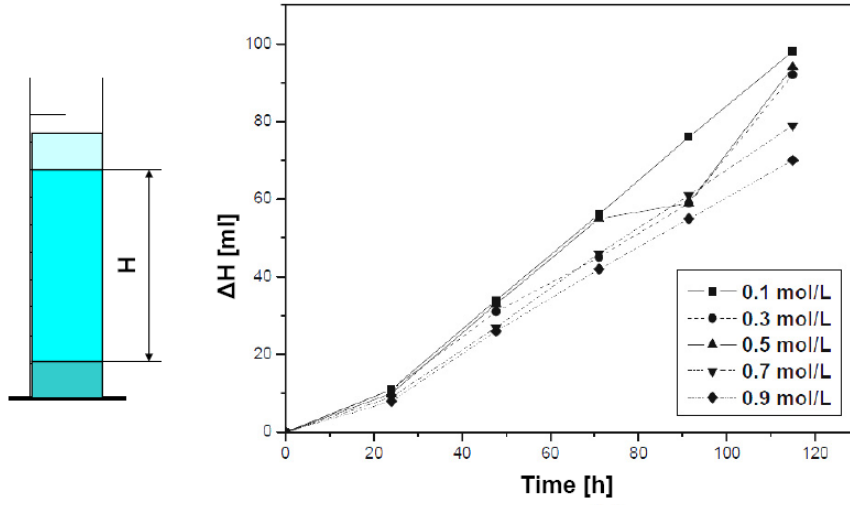
Figure 4.20: Change in dispersion height (ΔH) of the sulfate electrolyte with alumina particles in dependence on the ageing time of the electrolyte at different citrate concentrations. The considered dispersion height is indicated by H on the cylinder presenting the phases formed after a certain ageing time.

the sinking velocity appears to be slower since the change in dispersion height reached at longer age is low compared to the other concentrations.

Assuming that the sinking velocity determined from Figure 4.20 is constant during the sedimentation experiment, the average agglomerate size is calculated based on the balance of forces applied on each particle. The balance of forces, illustrated in Figure 4.21, is presented in the equation

$$F_g - F_R - F_A = 0 \tag{4.1}$$

in which F_g, F_R and F_A refer to the weight, friction force and buoyancy force, respectively.

The agglomerate diameter d is consequently given by the following equation:

$$d = \sqrt{\frac{18\,\eta\,v}{g\,(\rho_F - \rho_T)}} \tag{4.2}$$

where ρ_T is the particle density. Knowing that $f = 6\pi\eta r$ where η = fluid viscosity, and ρ_F = 1 g / cm^3, ρ_T = 3.94 g / cm^3, η = 1 mPa·s and g = 10 m / s^2, the calculated agglomerate diameter values are plotted in Figure 4.22 in dependence on the citrate concentration in the
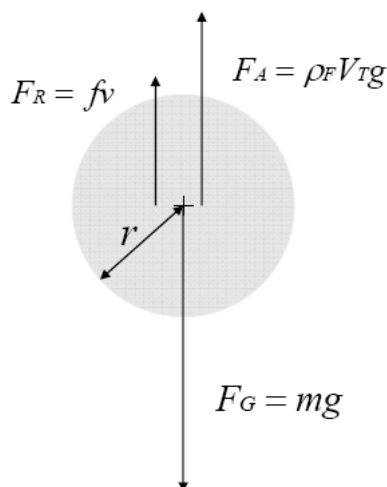
Figure 4.21: Schematic showing the forces applied on a particle moving in the electrolyte. m = particle mass, r = particle radius, V_T = particle volume, v = sinking velocity of a particle f = friction coefficient, g = acceleration of gravity, ρ_F = liquid density.

electrolyte. A first view indicates that all the agglomerates show a diameter range below 550 nm. In addition, the higher the citrate concentration in the solution is, the smaller the agglomerates formed in the electrolyte are.

Effect of the nickel ions concentration on the current efficiency and the electrodeposited material

Some Ni-Al$_2$O$_3$ layer depositions were carried out at different nickel ions concentrations varying in the range of 0.06 and 1.06 mol/L. The resulted layers were weighed and the appropriate current efficiency was determined.

The plot in Figure 4.23 presents the dependence of the current efficiency on the nickel concentration. The current efficiency increases when increasing the amount of Ni-ions to reach a saturation value of about 90 % at concentrations higher than 0.2 mol/L. The layer electrodeposited from the electrolyte containing 0.26 mol/L Ni-ions was observed with SEM and is presented in the micrographs in Figure 4.24 a and b. Figure 4.24 a shows an overview at the surface while Figure 4.24 b presents the cross section of the material.

We can notice from the plan-view of the layer (Figure 4.24 a) that the obtained material shows a smooth surface comprising submicron sized pores that are randomly distributed.
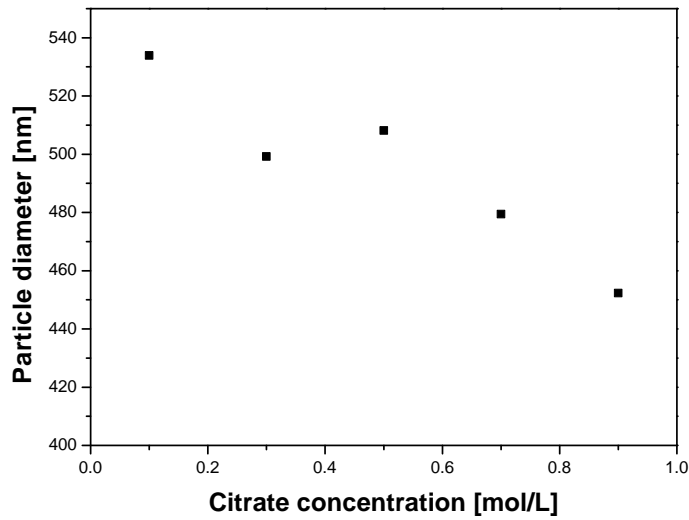
Figure 4.22: Dependence of the alumina agglomerate diameter on the citrate concentration in the electrolyte
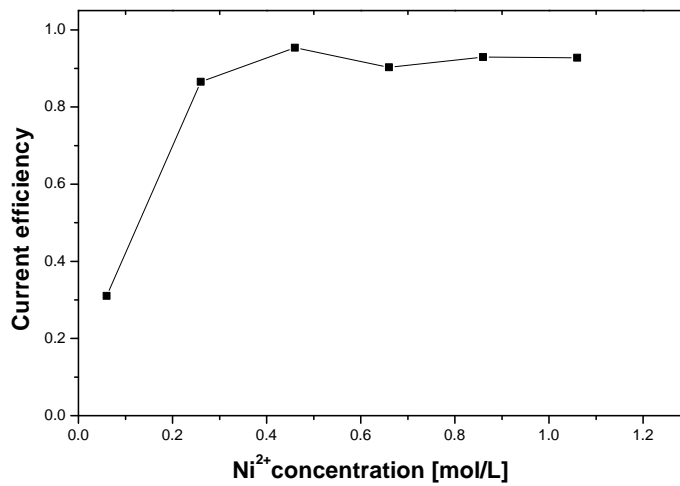
Figure 4.23: The current efficiency of the nickel-alumina electrodeposition in dependence on the nickel concentration
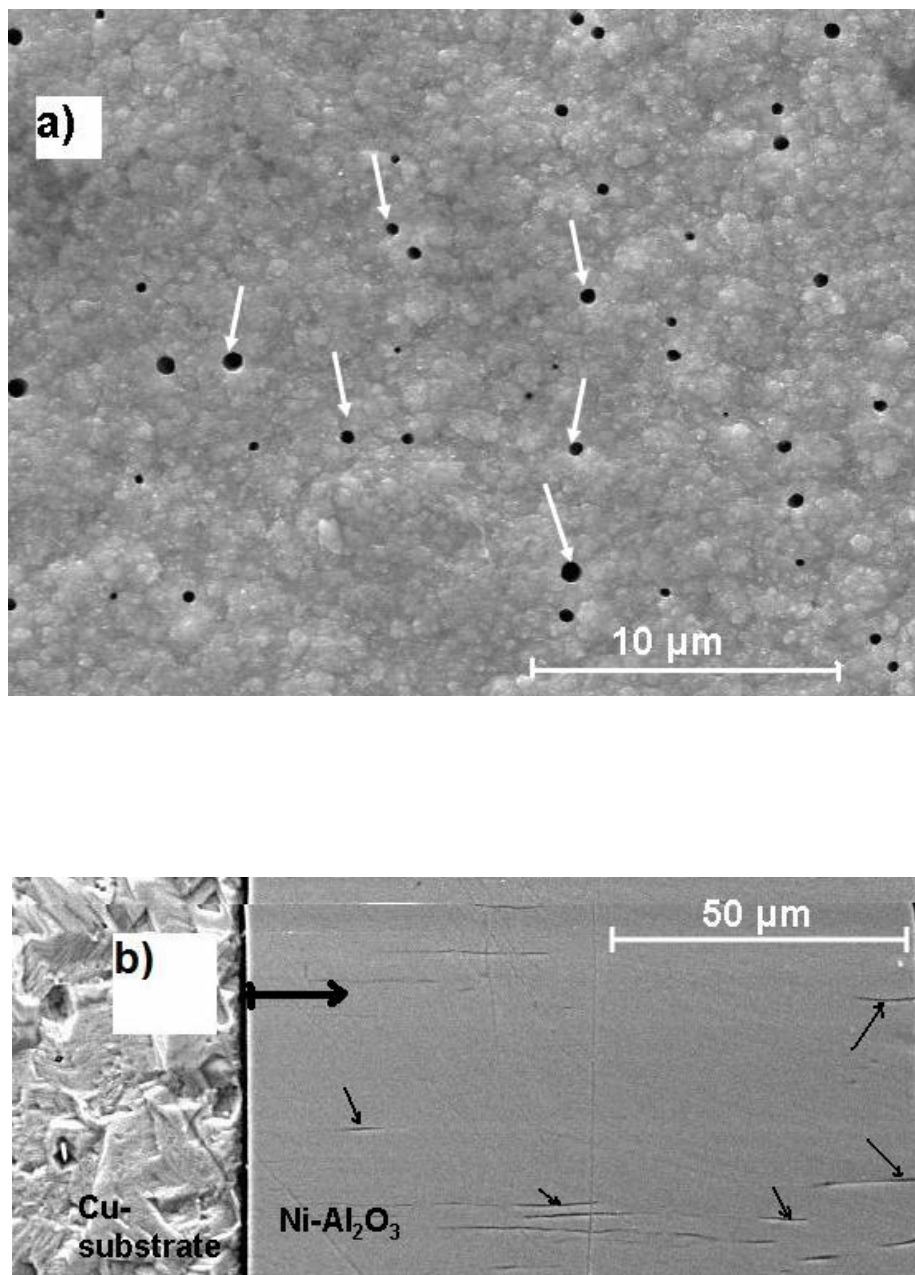
Figure 4.24: SEM-micrograph of an electrodeposit obtained from a nickel sulfate electrolyte containing Al_2O_3 particles, the Ni^{2+} concentration is 0.26 mol/L. a- overview showing pores indicated by arrows, b- cross-view showing pores elongated in the growth direction (see bold arrow) and indicated by arrows.

The cross section (Figure 4.24 b) presents a compact material with pores that are elongated in the growth direction. Their size is $\leq 1\ \mu$m in the cross direction, which is comparable to the size of the ones observed on the plan-view.

A picture of the layer on the copper substrate obtained from the solution with high Ni-concentration (1.06 mol/L) is shown in Figure 4.25. The electrodeposited Ni-Al$_2$O$_3$ layer demonstrates cracks and even the release of the layer from the substrate at several points as indicated in Figure 4.25. Ni-Al$_2$O$_3$ is observed underneath the delaminated parts, which confirms the beginning of this effect during the electrodeposition.

Figure 4.25: A Ni-Al$_2$O$_3$ layer on copper substrate electrodeposited at a Ni^{2+} concentration of 1.06 mol/L. Cracks at the surface are indicated by arrows. The circle surrounds a delaminated part. Underneath the latter electrodeposited Ni-Al$_2$O$_3$ is observed.

Effect of the ratio Ni^{2+} to NH$_4{}^+$ concentration on the stability of the ammonia-citrate sulfate solution

In order to increase the nickel ammonia complex concentration in the electrolyte without formation of precipitates, the ammonia-citrate sulfate electrolyte was studied while varying the ratio Ni^{2+} to NH$_4{}^+$ concentration before adding the alumina nanoparticles. In Table

4.7, the important features observed on several solutions with different Ni^{2+} and NH_4^+ concentrations are summarized.

Table 4.7: Variation of the ratio $C(Ni^{2+})$ / $C(NH_4^+)$ in the sulfate dispersion and important observations

Exp. n	$c(Ni^{2+})$ [mol/L]	$c(NH_4^+)$ [mol/L]	$c(Ni^{2+})/c(NH_4^+)$	Remarks
1	0.36	0.7	0.51	Formation of a white precipitate after few minutes. pH (after a day) = 3.74
2	0.36	0.8	0.45	Solution is originally from Exp. 1 with adding NH_4^+. White old crystals dissolved while adding NH_4^+. New white precipitate after one day
3	0.36	0.855	0.42	NH_4^+ added to the solution in Exp. 2. Old white crystals dissolved after adjusting pH to 8.5. After few days, new precipitate formed and pH = 6.9
4	0.26	1.3	0.2	pH adjusted to 8.5. A white precipitate observed on the next day
5	0.26	1.5	0.17	NH_4^+ added to the solution in Exp. 4. pH adjusted to 8.5. The old crystals still to see
6	0.26	2.16	0.12	pH adjusted to 8.5. No precipitate observed in the first few days.
7	0.06	0.5	0.12	pH adjusted to 8.5. No precipitate observed.

It is important to note that the precipitate seen most often in Table 4.7 is formed relatively fast (at the moment of the solution preparation) in the case of high $c(Ni^{2+})$ to $c(NH_4^+)$ ratio (0.514). At ratio values between 0.5 and 0.17, the precipitation of the white crystals takes a longer time and varies from case to case. Moreover, the pH value also has an influence on the precipitation. In fact, at pH values higher than 8, the precipitation is delayed and the crystals can be dissolved as demonstrated in Exp. 3.

Further investigations, consisting in the electrodeposition of pure nickel layers before detecting any precipitate in the solutions, were realized for Exp. 3, 6 and 7. In the electrolyte, the concentration of citrate is chosen to be 0.9 mol/L and those of the other components remain the same as in Table 4.6.

Exp. 3

The layer resulted from Exp. 3 showed several cracks at the surface and was released from the substrate apparently during the electrodeposition, since new material is growing underneath the released parts. The XRD measurements carried out on this layer yield the spectrum in Figure 4.26.
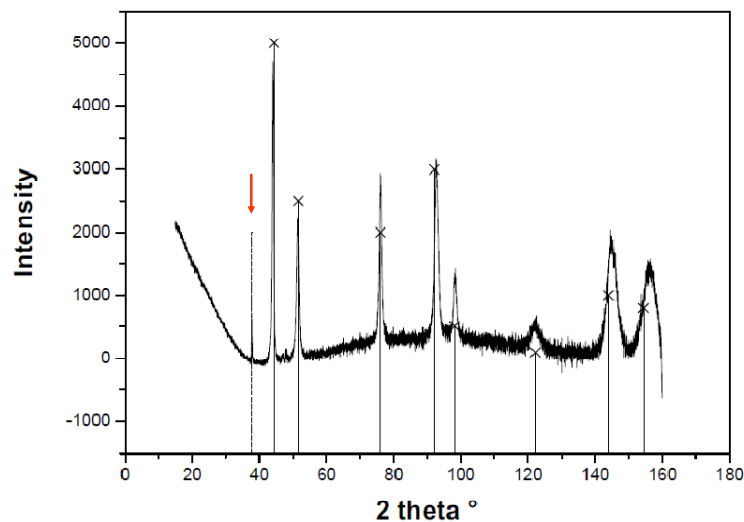
Figure 4.26: XRD-diffractogram obtained after scanning the layer electrodeposited from Exp. 3. The peaks indicated by the black lines refer to those of nickel, while the peak indicated by the red arrow corresponds to a different phase that may be either nickel oxide hydroxide, nickel oxide or nickel hydroxide.

For angle values higher than 40°, the detected peaks correspond to the nickel peaks indicated by the continuous lines. At a range lower than 40°, a smaller peak refers to a different phase. Compared to data in the database, the position of this peak is close to that of some peaks shown by nickel oxide hydroxide, nickel oxide and nickel hydroxide. The microhardness was also determined for this layer. It shows values in the range of $550 \ldots 580$ HV which is clearly higher than the values expected for pure nickel.

Exp. 6 and 7

The electrodeposited material obtained from Exp. 6 presents a black layer unlike the usual grey nickel and whose microhardness values are higher than 600 HV. The last experiment (Exp. 7), however, resulted in a layer showing a grey surface comparable to the nickel surface and microhardness values lower than 300 HV.

Electrodeposition of microspecimens

Some electrodepositions of Ni-Al$_2$O$_3$ were carried out on the LIGA micropattern presented in Figure 3.1. The purpose of such electrodepositions consists of studying the effect of several process parameters on the fabrication of microspecimens for further use in the mechanical testing of the microspecimens. In all of the following experiments, the citrate and ammonium chloride are 0.9 and 0.5 mol/L, respectively. The other parameters are adjusted similar to those described in Table 4.6. The current density, the nickel concentration in solution and the type of the used anode present the only varied parameters.

In the first experiment, a soluble nickel anode was used. The concentration of nickel ions of 0.06 mol/L was dosed in the electrolyte. The current density was kept to 2 A / dm^2. The cross section of an obtained microspecimen is shown in the micrograph Figure 4.27.

Figure 4.27: SEM-micrograph of a microspecimen cross section electrodeposited from a sulfate dispersion at Ni^{2+} concentration of 0.06 mol/L and using a soluble anode. The current density is 2 A / dm^2. The growth direction is indicated by the bold arrow. Two different regions are observed: region 1 presenting numerous voids, region 2 shown to be compacter.

The resulted material shows a very rough surface and high thickness that exceeds $300\ \mu$m in some areas. On the cross section we can distinguish between two regions indicated in Figure 4.27. In region 1, the material demonstrates a dendrite structure pointing in the growth direction of the electrodeposition (see Figure 4.27) and dispersed voids with different shapes. However, region 2 shows compact material trying to close the voids formed in region 1. This material seems to overgrow the resist since the traces left by the resist pattern are shown near the edge of the electrodeposited microspecimen (see dashed line in Figure 4.27).

Figure 4.28: Al_2O_3 content determined by point EDX-measurements on the cross section of the Ni-Al_2O_3 microspecimen presented in Figure 4.27.

The composition distribution measured along the cross section of the microspecimen in Figure 4.27 is shown in Figure 4.28 . The latter illustrates the point measurements realized at $10\ \mu$m spaced positions. It is then noted that the measured compositions vary between 3.32 and 1.17 wt% except two outliers showing higher alumina content.

In the next microspecimens' electrodeposition, the parameters are maintained as mentioned for the last experiment. This time however, an inert anode is used. The result of

this electrodeposition is presented in the micrograph in Figure 4.29 and shows the cross section of the gage section of a microspecimen still sitting on the wafer and observed after the resist stripping.
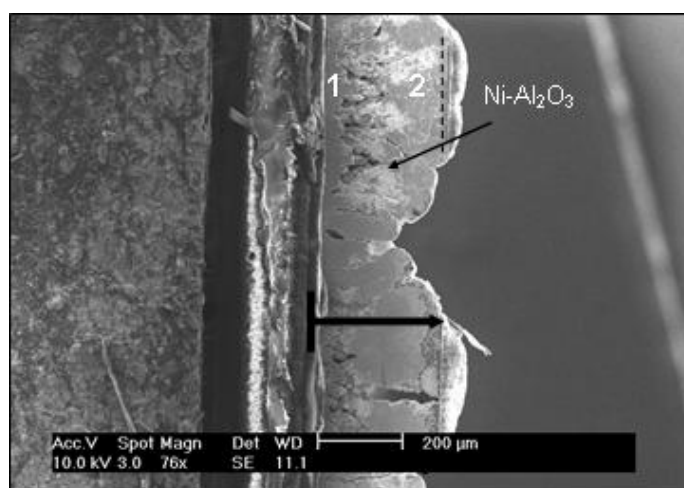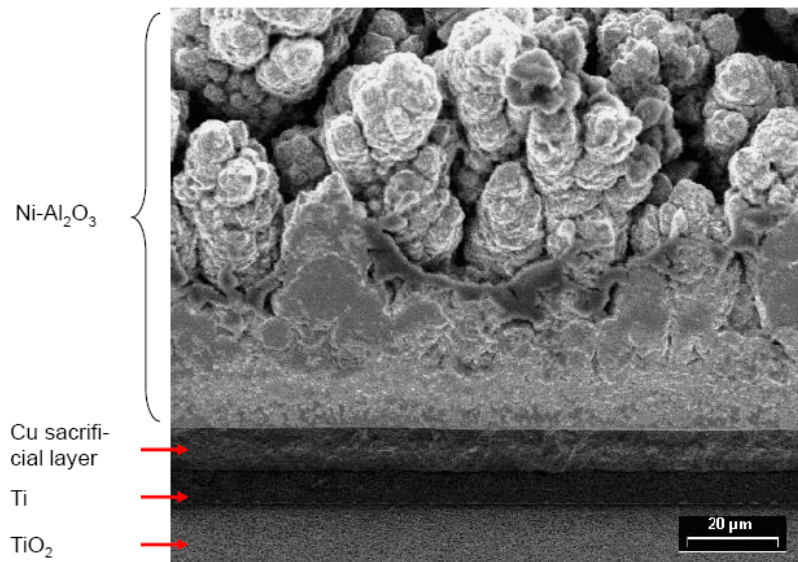

Figure 4.29: SEM-micrograph of a microspecimen cross section electrodeposited from a nickel sulfate dispersion at Ni^{2+} concentration of 0.06 mol/L and using an inert anode. The current density is 2 A / dm^2. This microspecimen, presented after PMMA stripping, is still attached to the wafer. It is released from TiO_2 at some places, where titanium is to see.

The material in Figure 4.29 presents a non-compact dendrite structure resulting in a rough surface. In addition, a gap between the microspecimen and the substrate demonstrates the release of the material at some areas. The release of the microspecimen seems to happen from titanium since the surface appearing below the material is darker than the one of the substrate (TiO_2).

In the last experiment, the current density was reduced to 1 A / dm^2. The other parameters remained similar to those of the electrodeposition of the specimen shown in Figure 4.29. The gage section of an obtained microspecimen is shown in the following micrograph (Figure 4.30).

If we consider the cross section, we note that the electrodeposit appears to be more compact and the surface relatively rough especially at several areas where the material shows spherical knolls. The gap observed below the specimen confirms the release of the material
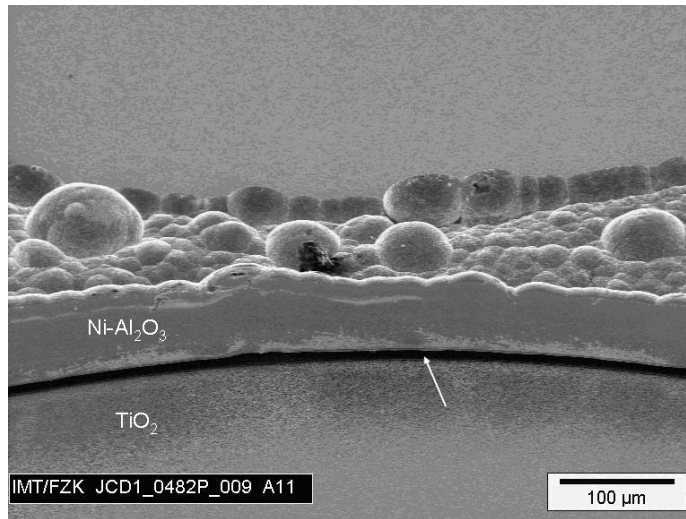
Figure 4.30: SEM-micrograph of a microspecimen crosssection electrodeposited from a sulfate citrate electrolyte at Ni^{2+} concentration of 0.06 mol/L and using an inert anode. The current density is kept to 1 A / dm^2. The microspecimen, presented after PMMA stripping, is still attached to the wafer. A gap underneath the specimen is to see as indicated by the arrow.

from the substrate. This aspect has been also mentioned in the explanation of Figure 4.29. The composition of the material across the microspecimen was studied and is shown in the plot in Figure 4.31. The latter gives an overview about the chemical composition of the electrodeposit in dependence on the position on the cross section. The spacings between the point measurements are fixed to be about 10 μm.

It is clear that the measurements vary around an average of 1.34 wt% Al_2O_3 content in a deviation range of $\pm$ 0.21 wt%. The deviation estimated from the plot in Figure 4.31 corresponds to 15.7% of the mean value of the alumina content embedded in the electrodeposited nickel matrix.

4.2.2 Microstructure investigations and microhardness measurements in the as-deposited state and after annealing

Layer electrodepositions were carried out from several electrolytes investigated in Section 4.2.1. For the obtained material, further microhardness and microstructure studies were realized in the as-deposited state as well as the annealed one and are presented in this paragraph.
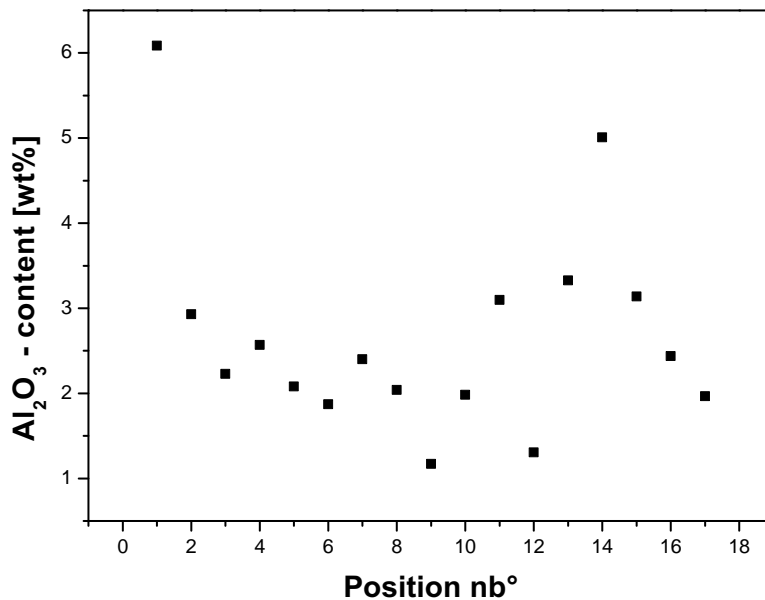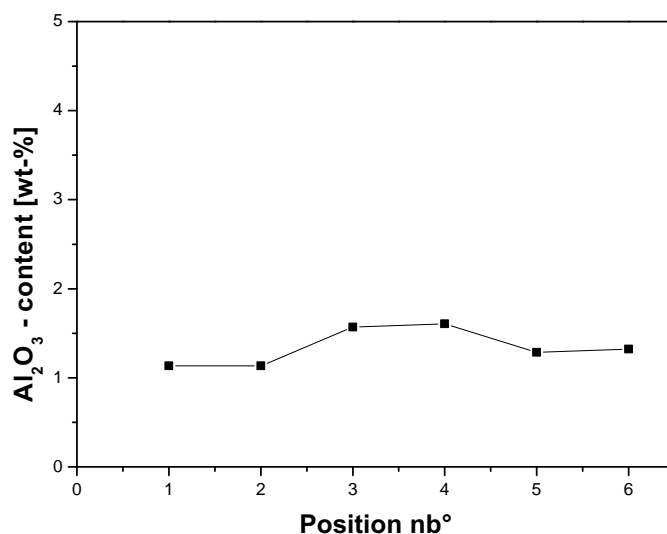
Figure 4.31: Al_2O_3 content determined by point EDX-measurements on the cross section of a Ni-Al_2O_3 microspecimen presented in Figure 4.30. Its thickness is estimated to be around 60 μm.

First of all, both dispersion strategies are compared in Figure 4.32 and show the microhardness of some layers resulting from electrodepositions with different parameters. Al1 and Al2 stand for the layers electrodeposited at different current densities from the dispersion containing hydrophobic Al_2O_3. Al3, Al4 represent the layers obtained from the sulfate electrolyte containing hydrophilic alumina. The citrate and nickel concentration in the latter electrolyte were adjusted to 0.5 and 0.06 mol/L, respectively. For comparison, pure nickel was also electrodeposited from this electrolyte before adding the alumina particles and is labeled in Figure 4.32 with "pure Ni". The microhardness of Al3 and Al4 values varying in the range 400 to 525 HV which is higher than the one of pure nickel electrodeposited from the same electrolyte (in the range of 200 to 300 HV). However, the microhardness of the layers Al1 and Al2 resulting from the sulfamate electrolyte with the hydrophobic particles demonstrates no change compared to the microhardness of the pure nickel electrodeposited from this same electrolyte estimated to be between 200 and 300 HV [102], which is also in agreement with the range measured for the pure nickel resulting from the sulfate electrolyte. Some Ni-Al_2O_3 layers obtained from the sulphate electrolyte with comparable parameters to those of the electrodeposition of Al3 and Al4
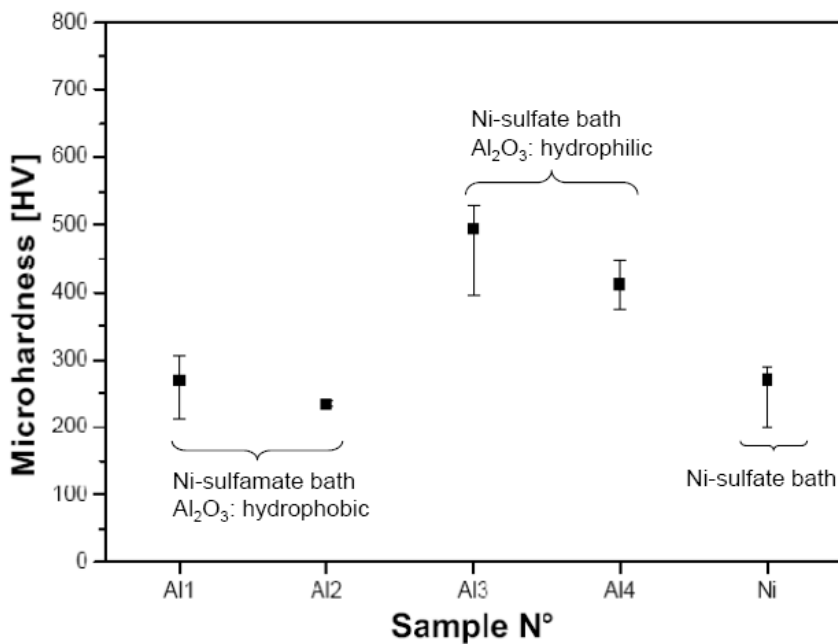
Figure 4.32: Microhardness values of Ni-Al$_2$O$_3$ layers electrodeposited from different electrolytes

were annealed at different temperatures over the course of 2 hours. The microhardness investigations of these samples are presented in Figure 4.33 and compared to those of pure Nickel. The microhardness values of the latter were presented in Section 4.1.2, and in Figure 4.9. The microhardness values of Ni-Al$_2$O$_3$ are shown to be higher than those of pure Nickel in the as-deposited as well as annealed state. After annealing at intermediate temperatures (300 - 400 ^{o}C), the microhardness remains almost unchanged and drops at higher temperature (500 - 600 ^{o}C) but reaching values higher than those of pure nickel in the as-deposited state.

Microstructural investigations using the microscopy methods mentioned in Paragraph 3.2 are carried out for Ni-Al$_2$O$_3$ specimens electrodeposited from different sulfate electrolyte containing hydrophilic particles. The micrograph in Figure 4.34 shows a HR-SEM picture of a cross section realized by FIB cutting through the sample Al3 (see Figure 4.32) in the as-deposited state. Frequent agglomerates are observed on the cross section as indicated with the circles in Figure 4.34. The diameter of such agglomerates is estimated to be in the range of several hundred nanometers but smaller than 500 nm. The chemical
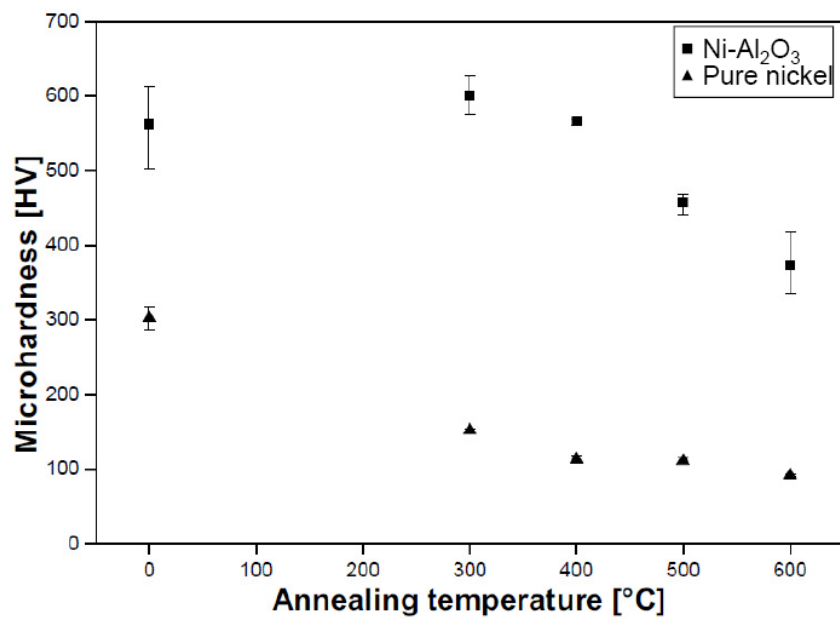
Figure 4.33: Microhardness of LIGA Ni and LIGA Ni-Al$_2$O$_3$ alloys and its dependence on the annealing temperature (2h duration).
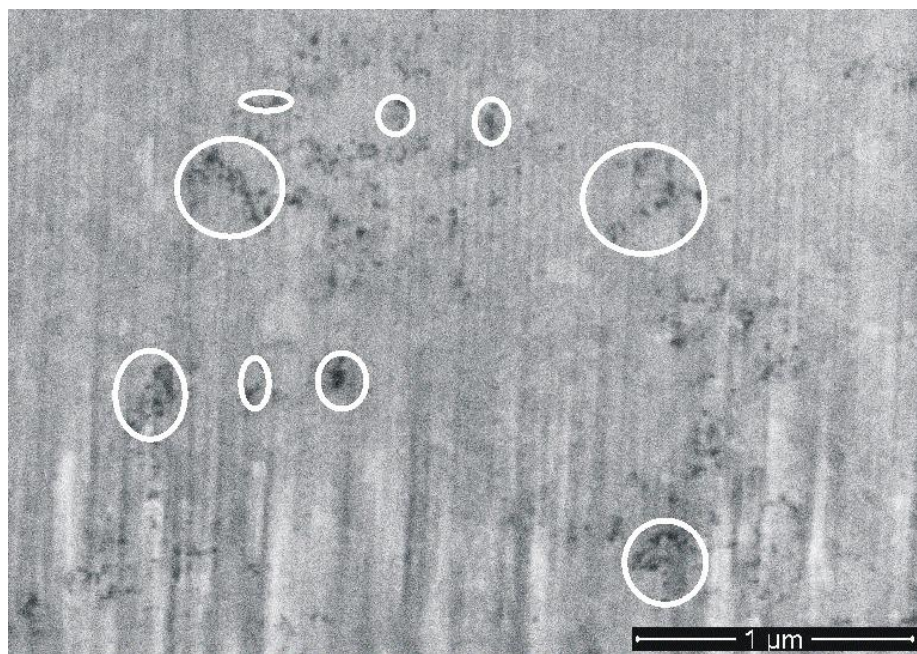
Figure 4.34: HR-SEM image of a FIB-cut Ni-Al$_2$O$_3$ layer, sample Al3 (see Figure 4.32 in the as-deposited state). The circles show several Al$_2$O$_3$ agglomerates.

composition of such layers determined by EDX is estimated to be about 1.75 wt% Al_2O_3 which corresponds to 3.84 vol% Al_2O_3.

Further TEM investigations shown in the micrographs Figure 4.35 and Figure 4.36 are established on Ni-Al_2O_3 disks resulting from a current density of 2 A / dm^2 from a sulfate electrolyte showing a citrate and nickel concentration of 0.9 and 0.06 mol/L, respectively. The observed grains are all in the submicron range. Few of them are shown to be relatively large with a size of several hundred nanometers (see Figure 4.35), whereas the size of some dispersed grains is estimated to be smaller than one hundred nanometers as indicated in Figure 4.35. Numerous twins presented by the darker lines across the grain in Figure 4.36 present a remarkable feature in the TEM micrographs. The clear white random-shaped voids, observed especially in Figure 4.35, resulted from the preparation of TEM samples. The spherical white particles are aluminum oxide which was confirmed by the EDX measurements realized on those particles. From the observations of many areas, the size of the particles is estimated to range between 20 and 80 nm. It is also noted that the particles are embedded inside the grains as demonstrated in Figure 4.36. The layer shown
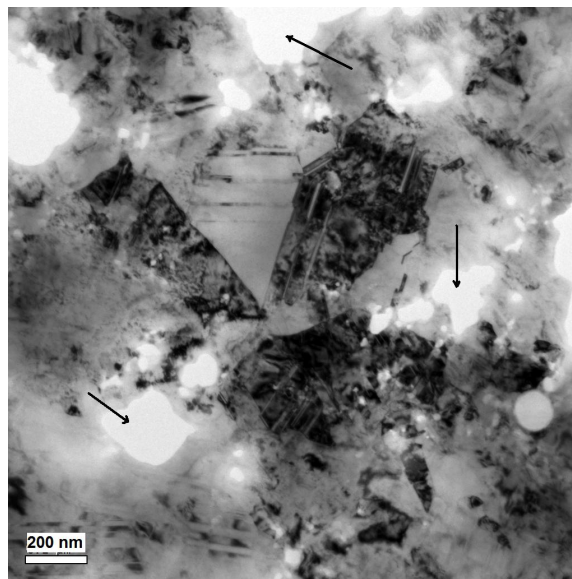
Figure 4.35: TEM-image of a Ni-Al_2O_3 TEM-disk electrodeposited according the parameters used to electrodeposit the micrcrospecimens shown in Figure 4.29. The arrows indicate several voids.

in Figure 4.37 has been annealed at 600 ^{o}C for 2 hours and compared to the as-deposited one in the micrographs Figure 4.37. Thanks to the higher channeling contrast resulting
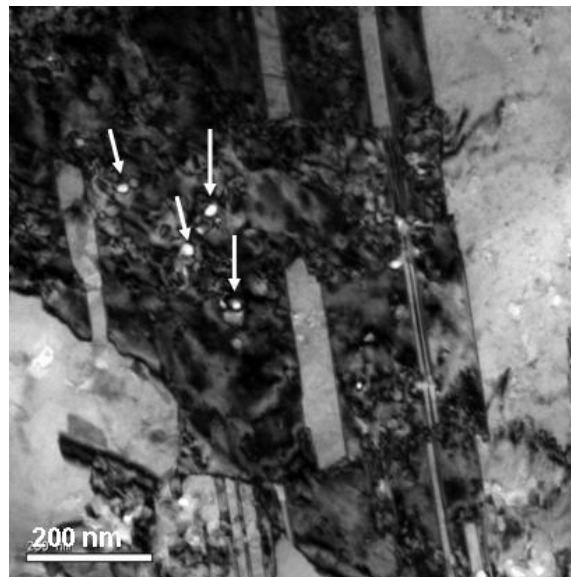
Figure 4.36: TEM-image of a Ni-Al$_2$O$_3$ TEM-disk electrodeposited according to the parameters used to electrodeposit the microspecimens shown in Figure 4.29. The arrows show Al$_2$O$_3$ nanoparticles.
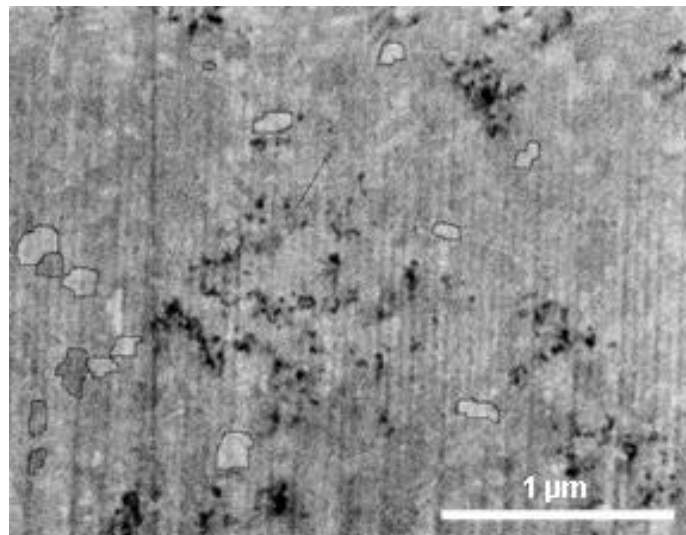
Figure 4.37: HR-SEM image of a FIB-cut Ni-Al$_2$O$_3$ layer, sample Al3 (see Figure 4.32 in the as-deposited state). Several grains are illustrated by drawn contours resulting in an estimated average grain size of circa 100 nm.

from the ion beam, some grains could be identified in Figure 4.38. The average grain size of these grains is estimated at 500 nm, which represents a higher value than the grain size of the layer in the as-deposited state shown to be 100 nm. However, in Figure 4.37 the grain boundaries are difficult to see because the contrast delivered by SEM is not sufficient and the observed grains are too small to make quantitative investigations.
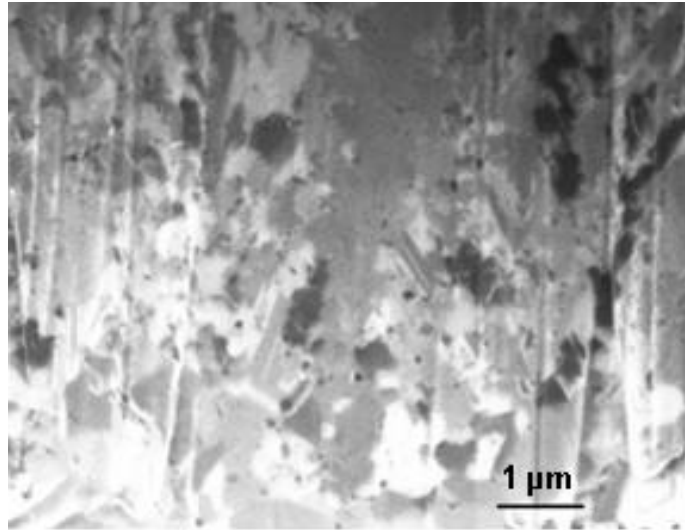
Figure 4.38: FIB-image of a Ni-Al$_2$O$_3$ cross section annealed at 600 ^{o}C for 2 hours, sample Al3 (see Figure 4.32).

4.2.3 Tensile tests at room temperature

The microspecimens showing no defects were tested for the purpose to determine the mechanical properties of Ni-Al$_2$O$_3$. Before carrying out the tensile test, some microsamples were polished down to a thickness where they present a uniform section.

The first obtained stress-strain curve of Ni-Al$_2$O$_3$ at room temperature is illustrated in Figure 4.39 and compared to the stress-strain response of Ni-W showing compositions studied in Section 4.1.3.

It is worth noting that fracture stress of Ni-Al$_2$O$_3$ reaches a value of approximately 1.2 GPa which is high compared to pure nickel and in the range of the fracture stress determined for Ni 15 at% W and Ni 5 at% W (see Table 4.3 and 4.4 in Section 4.1.3). The Young's modulus is estimated to 150 GPa by linear regression. This value is slightly smaller than
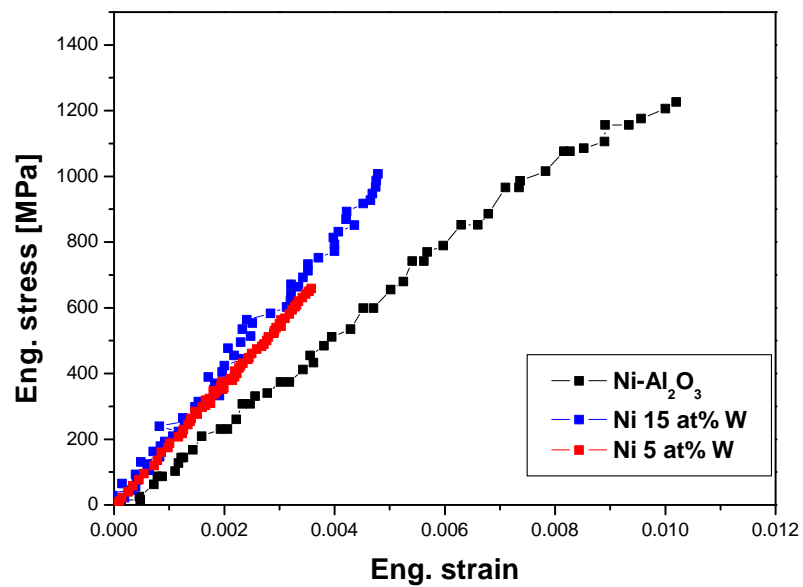
Figure 4.39: Stress-strain curve of a Ni-Al$_2$O$_3$ specimen in the as-deposited state compared to those of Ni-W containing 15 at% W and 5 at% W [105]. The strain rate is fixed to $2 \cdot 10^{-4} s^{-1}$.

those of the Ni-W alloys (see Table 4.3). The fracture of the microspecimens occurs after negligible plasticity as observed for the Ni-W samples.

4.3 Ni-base superalloy

4.3.1 Ni-Al electrodeposition process parameters

In order to demonstrate the feasibility of using electrodeposited Ni-Al composites in producing Ni-base superalloys, an electrolyte has been developed based on the experience acquired for the fabrication of Ni-Al$_2$O$_3$. Its chemical composition is summarized in Table 4.8. The role of each component in the electrodeposition of Ni-Al is comparable to

Table 4.8: Chemical composition of the electrolyte used for the electrodeposition of Ni-Al

Component	Concentration [mol/L]
Nickel sulfate · 6 H_2O	1
Sodium citrate · 2 H_2O	1
Ammonium chloride	0.5
Sodium bromide	0.15
Aluminum particles	0.49

that explained in the section for codepositing hydrophilic Al$_2$O$_3$ in the nickel matrix. Two different-sized Al-particles, whose effects on the electrodeposits have been studied, are added in the electrolyte. The larger ones are microparticles and show an average diameter of 10 μm. The smaller ones present nanoparticles with a diameter size varying between 70 and 150 nm manufactured by "Advance Powder Technologies" in Tomsk (Russia). The pH of the solution is kept in the neutral range (7 to 7.6). Different temperatures are set for the electrodeposition of the Ni-Al layers. The experiments are carried out at a current density of 2 A / dm^2.

4.3.2 Characterization of the Ni-Al electrodeposits

Incorperation of aluminum microparticles

The result of the electrodeposition with microparticles is demonstrated in the micrographs of Figure 4.40. A dendritic structure oriented in the growth direction of the electrodeposit

is observed in the cross section shown in Figure 4.40 a. This results in an enormous roughness at the surface of the electrodeposit as illustrated in Figure 4.40 b. The observed darker regions having different size are aluminum particles that are surrounded by brighter areas representing nickel as indicated in Figure 4.40 (above). This is also confirmed by EDX measurements carried out on the corresponding place. If we consider the overview of the Ni-Al layer (Figure 4.40 b), we can see nucleation of nickel starting at the surface of the spherical aluminum particles whose size is in the same range as for the nominal diameter of the microparticles.

Furthermore, a few days after the electrodeposition, the electrolyte looks different than when it started. A thick metallic precipitate is also observed in the clear solution showing a changed color compared to its original color.

Incorporation of aluminum nanoparticles

Table 4.9: Ni-Al layers, named NiAl1, NiAl2, NiAl3 and NiAl4, and their corresponding electrodeposition parameters

Sample label	Current density [A / dm^2]	Temperature [^{o}C]	Duration [min]
NiAl1	2	25	269
NiAl2	2	50	63.5
NiAl3	1	50	120
NiAl4	4	50	120

Table 4.9 shows several layer electrodepositions carried out from the electrolyte that contains the nanoparticles from a 24 hour time period. In these experiments, the temperature and the electrodeposition were varied. Table 4.9 summarizes the electrodeposition parameters of the obtained layers, labeled NiAl1 … NiAl4 in chronological order. The layers obtained from the electrodepositions shown above are illustrated in Figure 4.41.

NiAl1 and NiAl2 show bright grey layers with apparently smooth surfaces, while the layers NiAl3 and NiAl4 are darker especially NiAl4 and present numerous buds at their surface.

Roughness data of the electrodeposits are determined and plotted in Figure 4.42. A rising trend of the plot is observed in which the roughness of the layers increases when the
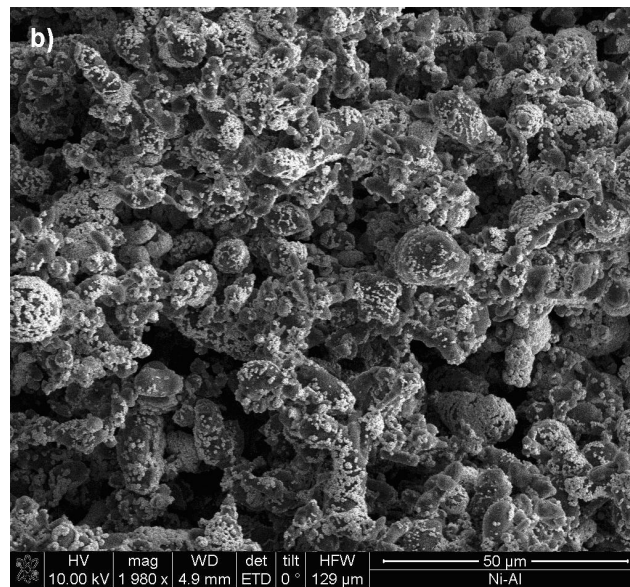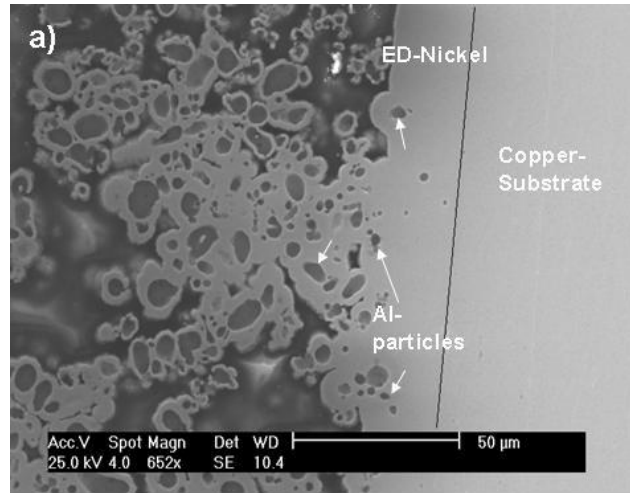
Figure 4.40: SEM-image of Ni-Al layer which is attached to copper substrate and electrodeposited from the Ni-Al electrolyte containing microparticles. a: cross view, b: overview.
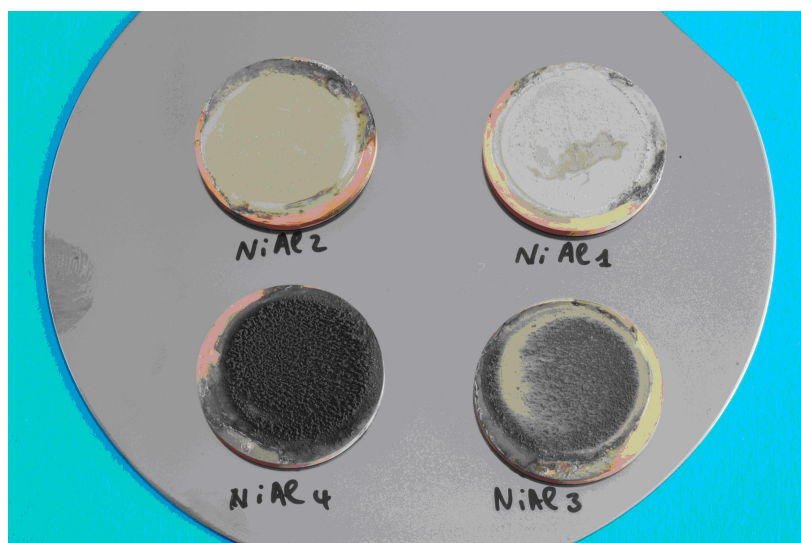
Figure 4.41: Photograph of Ni-Al layers on copper substrate. The corresponding electrodeposition parameters are given in Table 4.9.

electrolyte becomes older. After less than approximately 8 hours, a small change in the roughness values is noticed. After more than 20 hours, a sharp rise in the roughness height occurs as a result of an enormous roughness value higher than 200 μm that was obtained from the electrolyte aged for 25 hours.

A few hours after the last electrodeposition, the aged electrolyte looks comparable to the one with the microparticles after longer aging. In addition gas bubbles are to see migrating from the metallic precipitate to the surface of the solution.

The layers NiAl1 and NiAl2, which showed lower roughness, are used for further microscopic investigations. The cross sections of NiAl1 and NiAL2 are presented in the micrographs Figure 4.43 and Figure 4.44, respectively. Both observed electrodeposits show a compact structure unlike the layers containing microparticles (see Figure 4.40). NiAl1 is thicker than 100 μm and presents homogeneously distributed particles proven by EDX to be aluminum. These particles are incorporated in the form of agglomerates whose diameter is estimated to be about 1 μm (Figure 4.43). Inside the agglomerate the separated particles are clearly seen with a diameter range similar to that of the nominal particles as given in the specification data (between 70 and 150 nm). Moreover, the NiAl2 layer has a smaller thickness estimated to about 30 μm. The agglomerates presenting similar diameter are less uniformly distributed compared to NiAl1. In the most cases, they include a larger
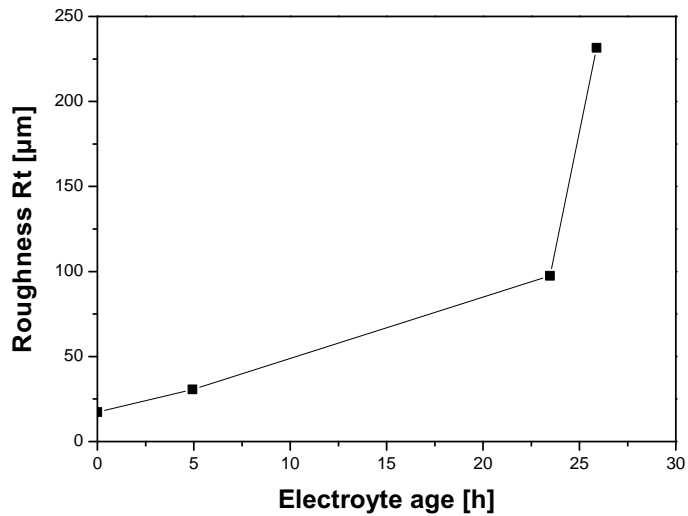
Figure 4.42: Roughness range (R$_t$) of the Ni-Al layers shown in Figure 4.41 in dependence to the electrolyte age. The measured area on each layer is 5 mm.

particle with a diameter about 500 nm, as indicated in Figure 4.44, surrounded by particles showing a diameter comparable to the nominal one.

The chemical composition within the investigated layers was determined by means of EDX and chemical analysis. The first method delivers an average composition of 2.3 and 1.7 at% aluminum in NiAL1 and NiAl2, respectively, while the second yields a layer containing 3.72 ± 0.29 at% aluminum for NiAl1 and 4.54 ± 0.23 at% for NiAl1.
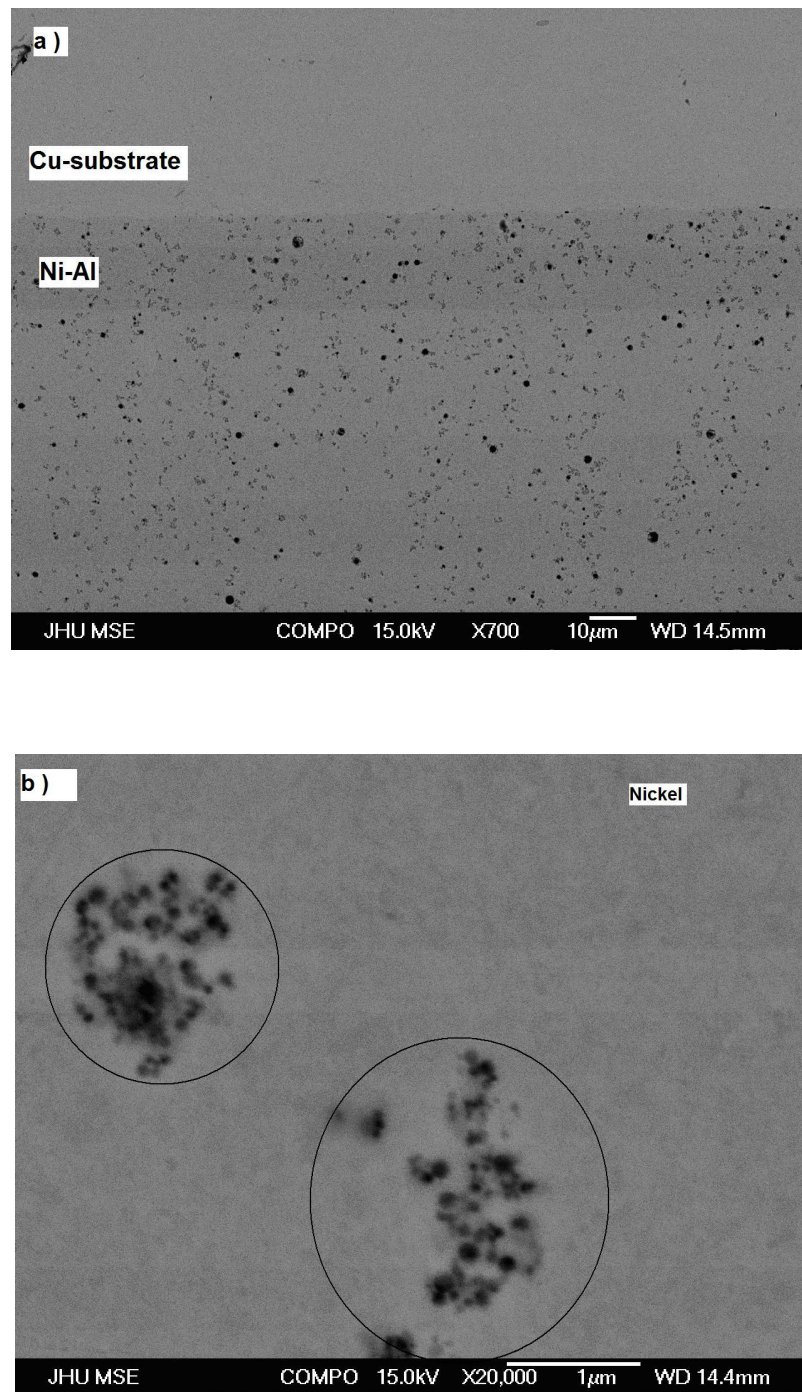
Figure 4.43: SEM-images of the NiAl1 (see Table 4.9) cross section at different magnifications (a, b) [106]. The layer is attached to the copper substrate. Several aluminum agglomerates are illustrated inside circles (b).
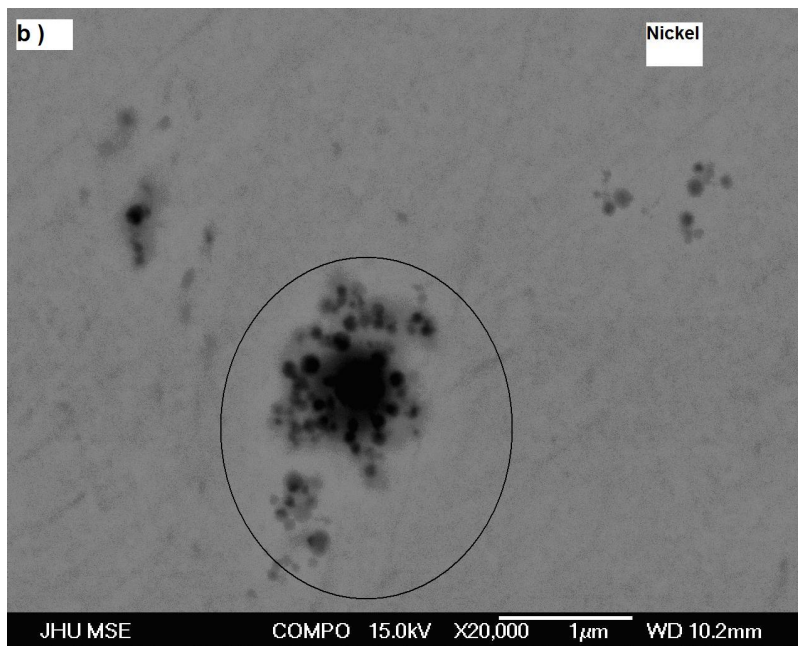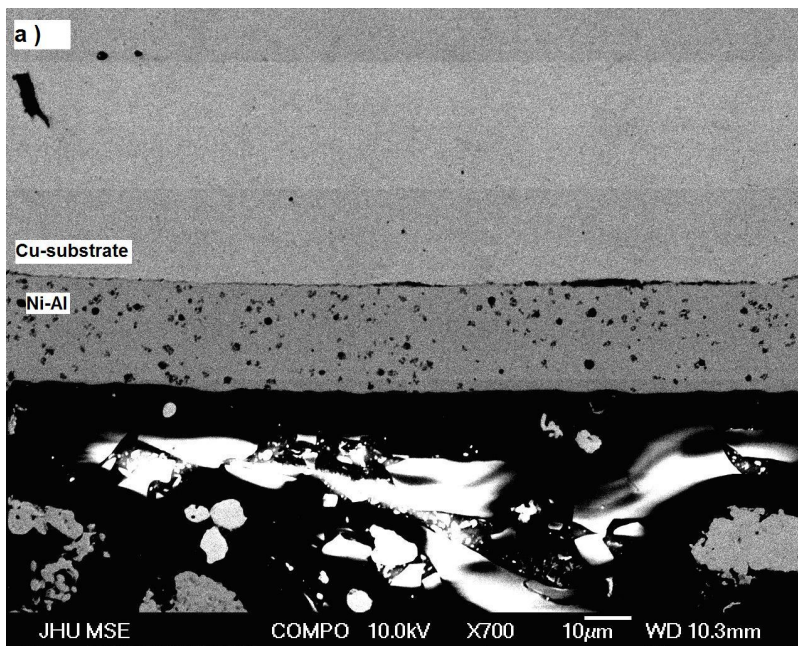
Figure 4.44: SEM-images of the NiAl2 (see Table 4.9) cross section at different magnifications (a, b) [106]. The layer is attached to the copper substrate. An aluminum agglomerate is illustrated inside the circle (b).

5 Discussion

5.1 Ni-W

5.1.1 Electrodeposition process

Within this work, alkaline ammonia citrate electrolytes with two different chemical compositions were used to electrodeposit an alloy with different W content. The obtained material showed a W concentration of 5 at% and 15 at% in solid solution. These alloy compositions are interesting for further mechanical testing and microstructure investigations for later use in high temperature MEMS applications. In fact, if we take a look at the phase diagram of Ni-W (Figure 5.1), we can notice that Ni-W represents a solid solution up to approximately 13 at% throughout the temperature range RT - melting point. Choi 2003 [36] demonstrated that electrodeposited Ni 18 at% W alloy is in the form of a solid solution which is maintained up to a temperature of 700 ^{o}C. Only at temperatures higher than 700 ^{o}C, the formation of the ordered Ni$_4$W phase begins, which, according to the phase diagram in Figure 5.1, should normally occur irrespective of the annealing temperature at W concentrations higher than approx. 13%. The deviation of this finding from the features in the phase diagram is due to the electrodeposition resulting in a material out of the thermodynamically stable state. In addition, increasing the content of incorporated W in the alloy can result in amorphous material after Yamasaki [98] who demonstrated the appearance of amorphous phases at concentrations higher than 20 at%. Amorphous material is known for its lack of ductility, which has to be avoided for the applications required from the electrodeposited LIGA part. The compositions of the tested material are consequently chosen to be Ni 5 at% and Ni 15 at% W in a solid solution form. Hence, these alloys are applicable for later use in the fabrication of microparts with defined functionality.

The temperature needed during the electrodeposition (T = 75 ^{o}C) is shown to be relatively high (paragraph 4.1.1) compared to the electrodeposition of pure nickel from a typical sulfamate electrolyte carried out at about 50 ^{o}C. This affects the stability of the
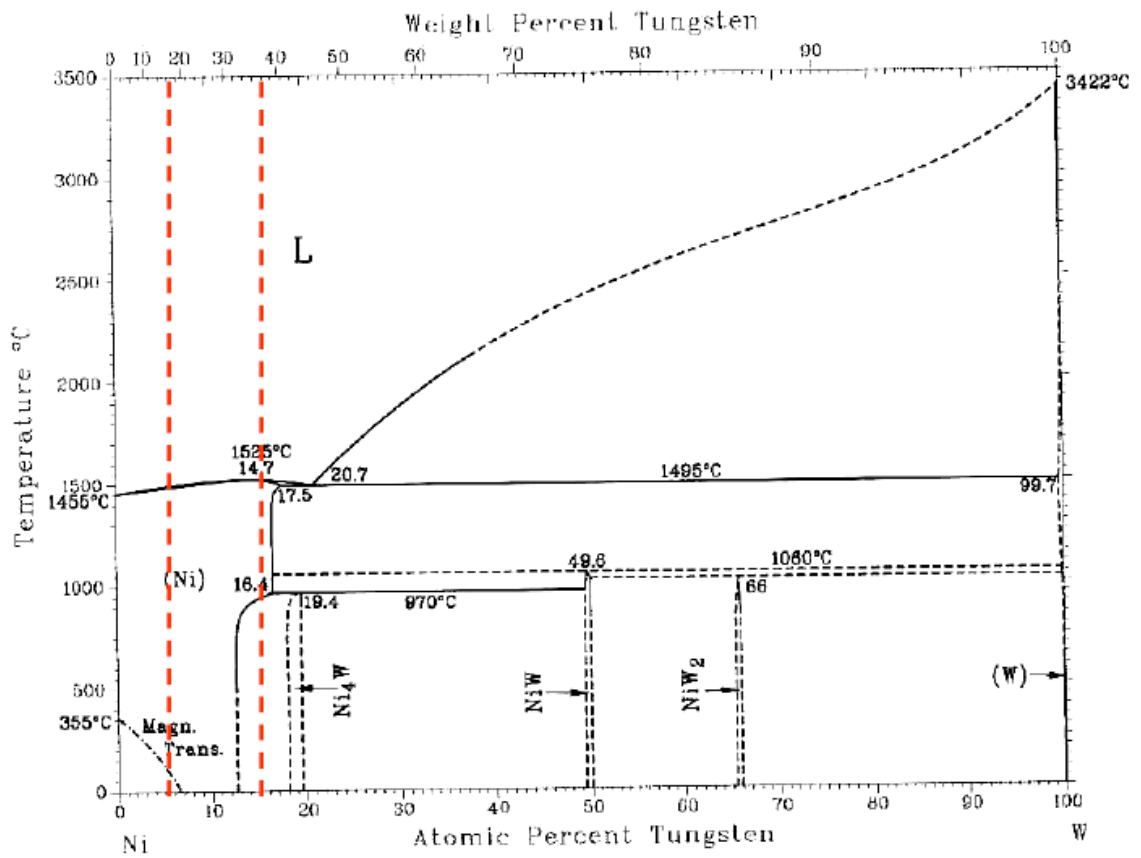
Figure 5.1: Ni-W phase diagram [107]. The material compositions studied in this thesis are indicated by the dashed red lines.

electrolyte and the dimensional accuracy of the resist pattern. The ammonia contained in the solution evaporates easily at high temperature. The loss of ammonia can be relevant if the electrodeposition takes longer time. As a consequence, the pH value shifts to a lower value, which leads to a change of the species distribution in the electrolyte. This change shows an influence on the current efficiency, on the structure of the electroplated material and on the amount of incorporated W. In our case, we covered the electrolyte during the electrodeposition (maximal 40 hours), as described in Section 3.1.1, so that the loss of ammonia stays tolerable. The effect of the high temperature on resist pattern is illustrated through the expansion of the resist structures resulting in inaccuracies in the micropart's dimensions, see Figure 4.7. This effect has to be avoided especially for selected industrial applications where the accuracies in the dimensions are required.

Further, the formation of pits by hydrogen bubble formation at the surface of the microsamples is supposed to be the result of the low current efficiency. As seen in paragraph 4.1.1, the pits are seen on the samples with high W content rather than those containing less W despite the addition of the surfactant. This is also confirmed by the difference in current efficiency between both materials. In fact, the current efficiency in the case of electrodeposition of the alloy with high W content is estimated to be higher than the material with low W content according to [97]. These defects need to be avoided since they affect the mechanical behaviour of the electrodeposited material and thus lower the microspecimens yield. As seen in Paragraph 4.1.1 the surfactant used for this purpose was not sufficient. That is why other solutions have to be followed. For example, increasing the ion concentration in the electrolyte and accordingly the current density not impacting the characteristics of the electrodeposited material (see current efficiency - deposition parameters dependence curves in [97]) presents an eventual measure to enhance the quality of the microsamples.

Last but not least, if we consider the whole wafer, two remarkable features, consisting of the release of the samples and the thickness distribution along the wafer, can be discussed.

The release and the following bending of the microsamples, especially those having a larger surface, is due to the high residual stresses in the material formed during electrodeposition. These stresses include thermal stresses induced by the difference in the thermal coefficient of the layers and growth stresses. This aspect is caused by low current efficiency of the electrolyte. It is an undesirable aspect, since it handicaps the handling of the microsamples shown to be brittle and thus more damageable, and also influences the structure through crack formation and the mechanical properties of the electrodeposited

material. The residual stresses can be reduced by using pulse plating [108] and giving some additives in the electrolyte such as saccharin [109]. The latter solution can, however, lead to the incorporation of components from additives components, for instance, sulfur in saccharin, in the electrodeposited material. this can affect the mechanical behaviour, e.g. ductility of the material.

The thickness distribution of the electrodeposited material along the wafer studied in 4.1.1 is shown to be homogeneous for the wafer with high W content rather than that with low W content. This can be explained by the difference in resistance during the electrodeposition of both alloys. The higher the resistance, the lower a current and consequently the surface roughness is influenced. This resistance includes the resistance part of the charge transfer and the ohmic resistance of the electrolyte. On one hand, the charge transfer is dependent on the reactions occurring at the growing surface, which is shown to be related to the electrolyte composition. On the other hand, the ohmic resistance of the electrolyte is determined by the distance between both electrodes. In the case of corrugated material surface, the piles grow faster than valleys, and thus the material level differences increase when increasing the electrodeposition time. Compared to an older wafer layout shown in [104], the wafer layout developed in the current work assures a more homogeneous thickness distribution as demonstrated in Figure 5.2 (compare 3412 and 482P-01 presenting the thickness distribution on the current wafer and on the old wafer, respectively). The observed homogeneity can be due to the additional electrodeposition of a border around the microspecimens on the new wafer (see Figure 3.4). The thickness inhomogeneities of the old wafer were especially observed on the microspecimens at the border, whereas the new wafer presented inhomogeneities at the added border area.

5.1.2 Mechanical behaviour and reliability

The trend of the microhardness illustrated in Figure 4.9 is also observed in previous work [98] in which the microhardness values of electrodeposited Ni-W with higher W content in dependence of the annealing temperature were presented. However, the curves in the literature reach higher values, probably due to their higher tungsten content. The small increase of the material grain size during annealing at relatively high temperature (till 700 ^{o}C) explains the higher microhardness values of Ni-W alloys compared to pure Nickel. The slight coarsening of the grains between 500 ^{o}C and 700 ^{o}C corresponds to the small decrease of the microhardness values of Ni-W shown in Figure 4.9. This slow coarsening
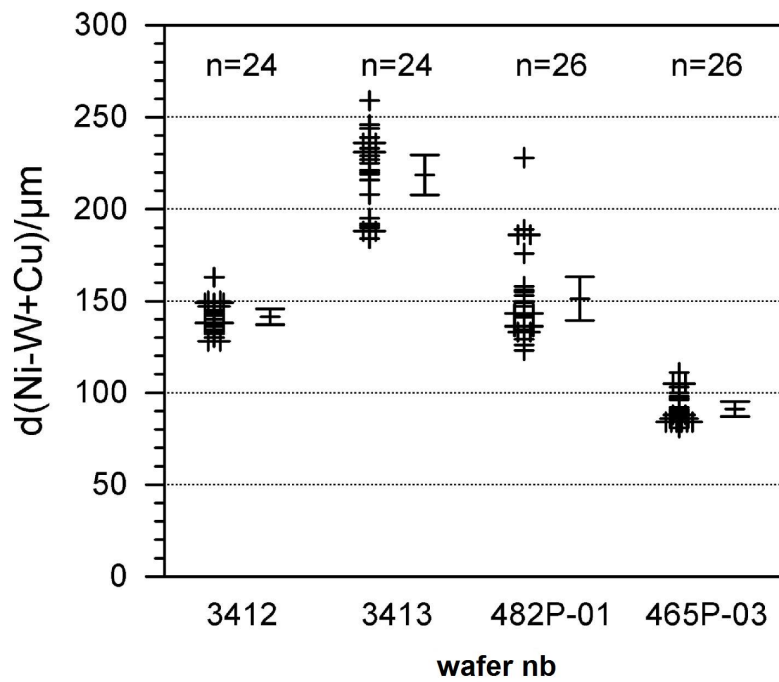
Figure 5.2: Comparison of the thickness distribution of electrodeposited Ni-W with different compositions on wafers with different layouts: 3412 and 3413 current layout (Figure 3.4), 482P-01 and 465P-03 previous layout [104].

effect observed for Ni-W confirms the thermal stability of this material up to 700 ^{o}C which is in good agreement with the tomographic atom probe (TAP) microstructure investigations by [36].

On the one hand, the variation of the W content in the electrodeposited material results in a constant microhardness measured for the alloy with high W content even at high annealing temperatures and durations. The grain size determined by XRD followed a similar trend as the microhardness since the higher hardness values correspond to smaller grain sizes and the small decrease in microhardness is accompanied by a slight increase in the grain size which is in agreement with the Hall-Petch law (see Section 2.4). On the other hand, the observations of the microstructure using TEM delivers clearly larger grain size values. This is due to the ability of XRD-method to determine a measure for coherently diffracting domains that do not correspond to whole grains especially in materials containing more regions with high density of stacking faults. Electrodeposition, for example, is responsible for such defects also seen on the TEM images of Ni-W (see Figures 4.14 and 4.15). Furthermore, the grains are shown to be larger than 150 nm for several samples after annealing, as demonstrated using TEM and XRD, which is outside of the range of measurable grain size using XRD. At this range of grain size ($\geq$ 150 nm), the values determined by XRD present thus higher standard deviation values. One more factor is that the observations using TEM are limited to a small area of few μm, whereas XRD gives results for a larger scanned area of a few mm^2. The material characterized within this work showed a bimodal like grain size distribution at several annealing parameters which is in agreement with findings in the literature stating the non uniformity of the grain size distribution observed on electrodeposited materials (see for example [104] and [110]). Consequently, the mean grain size determined by XRD may have been based only on grains smaller than 150, which could explain the difference between the results of XRD and TEM.

As mentioned above, the strengthening effect seen at the investigated alloys is basically caused by the grain refinement (grains in submicron range) which is still observed even at high annealing temperatures (up to 700 ^{o}C). This is unlike pure nickel showing already coarsened grains at relatively low annealing temperature ($<$ 300 ^{o}C). The grain size was shown to remain nearly constant at relatively low annealing temperatures and increases rapidly at higher ones. This tendency can be described by an Arrhenius-type equation [83]:

$$D^n - D_0^n = K_0 \, t \, e^{\left(\frac{-Q}{RT}\right)} \qquad (5.1)$$

where D_0 is the grain size at $t = 0$, n is the time exponent, K_0 is a constant and Q is the activation energy. n, K_0 and Q are material dependent. R is the universal gas constant.

The parameters n, K_0 and Q are determined for Ni 5 at% W and Ni 15 at% W by fitting Equation 5.1 to the experimental values using a non-linear regression procedure. The resulting values of these parameters are listed in Table 5.1. The quality of the description

Table 5.1: Comparison of the activation energies determined for the Ni-W alloys investigated within this thesis with that of electrodeposited pure nickel [111].

Metal	n	Activation Energy [kJ·mol^{-1}]	K_0 [nm^n/sec]
Ni 15 at% W	8.1	202	$5 \cdot 10^{21}$
Ni 5 at% W	4.86	256	$5.14 \cdot 10^{21}$
electrodeposited nanocystalline nickel	-	102.55	-

by equation 5.1 can be seen in Figure 5.3 and 5.4 where the experimental data are compared to those obtained from the model given above. The activation energies for both Ni-W alloys are higher compared to that of pure nickel. This explained the grain growth of Ni-W happening at high temperature (400 - 700 ^{o}C) unlike pure nickel whose grains begin to coarsen at lower temperatures (70 ^{o}C). The negligible increase of the grain size at low temperatures ($\leq$ 400 ^{o}C) and the higher increase of the grain sizes at higher temperatures ($\geq$ 400 ^{o}C), still remaining in the submicron range confirm the stability of this alloy at high temperatures. However, annealed pure nickel was proven to be instable at this temperature range (up to 700 ^{o}C) since it showed coarse micron sized grains (see Figure 4.10). This finding confirms the results seen in the literature [36] stating the low mobility of the W atoms located at the grain boundaries. The TEM investigations within this work showed fuzzy boundaries which could be an indication for the presence of W at these regions.

The stress-strain curves, described in Section 4.1.3 and showing higher strength, confirm the findings of the microhardness measurements stating the strong behaviour of electrodeposited Ni-W. The brittle behaviour observed at the tensile test of the as-deposited microspecimens with both compositions is in agreement with the high microhardness values and the small size of the grains being in the range of several tens of nanometers. At 400 ^{o}C annealing temperature, the increase of the tensile strength observed for Ni 15 at% W can
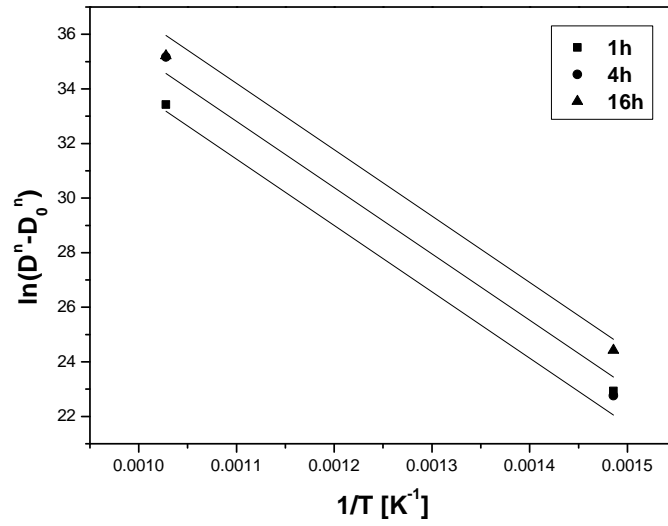
Figure 5.3: The Arrhenius curves for the grain growth of electrodeposited Ni 15 at% W annealed at different durations
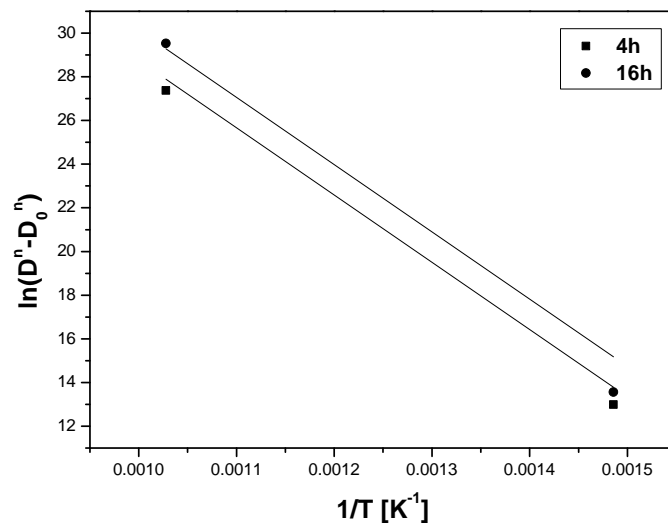
Figure 5.4: The Arrhenius curves for the grain growth of electrodeposited Ni 5 at% W annealed at different durations

be explained by the extreme brittle behaviour of the material in the as-deposited state breaking before reaching its UTS. The increase in plasticity for the Ni 5 at% W annealed at 400 ^{o}C and 700 ^{o}C and the Ni 15 at% W annealed at 700 ^{o}C results from the coarsening of several grains that remain in the submicron range maintaining the high strength of the material. The rest of the grains, which showed slight increase in size during annealing, also presents a main cause of the strength stability noticed even at high annealing temperature. Enhancing the ductility and the simultaneous maintaining of the tensile strength after annealing is due to the microstructure of the material originally shown to be nanocrystalline in the as-deposited state resulting in high strength and a certain brittleness, and, because of few coarsened grains, presents additional plasticity at high annealing temperature. This bimodal distribution of the grain size is especially seen at the Ni 15 at% W samples that demonstrates higher strength than that of Ni 5 at% W.

The comparison of the stress-strain results obtained in the current work with results from other works demonstrates a good agreement in the as-deposited state. The fracture stress of the samples with 15 and 17 at% W shown in [112] are 1208 MPa and 1238 MPa, respectively. They are located near to the values obtained within this work for the high tungsten content. Yamasaki's results, obtained by testing films with 20.7 at% W [113] and by testing Ni 16 at% W tensile specimens with finely dispersed micrometer-sized array through-holes [114] and having a bigger size, show similar stress-strain behaviour to the curves in Figure 4.16. The value of fracture stress determined for the 16 at% W monolithic sample is nearer to the one for the samples with high W content (15 at% W). The higher value (2333 MPa) shown with the 20.7 at% W sample is probably due to the higher W content codeposited in the material than that realized within this thesis (5 and 15 at% W). Additional causes for the disagreement of some mechanical properties, such as fracture strain, could be different electrodeposition parameters such as current density and bath temperature, as well as the number of defects and the amount of residual stress of the electroplated material.

5.2 Ni-Al$_2$O$_3$

5.2.1 Processing parameters

In order to electrodeposit Ni-Al$_2$O$_3$ layers and microspecimens that satisfy the requirements of high temperature MEMS applications including the relatively high thickness ($>$

100 μm) and improved mechanical properties at high temperature, the electrolyte, a dispersion with alumina particles was studied with the purpose to reduce the agglomeration of the nanoparticles in the solution and consequently in the electrodeposited material, and maintain its stability for longer time. Two different alumina-nanoparticles were used within this work: hydrophilic and hydrophobic ones. Depending on the particles' behaviour in the electrolyte, two different dispersion strategies were investigated.

The steric stabilization delivers a homogeneous well-dispersed solution. In the resulting deposits no alumina was detected and the microhardness did not show any change compared to that of pure nickel, which, at first view, confirms that no particles were embedded in the nickel matrix. It is also possible to conclude that the incorporation of the particles could be considered as successful though. In this case, the particles could not be detected with the methods indicated above as they are relatively small in diameter (few nanometers) and may require the use of a different microscopy strategy showing higher resolution (e.g TEM). Since the particles remained well dispersed in the electrolyte after longer aging and thus no precipitate was observed in the electrolyte after longer aging, this dispersion strategy has been shown to be promising for longer deposition processes especially if particles with larger diameter, depending on the necessary size to enhance the mechanical properties at room and at high temperature, are added to the electrolyte.

The electrostatic stabilization has been shown to be improved by the addition of a higher amount of citrate in the solution. In fact, citrate modifies the electrostatic state of Al_2O_3 particles in order to improve their repulsive interaction. At a pH range higher than 6 including the pH needed within this work, citrate species present relatively high degrees of dissociation, leading to the formation of species with high electric charge, and also a higher adsorption degree at the surface of the particles [115]. These citrate properties result in shifting the isoelectric point of the ceramic hydrophilic particles from pH 9.5 to pH 3, far from the pH range of 8.5, used in this thesis. At the isoelectric point, alumina particles show no charge at their surface which leads to stronger agglomeration of the particles. It is also important to note that at a pH higher than 7, nickel hydroxide can be formed. This effect is thought to be avoided by increasing the nickel solubility through the coordination with ammonia and citrate. The material resulting from this dispersion method shows an increased microhardness compared to pure nickel and a certain amount of alumina particles detected by different microscopy methods, which confirms the successful incorporation of the particles in the nickel matrix. That is why the dispersion strategy followed within this

work is to use nickel sulphate electrolytes showing relatively high citrate concentration (0.9 mol/L).

The chemistry of the nickel sulphate electrolyte was studied in order to find out the appropriate parameters to result in compact defect free electrodeposited microspecimens.

As seen in Section 4.2.1, the current efficiency depends on the nickel concentration. This effect is confirmed by the electrodeposition experiment of the microspecimens in Figure 4.27. During the electrodeposition, the nickel concentration was undefined because of the use of the soluble anode. This was demonstrated by the formation of two different regions. On the one hand, region 1, showing more voids, corresponds to the depletion of nickel ions in the solution starting at a Ni^{2+} concentration of 0.06 mol/L which results in low current efficiency of the electrodeposition. On the other hand, region 2 presenting compacter structure stands for the higher nickel concentration which resulted from the continuous release of Ni^{2+} as a product from the oxidation of the nickel atoms in the anode. The higher current efficiency engendered by the enrichment with Ni^{2+} is also confirmed by the thicker electrodeposited material. Nevertheless, the enhancement of the current efficiency by the increase of the Ni^{2+} concentration is accompanied by undesirable features such as small pores and cracks at the surfaces.

The precipitation in the electrolyte was examined through variation of the Ni^{2+} to NH_4^+ concentration ratio. It was found that the precipitation of white or transparent crystals occurs in the case of higher Nickel to ammonia ratio. The formed precipitate is in all probability Nickel hydroxide as shown in the X-ray diffractogram Figure 4.26. This is in agreement with the arguments regarding the formation of nickel hydroxide from the nickel ions, not complexed as ammonia or citrate species, in combination with OH^-. The steps of this precipitation are presented in the following:

$NH_4^+ + H_2O \rightarrow NH_3 + 2(OH^-)$

$Ni^{2+} + OH^- \rightarrow Ni(OH)_2$
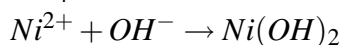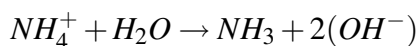
The loss of OH^- should lead to decreasing pH value, which is demonstrated in several precipitation experiments described in Table 4.7. A simplified calculation predicting the precipitate amount is carried out considering the concentrations of the different components in the electrolyte, the pH value and the equilibrium constants. The calculated hydroxide content is plotted against the concentration of ammonium chloride for two different Nickel concentrations in Figure 5.5. The zero line presents the limit separating the domain where the precipitate dissolves $(x(Ni(OH)_2) < 0)$, and where the precipitate is observed in the electrolyte $(x(Ni(OH)_2) > 0)$. The nickel hydroxide amount decreases with the reduction

of the ratio of Nickel to ammonia, which confirms in some degree the trend observed in the experiments described in Table 4.7. The difference in the values of nickel to ammo-
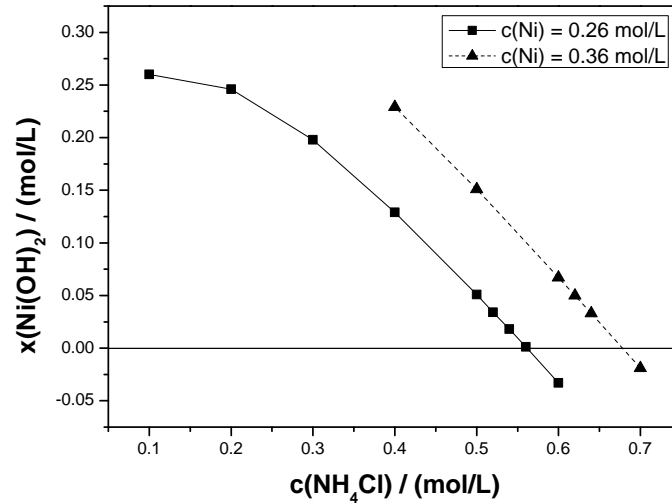
Figure 5.5: Predicted hydroxide amount in dependence on ammonia concentration at two different Ni^{2+} concentrations

nia ratio between the calculated results and the experimental ones is due to possible other reactions and formation of undefined species in the solution. This precipitation has to be avoided within this work since the precipitate, in the form of smaller crystals, can be incorporated in the electrodeposited layer which results in additional effects on the mechanical properties as demonstrated by the increase of the hardness values measured on the material obtained from the electrolyte showing a relatively high nickel ammonia ratio.

The electrolyte suitable for the microspecimens electrodeposition was therefore chosen to be the one with the lowest ratio (0.12) and lowest nickel concentration (0.06 mol/L). Two microspecimens' electrodepositions were realized with different current density. Only, the electrodeposit obtained at the lowest current density presents a compact structure that can be used for further mechanical investigations. This feature is related to the diffusion limiting current density i_{lim} determining the applicable current density range of compact deposition parameters. This limiting value is determined by the following equation [116]:

$$i_{lim} = nFD\frac{c_0}{\delta_N} \tag{5.2}$$

where n, F, D, c_0 and δ_N stand for the number of exchanged electrons in the reduction reaction, the Faraday constant, the diffusion constant, the concentration of the ions in the electrolyte and the thickness of the diffusion layer, respectively. Knowing that in our microspecimen electrodeposition, the diffusion constant of the Ni^{2+}-ions is approximately $10^{-5} = cm^2/s$, $c_0 = 0.06$ mol/L and $\delta_N = 100$ μm, i_{lim} is calculated to be 1.158 A / dm^2. In contrast to the electrodeposition at 1 A / dm^2, the one at 2 A / dm^2 is far above the acceptable range of current density, limited by i_{lim}. This leads to microsamples with a high defect density.

The microspecimens showing compact structure demonstrated relatively homogeneous chemical composition along the cross section which is required for the tensile tests. They also showed lower thickness than expected according to Figure 4.23. This is due to the higher current density used in the experiments resulting in this plot. The dependence of the current efficiency on the current density was also demonstrated in [45]. The higher roughness observed at the surface of the specimens results in non uniformity of the section along the whole sample in general and particularly the gage section. Consequently, this effect requires additional finishing work. The finishing, realized manually for each microspecimen, represents a time consuming task and results in many cases in unusable samples showing disappearing parts, especially on the ear region where the samples are supposed to be mounted in the grids. This undesirable effect could be reduced, for example through electropolishing which consists in finishing the microsamples all at once before releasing them from the wafer.

5.2.2 Mechanical behaviour and microstructural stability at high temperature

The microhardness of the Ni-alumina in the as-deposited as well as the annealed state is shown to be high compared to pure nickel which, after annealing, decreases to a value lower than 30% of the microhardness in the as-deposited state. This decrease in the microhardness of nickel is related to the rapid coarsening of the grains after annealing which is in agreement with the Hall-Petch relation. The enhancement in microhardness at room temperature of Ni-alumina compared to pure nickel is speculated to be principally due to the smaller grain size shown to be in the submicron range (Hall-Petch relation, Section 2.4). The stacking faults, presenting a common effect of the electrodeposition, can also be a cause of the higher microhardness values. In addition, the Orowan relation may have

contributed to the microhardness value, since the embedded nanoparticles were detected inside the grains (see Paragraph 4.2.2). Pure nickel was electrodeposited at the same conditions as Ni-Al$_2$O$_3$ and showed an average grain size of around 40 nm, which is determined by XRD and represents, after conversion to real values given by TEM, a comparable grain size to that of Ni-Alumina estimated by TEM of few hundreds of nanometers. The stress contribution of Orowan can result in a hardness increase of 91 to 363 HV, knowing that:

- G and b for nickel are 76 GPa and 0.249 nm, respectively [117]

- the particle spacing λ is given from the equation $\lambda = (\frac{4\pi}{3\chi_v})^{1/3} r$ where χ_v is the particle volume fraction, found to be 3.84 vol% for alumina particles (see Section 4.2.2) and r ranges between 10 and 40 nm based on the TEM observations in 4.2.2

- determining the hardness number in the scale HV occurs in two steps: the conversion from the MPa unit to the HV unit resulting from the multiplication by 1 / 9.807 and the calculation of the hardness value in MPa correspoding to the stress value τ_y found after the Orowan model knowing that Hardness [MPa] = 3 σ_y [118] and $\sigma_y = 3\ \tau_y$ [117]

The remaining hardness contribution may be an effect of the numerous twins observed inside the grains as demonstrated in [119] that states the increase of the strength of polycrystalline material with decreasing the spaces between the twins.

At higher annealing temperatures, the higher microhardness values of Ni-Al$_2$O$_3$ are associated with the smaller grain size of the nanocomposite which remains in submicron range and is clearly smaller than that of pure nickel, in addition to the particle dispersion and defects strengthening. The slight change in grain size of Ni-Al$_2$O$_3$ during annealing is due to the grain boundary pinning effect caused by the alumina particles.

The tensile test of Ni-Al$_2$O$_3$ at room temperature confirms the higher strength and the brittle behaviour demonstrated by the microhardness investigations.

5.2.3 Comparison to published results

The common electrolyte in the literature, used to fabricate Ni-Al$_2$O$_3$, consists in the sulfamate or sulfate solution showing a pH in the acid range between 3 and 4, unlike the one used within this work with an alkaline sulphate with ammonia citrate solution. It's worth noting that the electrolyte with the alkaline solution is shown to be better dispersed than

the acid one as shown in [51] and [120]. In fact in [51], where sulfamate solution was used, the ratio agglomerate size embedded in the layers as well as microposts to nominal size of particles as delivered is much larger than that observed in the current work. In order to obtain homogeneous particle sulfamate dispersion, some additives (e.g. cumarin and saccharin) are added in the electrolyte as mentioned in [51], [121] and [45]. This method resulted in smaller agglomerate size. However, different elements, which are included in the additives, can be incorporated in the electrodeposit which leads to undesirable effects on the mechanical properties, for example, embrittlement caused by carbon contained in saccharin.

The volume fraction of Al_2O_3 incorporated in the electrodeposits within this work is determined to range between 3 and 8%. The latter value deviates from those found in the literature due to some differing electrolyte parameters such as the different Al_2O_3 concentration in the electrolyte as shown in [120], [45] and [121]. The agglomerates size and the particles nominal size also present a cause of the deviation in the amount of embedded particles [51].

The microhardness varied in the range of approximately 500 to 700 HV which also confirmed values from the literature cited above. The tensile strength determined in the first tensile test is shown to be higher than that obtained in [117]. This is due to the higher volume fraction of particles incorporated in our electrodeposits which results in more dispersion strengthening. The ductility shown by the material in [117], contrary to ours which presented a brittle behaviour, may be due to its electrolyte chemistry resulting in a different microstructure (grain size, grains shape).

5.3 Ni-Al

5.3.1 Electrolyte optimization

Since aluminum ions can not be reduced from an aqueous solution as nickel can, the incorporation of aluminum in the nickel matrix occurs by codepositing aluminum particles dispersed in a nickel electrolyte. An ammonia citrate electrolyte was used unlike the conventional ones used in the literature; see, for example, the diluted Watts bath in [121] and nickel sulfamate electrolyte in [122]. The choice of the above cited bath chemistry is based on the purpose of dispersing the aluminum particles, enveloped by a thin aluminum oxide layer, with a similar strategy as for the electrodeposition of nickel containing hydrophilic

alumina particles. The current electrolyte composition showed a nickel to ammonia concentration ratio of 0.5 which exceeds the allowable value before the precipitation of the white crystals described in Section 4.2.1. The expected precipitate was not observed in the electrolyte since we prepared the solution and quickly added the particles which hindered the ability to see whether the white precipitate was formed. This effect has to be considered in future work while adjusting the mentioned ratio with respect to other electrodeposition parameters (pH, current efficiency) and their influence on the material structure.

The pH of the Ni-Al electrolyte was chosen to be in the neutral range in order to avoid dissolving the aluminum particles that are known to be unstable in acids as well as basic solutions.

The temperature during the electrodeposition was chosen in the room temperature range in a first trial and then increased to 50 ^{o}C which represents the known temperature used to electrodeposit nickel. The starting experiment with low temperature is due to safety reasons. In fact, aluminum particles especially the nanosized ones are reactive in humid milieus which require the full attention while manipulating such particles. The heat could in some degree enhance this effect. This explains then the proceeding of the gradual increasing of the temperature. The higher temperature was proven to be harmless, that is why it can be used in future Ni-Al depositions since this temperature is shown to be beneficial for pure nickel electrodeposition.

The instability of the dispersion noticed independently from the particles size may be due to some electroless processes happening progressively. Among others we can mention the oxidation of Al to Al^{3+}, the reduction of Ni^{2+} to nickel which can be formed at the surface of the aluminum particles, and hydrogen gas formation as a result of water decomposition. In order to verify these speculations additional work, consisting in determining the chemical composition of the electrolyte after longer ageing time and investigating the thermodynamic parameters of these electroless processes, is needed.

The layers resulting from the electrolyte discussed above showed a very rough surface in the case of incorporating the microparticles while a relatively smoother surface was observed after codepositing the nanoparticles. The embedded particles are electrically conductive and consequently become part of the cathode surface from which nickel nucleates and grows outward as clearly seen in Section 4.3.2 and demonstrated in the literature [123]. According to this growth mechanism, larger particles can engender mounds at the surface [122] responsible for the enormous roughness observed while incorporating the

microparticles. The nickel layers containing aluminum nanoparticles have been shown to be suitable for the use in MEMS applications.

The amount of nanoparticles embedded in the nickel layer was about 4 at%, if we consider the measurements using the chemical analysis which is more reliable than EDX. The purpose of this work is the development of nickel superalloys through the formation of the γ' - phase leading to the microstructural stability at high temperatures (up to 700 ^{o}C). According to the phase diagram of Ni-Al (Figure 5.6), the formation of the high temperature resistant γ'- phase is reached only at an Al content $\geq$ 7 at%. More precisely, the γ'- phase
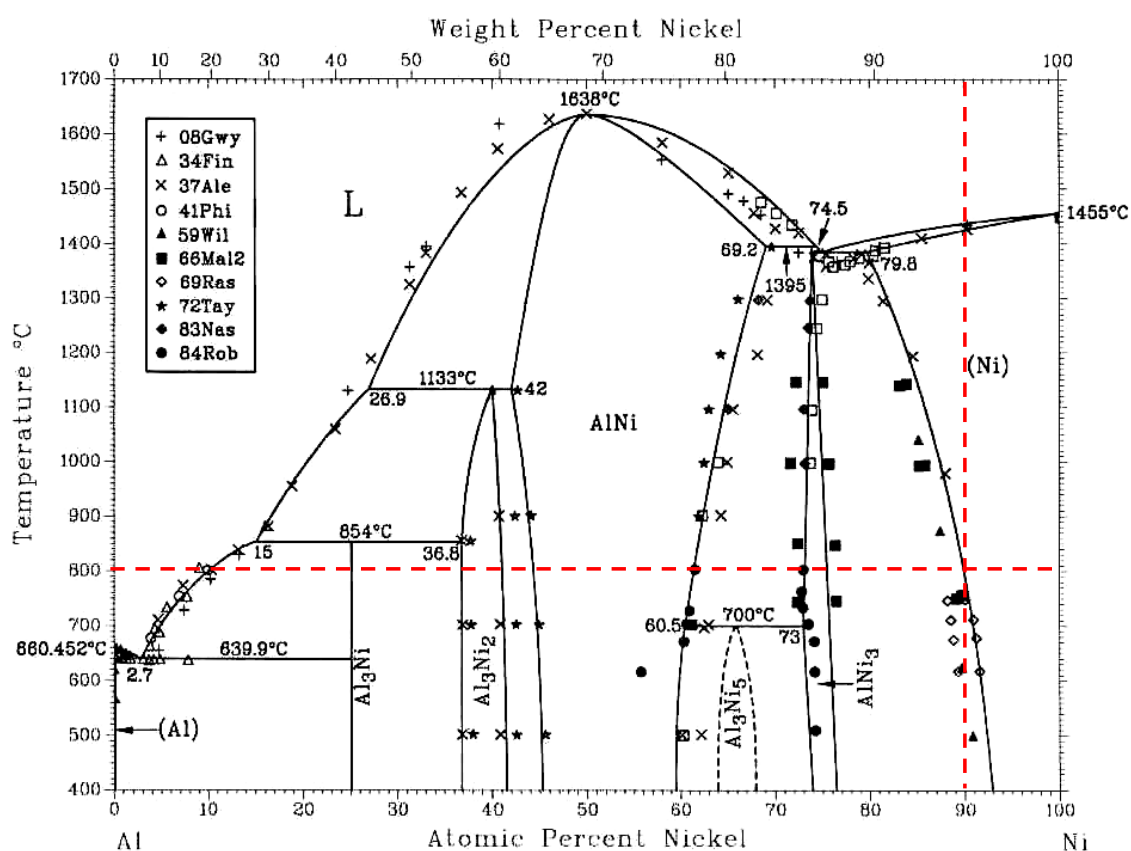
Figure 5.6: Ni-Al phase diagram [107]. The dashed lines present the upper limit of the concerned temperature range and the appropriate minimum in aluminum content.

is stable at higher temperatures (up to 800 ^{o}C) in the case of higher aluminum percentage not less than about 10 at% as indicated in Figure 5.6 which is not in agreement with the particles' amount obtained through the electrodeposition described within the current work. Some previous works confirm the formation of γ' - phase after a defined annealing

of Ni-Al layers with 6.6 wt% corresponding to about 12 at% aluminum [121], however they did not mention whether this new phase persists at longer exposure to temperatures higher than 700 ^{o}C. The formation of this phase is possible in regions close to an aluminum particle where the needed Al-concentration is exceeded locally. In order to ensure the stability of this high temperature resistant phase for longer use at high temperature, it is worth electrodepositing a material showing the amount required in the Ni-Al phase diagram.

To enhance the amount of the incorporated aluminum particles, some arrangements can be made. For example, a cathode which is positioned horizontally below the anode can be used so that particles sediment on it while reducing nickel from the solution as described in [124]. Another possible solution consists in increasing the concentration of aluminum in the dispersion which leads to higher particle incorporation in the electrodeposited nickel layer similar to [122]. Codeposition of Cr in Ni-Al composite also presents a promising strategy to decrease the amount of incorporated aluminum needed to result in the γ' phase. If we consider the ternary phase diagram Ni-Al-Cr, we remark that an alloy with 10 at% aluminum, 72.5 at% nickel and 17.5 at% chromium, for instance, is located approximately in the middle square of the γ - γ' regime (see Figure 5.7).

5.3.2 First ideas about the annealing parameters for the formation of the γ' - phase

The formation of Ni$_3$Al phase, also called γ'- phase, requires a definite annealing process including annealing temperature and duration and governing the diffusion kinetics that result in the high temperature resistant phase. Before starting the annealing experiment some speculations about these parameters will be presented.

The idea behind the estimation of the annealing parameters is based on the determination of the diffusion length x which is proportional to $\sqrt{Dt}$. D and t stand for the diffusion constant and diffusion time, respectively.

The diffusion length indicated in Figure 5.8 is considered as the width of the nickel shell surrounding the spherical shaped aluminum particles. This spherical shell contains the amount of nickel needed to transform an aluminum particle into a γ' - particle. According to the stoichiometric ratios, the necessary number of nickel atoms $n(Ni)$ represents 3 times
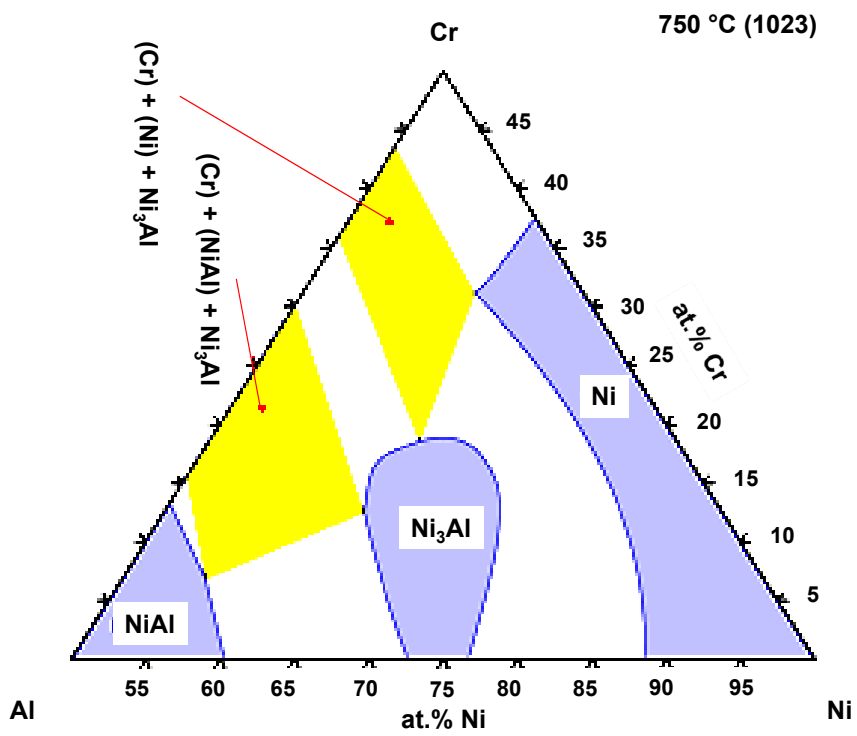
Figure 5.7: Ni-Al-Cr ternary phase diagram
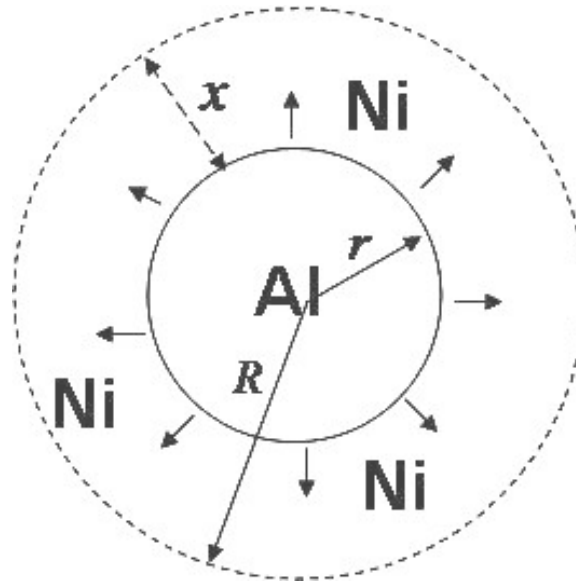
Figure 5.8: Schematic representation of the diffusion strategy thought to transform a Al-particle into a γ' - particle.

that of the aluminum atoms contained in a particle. The latter atoms number $n(Al)$ is given by the following equation:

$$n(Al) = \frac{4\pi}{3} (\frac{r}{d(Al)})^3 \cdot RE_{Al} \qquad (5.3)$$

where $d(Al)$ is the diameter of an aluminum atom and RE_{Al} is the volume ratio of aluminum.

Knowing that $x = R - r$, x can be calculated based on equation 5.3 as shown in the following:

$$x = \sqrt[3]{\frac{3}{4\pi \cdot RE_{Ni}} \cdot d(Ni)^3 \cdot n(Ni) + r^3} - r \qquad (5.4)$$

in which RE_{Ni} represents the volume ratio of nickel.

The diffusion constant is dependent on the annealing temperature and is known in most cases for each element diffusing in a definite phase. Therefore at a fixed temperature, the annealing duration can be determined from the relation $\sqrt{Dt}$.

The diameter of the obtained γ'- particle ($2R$) can be determined based on the calculated x value. Consequently the increase in strength caused by this second phase can be predicted before starting with any experiment. The purpose of this prediction is to optimize the

mechanical properties required by the high temperature MEMS applications and thus the corresponding electrodeposition parameters (particles size, particles concentration in the electrolyte).

6 Summary

Electrodeposited pure nickel shows poor mechanical properties and also a poor microstructural stability at elevated temperatures. To ensure the thermal stability the current work deals with the development of new electrodeposited materials including Ni-W alloys, Ni-Al_2O_3 nanocomposites and Ni based superalloys.

Ni-W alloy was electrodeposited from an ammonia citrate electrolyte developed in [97]. Two different alloy compositions (Ni 5 at% W and Ni 15 at% W) located in the allowable region of the Ni-W phase diagram where no intermetallics precipitate within the concerned temperature range (till 800 ^oC), were deposited in the form of layers and microspecimens. Some processing features observed on the microspecimens were discussed in terms of capability to be used for MEMS applications. Compact microspecimens showing a thickness higher than 100 μm and homogenous composition distribution could be fabricated in a batch process from a wafer delivering a high number of microparts. It is worth noting the relatively homogenous distribution of the thickness and the tolerable surface roughness at the surface that could be treated depending on the requirements of the MEMS application. Hence the yield of microparts is relatively high, close to 100 %, which is a relevant aspect for reducing the costs and time of this microfabrication process.

Ni-W was investigated in terms of mechanical properties and microstructure in the as-deposited and annealed state. The mechanical properties of interest comprise microhardness and tensile testing. The microstructure of the material was observed and quantified using FIB, SEM, TEM and XRD. These investigations demonstrated higher strength and a brittle behaviour in the as-deposited state, compared to pure nickel, through the higher hardness value, higher tensile strength and the brittle fracture observed for both compositions. The microstructure was determined to be nanocrystalline showing a grain size smaller than 100 nm which explains the higher strength of the Ni-W alloys. After exposure at high temperature (300 ... 700 ^oC) the strength and microhardness remained high and more plasticity was seen. The grain size of Ni-W alloys increased slightly in contrast to the enormous coarsening of the nickel microstructure after annealing. This may be due

to the W segregation at the grain boundaries and low diffusivity of the W atoms impeding the boundaries movement during the high temperature annealing. The effect of the variation in W content led to higher strength for the alloy with higher W content on the one side and higher plasticity shown by the material with low W content on the other side. This could be explained by the higher fraction of small grains shown by Ni 15 at% W resulting in grain boundaries strengthening and the higher large grain density observed on the Ni 5 at% W leading to the higher plasticity.

For the electrodeposition of Ni-Al$_2$O$_3$ an alkaline nickel sulfate electrolyte containing ammonia and citrate, unlike the common used acid sulfamate solution, was developed in order to disperse hydrophilic alumina nanoparticles with a diameter of 17 nm. The effects of several electrolyte parameters on the dispersion stability and structure of the electrodeposited material were studied. Sedimentation experiments showed that a higher citrate content led to smaller agglomerate size and longer stability of the electrolyte. This is due to the electrostatic stabilization of citrate in an alkaline environment. Furthermore, the nickel concentration demonstrated an influence on the current efficiency which increases with an increasing nickel concentration in the solution. The higher the current efficiency, the faster the electrodeposition process and the less hydrogen is developing resulting in a homogeneous and smooth surface. Due to the precipitation of white crystals at high nickel to ammonia ratios (> 0.12) a correlation of the nickel to the ammonia was proven. Because of the undefined electrolyte composition at these ratios which might result in undefined deposits, electrodeposition took place at lower ratios. The current density is also a relevant parameter deciding on the structure of the electrodeposit. When the current density exceeded the diffusion limiting current density, a compact material could not be realized because of a high density of defects like pores and cracks.

After optimizing the electrodeposition parameters, microspecimens and layers were electroplated for further characterizations. The electrodeposited material, investigated by SEM and EDX, showed a compact structure and an Al$_2$O$_3$ content of about 3 wt% detected on the layers and about 1.3 wt% on the microspecimens confirming the successful incorporation of particles in the nickel matrix. The microspecimens showed a relatively homogeneous composition distribution across the sample and a surface roughness of a few microns that could be removed by an additional finishing step.

Based on the data obtained by the microhardness and tensile testing, Ni-Al$_2$O$_3$, in the as-deposited state, showed a higher strength and brittle behaviour compared to pure nickel. This strengthening behaviour can be due to the grain size schown to be in the submicron

range (Hall-Petch). After exposure at higher temperatures (till 600 ^{o}C), the microhardness remains unchanged at intermediate temperatures, followed by a slight decrease at higher temperature, unlike pure nickel where strength drops strongly to about 30 % of the initial value even at annealing temperatures lower than 300 ^{o}C. The observed strength stability was in good agreement with the microstructural investigations that showed a slight coarsening of the grains during annealing. At higher exposure temperature (600 ^{o}C), the grain size was still in the submicron range according to the qualitative FIB images. The microstructural stability of Ni-Al$_2$O$_3$ at higher annealing temperature is due to the pinning of the grain boundaries by the nanoparticles. This grain refinement at high temperature presents an additional strenghtening factor (Hall-Petch).

Ni-Al composites were electrodeposited from an ammonia citrate nickel-sulfate electrolyte with a neutral pH value and containing nano- and microsized metallic aluminum particles. An annealing process could be proposed to produce the γ'-phase which is characteristic of a Ni superalloy. It has been shown that the size of the particles embedded in the nickel layer affect the structure of the electrodeposited layer. In fact, deposition with microparticles resulted in a non-compact layer showing an enormous surface roughness, while the addition of nanosized particles results in a compact layer with relatively smooth surfaces. Through monitoring the electrolyte during several days after the electrodeposition and measuring the surface roughness of electrodeposited layers, it was observed that the electrolyte is instable. This was probably due to electroless processes in the dispersion. Additional work on the electrolyte chemistry is required in order to enhance the stability of the solution at least during the electrodeposition process.

Concerning the formation of the γ'-phase, a scheme was developed to predict the annealing parameters. Assuming that each aluminum particle is transformed into a γ'- particle, the annealing time necessary at a definite temperature is calculated from the diffusion distance ($x = \sqrt{Dt}$) of aluminum in nickel.

As demonstrated above, the materials developed within this work present promising materials for high temperature MEMS applications since they showed a relatively stable microstructure and high strength at high exposure temperatures. More information about the creep behaviour, which is a relevant effect observed while operating at high temperature environments, have to be obtained through further mechanical testing at elevated temperatures. For this purpose a high temperature tensile set-up using digital image correlation for the strain measurement is developed and some tests have already been carried out.

Bibliography

[1] P. Bley, W. Bacher, W. Menz, and J. Mohr, "Description of microstructures in LIGA-technology," *Microelectron. Eng.*, vol. 13, no. 1 - 4, pp. 509 – 512, 1991.

[2] K. Zum Gahr, *Material- und Verfahrensentwicklung für mikrotechnische Hochleistungsbauteile*. Wissenschaftliche Berichte FZKA 6662, Oktober 2001.

[3] N. Miyano, K. Tagaya, K. Kawase, K. Ameyama, and S. Sugiyama, "Fabrication of alloy and ceramic microstructures by LIGA-MA-SPS process," *Sensors and Actuators A: Physical*, vol. 108, pp. 250 – 257, 2003.

[4] E. W. Becker, W. Ehrfeld, P. Hagmann, A. Maner, and D. Münchmeyer, "Fabrication of microstructures with high aspect ratios and great structural heights by synchrotron radiation lithography, galvanoforming, and plastic moulding (LIGA process)," *Microelectron. Eng.*, vol. 4, no. 1, pp. 35 – 56, 1986.

[5] P. Bley, "Polymers: an excellent and increasingly used material for microsystems," *Micromachined Devices and Components V*, vol. 3876, no. 1, pp. 172 – 184, 1999.

[6] S. Griffiths, J. Crowell, B. Kistler, and A. S. Dryden, "Dimensional errors in LIGA-produced metal structures due to thermal expansion and swelling of PMMA," *Journal of Micromechanics and Microengineering*, vol. 14, no. 11, pp. 1548 – 1557, 2004.

[7] C. Khan Malek and V. Saile, "Applications of LIGA technology to precision manufacturing of high-aspect-ratio micro-components and -systems: a review," *Microelectronics Journal*, vol. 35, no. 2, pp. 131 – 143, 2004.

[8] C. Thueringen, U. Beckord, and R. Bessey, "Construction and manufacturing of a microgearhead with 1.9-mm outer diameter for universal application," in *Society*

of Photo-Optical Instrumentation Engineers (SPIE) Conference Series, vol. 3680, pp. 526 – 533, 1999.

[9] L. Stephens and K. Kelly, "Bearings and mechanical seals enhanced with microstructures," August 2001. United States Patent 6,280,090.

[10] A. Cox and E. Garcia, "Development of a LIGA-based elastodynamic flying mechanism," in *Smart Structures and Materials 1998: Smart Structures and Integrated Systems*, vol. 3329, pp. 2–8, 1998.

[11] Y. Cheng, B. Shew, C. Lin, T. Hung, G. Hwang, C. Kuo, S. Tseng, D. Lee, and G. Chang, "Liga spinnerets for microfibers," in *Transducer 99*, pp. 1452 – 1455, 1999.

[12] J. Fahrenberg, S. T., B. W., A. El-Kholi, and W. Schomburg, "High aspect ratio multi-level mold inserts fabricated by mechanical micro machining and deep etch X-ray lithography," *Microsystem Technologies*, vol. 2, no. 4, pp. 174 – 177, 1996.

[13] S. Ford, A. McCandless, X. Liu, and S. Soper, "Rapid fabrication of embossing tools for the production of polymeric microfluidic devices for bioanalytical applications," in *Society of Photo-Optical Instrumentation Engineers (SPIE) Conference Series*, vol. 4560, pp. 207 – 216, 2001.

[14] J. Hruby, "LIGA technologies and applications," in *MRS Bulletin*, pp. 337 – 340, 2001.

[15] K. Kelly, C. Harris, L. Stephens, C. Marques, and D. Foley, "Industrial applications for LIGA-fabricated micro heat exchangers," in *Society of Photo-Optical Instrumentation Engineers (SPIE) Conference Series*, vol. 4559, pp. 73 – 84, 2001.

[16] R. Cahn, P. Haasen, and E. Kramer, eds., *Materials Science and Technology: Processing of Metals and Alloys (chapter 11)*, vol. 15. Weinheim: Wiley-WCH, 1996. ISBN 3-527-26828-6.

[17] W. H. Safranek, *The properties of Electrodeposited Metals and Alloys*. American Electroplaters and Surface Finishers Society, second ed., 1986. ISBN 978-0936569000.

[18] R. Weil, "The structures of electrodeposits and the properties that depend on them," *Annual Review of Materials Science*, vol. 19, no. 1, pp. 165 – 182, 1989.

[19] M. Whitehurst, "Strength and ductility of electrodeposited nickel," in *Symposium on electrodeposited metals as materials for selected applications*, pp. 53 – 64, 1971.

[20] U. Erb, A. El-Sherik, G. Palumbo, and K. Aust, "Synthesis, structure and properties of electroplated nanocrystalline materials," *Nanostructured Materials*, vol. 2, no. 4, pp. 383 – 390, 1993.

[21] F. Ebrahimi, G. Bourne, M. Kelly, and M. T.E., "Mechanical properties of nanocrystalline nickel produced by electrodeposition - morphology and properties of deposits," *Nanostructured Materials*, vol. 11, no. 3, pp. 343 – 350, 1999.

[22] H. Cho, K. Hemker, K. Lian, J. Goettert, and G. Dirras, "Measured mechanical properties of LIGA Ni structures," *Sensors and Actuators A: Physical*, vol. 103, no. 1 - 2, pp. 59 – 63, 2003.

[23] Z. Xie, D. Pan, H. Last, and K. Hemker, "Effect of as-processed and annealed microstructures on the mechanical properties of LIGA Ni MEMS," in *Material Research Society Symposia proceedings*, vol. 605, pp. 197 – 202, 2000.

[24] J. Wittenauer, ed., *The Invar Effect, A Centennial Symposium*. Warrendale: The Minerals, Metals and Materials Society, 1996. ISBN 0873393740.

[25] G. Beranger, F. Duffaut, J. Morlet, and J. Tiers, eds., *The Iron-Nickel Alloys*. New York: Lavoisier Publishing, 1996. ISBN 1898298491 / 9781898298496.

[26] J. McCrea, G. Palumbo, G. Hibbard, and U. Erb, "Properties and applications for electrodeposited nanocrystalline Fe-Ni alloys," *Reviews on Advanced Materials Science*, vol. 5, no. 3, pp. 252 – 258, 2003.

[27] M. Ghorbani, A. I. zad, A. Dolati, and R. Ghasempour, "The effect of the Cr and Mo on the physical properties of electrodeposited Ni-Fe alloy films," *Journal of Alloys and Compounds*, vol. 386, no. 1 - 2, pp. 43 – 46, 2005.

[28] S. Graham, J. Kelley, N. Yang, and T. Borca-Tasciuc, "The role of microstructure in the electrical and thermal conductivity of Ni-alloys for LIGA microsystems," *Microsystem Technologies*, vol. 10, no. 6, pp. 510 – 516, 2004.

[29] G. Carlson, A. Paranjpye, J. Summers, and D. Thompson, "Current-driven device using NiMn alloy and method of manufacture," 2008. USPTO Patent Application 20080124565.

[30] D. Clark, D. Wood, and U. Erb, "Industrial applications of electrodeposited nanocrystals," *Nanostructured Materials*, vol. 9, no. 1 - 8, pp. 755 – 758, 1997.

[31] R. Taheri, I. Oguocha, and S. Yannacopoulos, "The tribological characteristics of electroless NiP coatings," *Wear*, vol. 249, no. 5 - 6, pp. 389 – 396, 2001.

[32] E. Slavcheva, W. Mokwa, and U. Schnakenberg, "Electrodeposition and properties of. niw films for mems application," *Electrochim. Acta*, vol. 50, no. 28, pp. 5573 – 5580, 2005.

[33] G. Spanier, E. Slavcheva, and W. Mokwa, "Hf-contact elements for testing and multi chip module applications," *Microsystem Technologies*, vol. 12, no. 10 - 11, pp. 1015 – 1019, 2006.

[34] C. Schuh, T. Nieh, and H. Iwasaki, "The effect of solid solution W additions on the mechanical properties of nanocrystalline Ni," *Acta Materialia*, vol. 51, no. 2, pp. 431 – 443, 2003.

[35] A. Haseeb, U. Albers, and K. Bade, "Friction and wear characteristics of electrodeposited nanocrystalline nickelñtungsten alloy films," *Wear*, vol. 264, no. 1 - 2, pp. 106 – 112, 2008.

[36] P. Choi, T. Al-Kassab, F. Gartner, H. Kreye, and R. Kirchheim, "Thermal stability of nanocrystalline nickel-18 at.% tungsten alloy investigated with the tomographic atom probe," *Materials Science and Engineering: A*, vol. 353, no. 1 - 2, pp. 74 – 79, 2003.

[37] V. Greco, "Electrocomposites and their benefits," *Plating and Surface Finishing*, vol. 76, no. 7, pp. 62 – 67, 1989.

[38] P. Ebdon, "The performance of electroless nickel PTFE composites," *Plating and Surface Finishing*, vol. 75, no. 9, pp. 65 – 68, 1988.

[39] R. Mevrel, "State of the art on high-temperature corrosion-resistant coatings," *Materials Science and Engineering A-Structural Materials Properties, Microstructure and Processing*, vol. 120, no. 3, pp. 13 – 24, 1989.

[40] Y. Sofer, Y. Yarnitzky, and S. F. Dirnfeld, "Evaluation and uses of composite Ni-Co matrix coatings with diamonds on steel applied by electrodeposition," *Surface and coatings technology*, vol. 42, no. 3, pp. 227 – 236, 1990.

[41] G. Malone, "Electrodeposition of dispersion-strengthened alloys," *Plating and Surface finishing*, vol. 78, no. 8, pp. 58 – 62, 1991.

[42] R. Williams and P. Martin in *Proc. Interfinish 64*, pp. 182 – 188, 1964.

[43] D. Snaith and P. Groves, "Study of the mechanism of cermet electrodeposition," in *Trans. Instit. Met. Finish*, vol. 50, pp. 95 – 101, 1972.

[44] N. Guglielmi, "Kinetics of the deposition of inert particles from electrolytic baths," *J. Electrochem. Soc.*, vol. 119, no. 8, pp. 1009 – 1012, 1972.

[45] I. Shao, P. Vereecken, C. Chien, P. Searson, and R. Cammarata, "Synthesis and characterization of particle-reinforced Ni/Al2O3 nanocomposites," *Journal of Materials Research*, vol. 17, no. 6, pp. 1412 – 1418, 2002.

[46] A. Kariapper and J. Foster, "Further studies on the mechanism of formation of electrodeposited composite coatings," *Transactions of the Institute of Metal Finishing*, vol. 52, no. 3, pp. 87 – 91, 1974.

[47] F. K. Sautter, "Electrodeposition of dispersion-hardened Nickel-Al_2O_3 alloys," *Journal of The Electrochemical Society*, vol. 110, no. 6, pp. 557 – 560, 1963.

[48] T. Tomaszewski, L. Tomaszewski, and H. Brown, "Codeposition of finely dispersed particles with metals," *Plating*, vol. 56, pp. 1234 – 1239, 1969.

[49] M. Verelst, J. Bonino, and A. Rousset, "Electroforming of metal matrix composite - dispersoid grain-size dependence of thermostructural and mechanical properties," *Materials Science and Engineering A-Structural Materials Properties, Microstructure and Processing*, vol. 135, pp. 51 – 57, 1991.

[50] G. Michelsen-Mohammadein and G. Steinborn, "Verbesserte tribologische eigen-schaften durch nanodispersionsschichten," *Galvanotechnik*, vol. 91, no. 11, pp. 2940 – 2950, 2000.

[51] T. Wang and K. Kelly, "Particulate strengthened Ni-Al$_2$O$_3$ microcomposite HARMs for harsh-environmental micromechanical applications," *Journal of Micromechanics and Microengineering*, vol. 15, no. 1, pp. 81 – 90, 2005.

[52] G. Vidrich, J. Castagnet, and H. Ferkel, "Dispersion behavior of Al$_2$O$_3$ and SiO$_2$ nanoparticles in nickel sulfamate plating baths of different compositions," *Journal of The Electrochemical Society*, vol. 152, no. 5, pp. C294 – C297, 2005.

[53] J. Karthaus, K. Bade, and W. Bacher, *Galvanische Abscheidung von Metallen aus nichtwässrigen Elektrolyten für die Mikrosystemtechnik*. Wissenschaftliche Berichte FZKA 6455, March 2000.

[54] Y. Zhou, X. Peng, and F. Wang, "Oxidation of a novel electrodeposited Ni-Al nanocomposite film at 1050 ^{o}C," *Scripta Materialia*, vol. 50, no. 12, pp. 1429 – 1433, 2004.

[55] Y. Zhou, X. Peng, and F. Wang, "Cyclic oxidation of alumina-forming Ni-Al nanocomposites with and without CeO2 addition," *Scripta Materialia*, vol. 55, no. 11, pp. 1039 – 1042, 2006.

[56] X. Meng, H. Chen, and H. Vehoff, "Fractography, elastic modulus and oxidation resistance of novel metal-intermetallic ni/ni$_3$al multilayer films," *J. Mater. Res.*, vol. 17, no. 4, pp. 790 – 796, 2002.

[57] Y. Li, J. Zhao, G. Zeng, C. Guan, and X. He, "Ni/Ni3Al microlaminate composite produced by EB-PVD and the mechanical properties," *Materials Letters*, vol. 58, no. 10, pp. 1629 – 1633, 2004.

[58] J. Newman, *Electrochemical Systems*, p. 431. Englewood Cliffs, New Jersey: Prentice Hall, 1973. ISBN 0132489228.

[59] C. Wagner, "Theoretical analysis of the current density distribution in electrolytic cells," *Journal of The Electrochemical Society*, vol. 98, no. 3, pp. 116 – 128, 1951.

[60] C. Kasper, "The theory of the potential and the technical practice of electrodeposition," in *Transactions of the Electrochemical Society*, vol. 77, p. 365, 1940.

[61] C. Kasper, "The theory of the potential and the technical practice of electrodeposition IV," in *Transactions of the Electrochemical Society*, vol. 78, p. 147, 1940.

[62] C. Kasper, "The theory of the potential and the technical practice of electrodeposition V," in *Transactions of the Electrochemical Society*, vol. 82, 1942.

[63] A. West, M. Matlosz, and D. Landolt, "Normalized and average current distributions on unevenly spaced patterns," *Journal of The Electrochemical Society*, vol. 138, no. 3, pp. 728 – 735, 1991.

[64] S. Mehdizadeh, J. O. Dukovic, P. C. Andricacos, L. T. Romankiw, and H. Y. Cheh, "The influence of lithographic patterning on current distribution: A model for microfabrication by electrodeposition," *Journal of The Electrochemical Society*, vol. 139, no. 1, pp. 78–91, 1992.

[65] K. Bade, A. Fath, and W. Leskopf, "Galvanische prozesse in der mikrosystemtechnik," *Galvanotechnik*, vol. 53, no. 9, pp. 34 – 38, 1999.

[66] N. Masuko, T. Osaka, and Y. Ito, eds., *Electrochemical Technology: Innovation and New Developments*. Amsterdam, The Netherlands: Gordon and Breach Publishers, 1996.

[67] A. Ilzhöfer, H. Schneider, and C. Tsakmakis, "Tensile testing device for microstructured specimens," *Microsystem Technologies*, vol. 4, pp. 46 – 50, 1997.

[68] S. M. Allameh, "An introduction to mechanical-properties-related issues in MEMS structures," *Journal of Materials Science*, vol. 38, pp. 4115 – 4123, 2003.

[69] H. Kahn, A. Heuer, and R. Ballarini, "On-chip testing of mechanical properties of MEMS devices," in *MRS Bulletin*, vol. 26, pp. 300 – 301, 2001.

[70] M. Haque and M. Saif, "Application of MEMS force sensors for in situ mechanical characterization of nano-scale thin films in SEM and TEM," *Sensors and Actuators A: Physical*, vol. 97 - 98, pp. 239 – 245, 2002.

[71] W. Sharpe Jr, J. Bagdahn, K. Jackson, and G. Coles, "Tensile testing of MEMS materials-recent progress," *Journal of Materials Science*, vol. 38, pp. 4075 – 4079, 2003.

[72] M. Zupan, M. Hayden, C. Boehlert, and K. Hemker, "Development of high-temperature microsample testing," *Experimental Mechanics*, vol. 41, no. 3, pp. 242 – 247, 2001.

[73] E. Hall, "The deformation and ageing of mild steel: III discussion of results," *Proceedings of the Physical Society. Section B*, vol. 64, no. 9, pp. 747 – 753, 1951.

[74] N. J. Petch, "The cleavage strength of polycrystalline," *Journal of the Iron and Steel Institute*, vol. 173, pp. 25 – 28, 1953.

[75] M. A. Meyersm and E. Ashworth, "A model for the effect of grain size on the yield stress of metals," *Philosophical Magazine A*, vol. 46, no. 5, pp. 737 – 759, 1982.

[76] K. Kumar, H. Van Swygenhoven, and S. Suresh, "Mechanical behaviour of nanocrystalline metals and alloys," *Acta Materialia*, vol. 51, pp. 5743 – 5774, 2003.

[77] H. Cho, K. Hemker, K. Lian, and J. Goettert, "Tensile, fatigue and creep properties of LIGA nickel structures," in *MEMS 2002 Technical Digest*, 15th IEE Int. Conf. On MEMS, pp. 439 – 442, 2003.

[78] U. Klement, U. Erb, A. M. El-Sherik, and K. T. Aust, "Thermal stability of nanocrystalline Ni," *Materials Science and Engineering A*, vol. 203, no. 1 - 2, pp. 177 – 186, 1995.

[79] T. Hentschel, I. D., R. Kirchheim, F. Müller, and H. Kreye, "Nanocrystalline Ni-3.6 at.% P and its transformation sequence studied by atom-probe field-ion microscopy," *Acta Materialia*, vol. 48, pp. 933 – 941, 2000.

[80] O. Preston and N. Grant, "Dispersion strengthening of copper by internal oxidation," *Trans. Met. Soc. AIME*, vol. 221, pp. 164 – 173, 1961.

[81] F. Humphreys, "The nucleation of recrystallization at second phase particles in deformed aluminum," *Acta. Metall.*, vol. 25, pp. 1323 – 1344, 1977.

[82] R. Doherty and J. Martin, "The effect of a dispersed second phase on the recrystal-lization of aluminium-copper alloys," *J. Inst. Metals*, vol. 91, pp. 332 – 338, 1962-3.

[83] F. Humphreys and M. Matherly, *Recrystallization and Related Annealing Phenom-ena*. Oxford, UK: Elsevier, 2004. ISBN 0-08-044164-5.

[84] S. Wang and W. Wei, "Characterization of electroplated Ni/SiC and Ni/Al$_2$O$_3$ com-posite coatings bearing nanoparticles," *J. of Material Research Society*, vol. 18, no. 7, pp. 1566 – 1574, 2003.

[85] J. Naser, H. Ferkel, and W. Riehemann, "Grain stabilisation of copper with nanoscaled Al2O3-powder," *Materials Science and Engineering A*, vol. 234 - 236, pp. 470 – 473, 1997.

[86] F. Humphreys and V. Ramaswami in *Proc. 3rd Int. Conf. on high Voltage Electron Microscopy, Oxford*, pp. 268 – 272, 1973.

[87] P. F. Schmidt and 13 Co-Authors, *Praxis der Rasterelektronenmikroskopie und Mikrobereichsanalyse*. Renningen-Malmsheim: Expert, 1994. ISBN 3-8169-1038-6.

[88] W. Bragg, "The diffraction of short electromagnetic waves by a crystal," in *Pro-ceedings of the Cambridge Philosophical Society*, vol. 17, pp. 43 – 57, 1913.

[89] G. Williamson and W. Hall, "X-ray line broadening from filed aluminium and wol-fram," *Acta Metallurgica*, vol. 1, no. 1, pp. 22 – 31, 1953.

[90] H. Klug and L. Alexander, *X-Ray Diffraction Procedures*, pp. 655 – 665. New York: Wiley-Interscience, 1974.

[91] J. Marien, J. Plitzko, R. Spolenak, R.-M. Keller, and J. Mayer, "Quantitative electron spectroscopic imaging studies of microelectronic metallization layers," *Journal of Microscopy*, vol. 194, no. 1, pp. 71 – 78, 1999.

[92] D. Kiener, C. Motz, M. Rester, M. Jenko, and G. Dehm, "FIB damage of Cu and possible consequences for miniaturized mechanical tests," *Materials Science and Engineering: A*, vol. 459, no. 1 - 2, pp. 262 – 272, 2007.

[93] G. Dieter, *Mechanical Metallurgy*. SI Metric Edition, UK: McGraw-Hill BookCompany, 1988. ISBN 0-07-084187-X.

[94] M. Zupan, D. Lavan, and K. Hemker, "Tensile testing of single crystal gamma Ti - 55.5 Al," in *Material Research Society Proceedings, High Temperature Ordered Intermetalllic Alloys*, vol. 460, pp. 171 – 176, 1996.

[95] C. Matthek, *Warum alles kaputt geht? - Form und Versagen in Natur und Technik*. Germany: Forschungszentrum Karlsruhe, 2003. ISBN 978-3-923704-41-5.

[96] *http://www.mathworks.com/matlabcentral/fileexchange/12413*.

[97] A. Haseeb and K. Bade, "LIGA fabrication of nanocrystalline Ni-W alloy micro specimens from ammonia-citrate bath," *Microsystem Technologies*, vol. 14, no. 3, pp. 379 – 388, 2008.

[98] T. Yamasaki, P. Schloβmacher, K. Ehrlich, and Y. Ogino, "Formation of amorphous electrodeposited Ni-W alloys and their nanocrystallization," *Nanostructured Materials*, vol. 10, no. 3, pp. 375 – 388, 1998.

[99] M. Obradovic, R. Stevanovic, and A. Despic, "Electrochemical deposition of Ni-W alloys from ammonia-citrate electrolyte," *Journal of Electroanalytical Chemistry*, vol. 552, pp. 185 – 196, 2003.

[100] J. Van Der Lee and L. De Windt, *Chess Tutorial and Cookbook*. Technical Report Nr. LHM/RD/99/05, Ecole des Mines de Paris, Fontainebleau, France, 1999.

[101] D. K. Bade, *Institute for Microstruture Technology*. Private communication.

[102] R. Hammond, "Galvanisches vernickeln in sulfamatbädern," *Metalloberfläche, Angewandte Electrochemie*, vol. 26, no. Heft 8, pp. 291 – 298, 1972.

[103] W. Bacher, K. Bade, B. Matthis, M. Saumer, and R. Schwarz, "Fabrication of LIGA mold inserts," *Microsystem Technologies*, vol. 4, no. 3, pp. 117 – 119, 1998.

[104] J. Aktaa, J. Reszat, M. Walter, K. Bade, and K. Hemker, "High cycle fatigue and fracture behavior of LIGA nickel," *Scripta Materialia*, vol. 52, no. 12, pp. 1217 – 1221, 2005.

[105] D. S. Suresha, *Johns Hopkins University*. Private communication.

[106] D. Burns and D. S. Suresha, *Johns Hopkins University*. Private communication.

[107] P. Nash, ed., *Phase Diagrams of Binary Nickel Alloys*. ASM International, 1991. ISBN 0-87170-365-3.

[108] I. Mizushima, P. Tang, H. Hansen, and M. Somers, "Residual stress in Ni-W electrodeposits," *Electrochimica Acta*, vol. 51, no. 27, pp. 6128 – 6134, 2006.

[109] K. Bade, M. Haj-Taieb, and A. Haseeb, "Legierungsabscheidung für LIGA-Mikroteile und Werkzeugen am Beispiel von Ni-Fe und Ni-W," in *Technologien und Werkstoffe der Mikro- und Nanosystemtechnik*, vol. 53 of *GMM-Fachbericht*, pp. 67 – 72, VDE-Verl., 2007.

[110] A. Talin, E. Marquis, S. Goods, J. Kelly, and M. Miller, "Thermal stability of ni-mn electrodeposits," *Acta materialia*, vol. 54, no. 7, pp. 1935 – 1947, 2006.

[111] M. Iordache, S. Whang, Z. Jiao, and Z. Wang, "Grain growth kinetics in nanostructured nickel," *NanoStructured Materials*, vol. 11, no. 8, pp. 1343 – 1349, 1999.

[112] A. Giga, Y. Kimoto, Y. Takigawa, and K. Higashi, "Demonstration of an inverse Hall-Petch relationship in electrodeposited nanocrystalline Ni-W alloys through tensile testing," *Scripta Materialia*, vol. 55, no. 2, pp. 143 – 146, 2006.

[113] T. Yamasaki, "High-strength nanocrystalline Ni-W alloys produced by electrodeposition and their embrittlement behaviors during grain growth," *Scripta Materialia*, vol. 44, no. 8 - 9, pp. 1497 – 1502, 2001.

[114] T. yamasaki, N. Oda, H. Matsuoka, and T. Fukami, "Tensile strength of electrodeposited nanocrystalline ni-w alloys with finely dispersed micrometer-sized array through-holes," *Materials Science and Engineering A*, vol. 449 - 451, pp. 833 – 835, 2007.

[115] M. Song, J. Lee, Y. Lee, and J. Koo, "Stabilization of gamma alumina slurry for chemical-mechanical polishing of copper," *Journal of Colloid and Interface Science*, vol. 300, no. 2, pp. 603 – 611, 2006.

[116] C. Haman and W. Vielstich, *Elektochemie*, p. 178. 3. vollständig überarbeitete Auflage, Wiley-VCH, 1998. ISBN 3-527-27894-x.

[117] S. Goods, R. Janek, T. Buchheit, J. Michael, and P. Kotula, "Oxide dispersion strengthening of nickel electrodeposits for microsystem applications," *Metallurgical and Materials Transactions A*, vol. 35, no. 8, pp. 2351 – 2360, 2004.

[118] D. Tabor, *The hardness of Metals*. USA: Oxford University, 2000. ISBN 0198507763.

[119] L. Lu, X. Chen, X. Huang, and K. Lu, "Revealing the maximum strength in nanotwinned copper," *Science*, vol. 323, pp. 607 – 610, 2009.

[120] D. Thiemig, A. Bund, and J. Talbot, "Untersuchungen zur elektrochemischen herstellung und zu den struktur-eigenschaftsbeziehungen von nickeldispersionsschichten," *Galvanotechnik*, vol. 99, no. 10, pp. 2397 – 2410, 2008.

[121] T. Wang, M. Sorrell, K. Kelly, and E. Ma, "Ni-Al$_2$O$_3$ and Ni-Al composite high-aspect-ratio microstructures," *Materials and Device Characterization in Micromachining*, vol. 3512, no. 1, pp. 344 – 352, 1998.

[122] D. Susan, K. Barmak, and A. Marder, "Electrodeposited NiAl particle composite coatings," *Thin Solid Films*, vol. 307, no. 1 - 2, pp. 133 – 140, 1997.

[123] I. Naploszek-Bilnik, A. Budniok, B. Losiewicz, L. Pajak, and E. Lagiewka, "Electrodeposition of composite Ni-based coatings with the addition of Ti or/and Al particles," *Thin Solid Films*, vol. 474, no. 1 - 2, pp. 146 – 153, 2005.

[124] H. Liu and W. Chen, "Electrodeposited Ni-Al composite coatings with high Al content by sediment co-deposition," *Surface and Coatings Technology*, vol. 191, no. 2 - 3, pp. 341 – 350, 2005.